

Fusion studies in $^{12}\text{C} + ^{182,184,186}\text{W}$ reactions at energies below and near the Coulomb barrier

Thesis submitted to the University of Calicut

in partial fulfillment of the requirements

for the award of the degree of

Doctor of Philosophy in Physics

by

Sanila. S

Under the guidance of

Dr. A. M. Vinodkumar



Department of Physics

University of Calicut

Kerala 673635

India

June 2023



UNIVERSITY OF CALICUT

DR. A. M. Vinodkumar .
Professor
Department of Physics

Calicut University P. O.
Kerala INDIA 673 635
Tel: 0494-2407415
Fax: 0494-2400269
Mob: 9645078924
Email: amv@uoc.ac.in

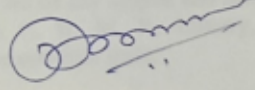
DP/AMV/2023/06-02

02 June 2023

CERTIFICATION OF SUPERVISOR

This is to certify that all the corrections/suggestions from the adjudicators have been incorporated in the thesis and that the content in the thesis and the soft copy are one and the same.

University of Calicut


Dr. A. M. Vinodkumar

Date: 02-06-2023



UNIVERSITY OF CALICUT

DR. A. M. Vinodkumar
Professor
Department of Physics

Calicut University P. O.
Kerala INDIA 673 635
Tel: 0494-2407415
Fax: 0494-2400269
Mob: 9645078924
Email: amv@uoc.ac.in

DP/AMV/2023/06-02

02 June 2023

CERTIFICATE

Certified that the work presented in this thesis entitled '**Fusion studies in $^{12}\text{C} + ^{182,184,186}\text{W}$ reactions at energies below and near the Coulomb barrier**' is a bonafide work done by Ms. Sanila. S under my guidance for the award of the degree of Doctor of Philosophy in Physics, at the Department of Physics, University of Calicut, and that this work has not been included in any other thesis submitted previously for the award of any degree and has undergone plagiarism check using OURIGINAL software at C. H. M. K. Library, University of Calicut, and the similarity index found within the permissible limit.

University of Calicut

Date: 02-06-2023

Dr. A. M. Vinodkumar

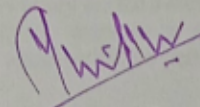
(Supervisor)

UNIVERSITY OF CALICUT
CERTIFICATE ON PLAGIARISM CHECK

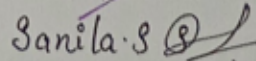
1.	Name of the research scholar	Sanila.S		
2.	Title of thesis/dissertation	Fusion studies in $^{12}\text{C} + ^{102,104,106}\text{W}$ reactions at energies below and near the Coulomb barrier		
3.	Name of the supervisor	Dr. A. M. Vinodkumar		
4.	Department/Institution	Department of Physics University of Calicut		
5.	Similar content (%) identified	Introduction/ Review of literature	Materials and Methods	Result/ Discussion/Summary / Conclusion
		0%	5%	0%
	Acceptable maximum limit (%)	25	25	10
6.	Software used	Ouriginal		
7.	Date of verification	28/10/2022		

*Report on plagiarism check, specifying included/excluded items with % of similarity to be attached

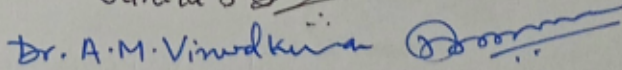
Checked by (with name, designation & Signature)


 Dr. VINOD. V.M
 Assistant Librarian(Sr.Scale)
 University of Calicut

Name and signature of the Researcher

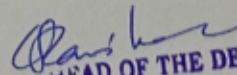

 Sanila.S

Name & Signature of the Supervisor


 Dr. A.M. Vinodkumar

The Doctoral Committee* has verified the report on plagiarism check with the contents of the thesis, as summarized above and appropriate measures have been taken to ensure originality of the Research accomplished herein.

Name & Signature of the HoD/HoI (Chairperson of the Doctoral Committee)


HEAD OF THE DEPARTMENT
DEPARTMENT OF PHYSICS
UNIVERSITY OF CALICUT

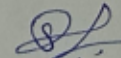
* In case of languages like Malayalam, Tamil, etc. on which no software is available for plagiarism check, a manual check shall be made by the Doctoral Committee, for which an additional certificate has to be attached

DECLARATION

I hereby declare that the work presented in this thesis entitled '**Fusion studies in $^{12}\text{C} + ^{182,184,186}\text{W}$ reactions at energies below and near the Coulomb barrier**' is based on the original work done by me under the guidance of Dr. A. M. Vinodkumar, Professor, Department of Physics, University of Calicut, and has not been included in any other thesis submitted previously for the award of any degree. It is also declared that the thesis undergone plagiarism check using OURIGINAL software at C. H. M. K. Library, University of Calicut, and the similarity index found within the permissible limit.

University of Calicut

Date: 02-06-2023



Sanila. S

Publications

International Journals

1. **S. Sanila**, A. M. Vinodkumar, B. R. S. Babu, N. Madhavan, S. Nath, J. Gehlot, Rohan Biswas, Chandra Kumar, Gonika, Anjali Rani, A. Parihari, Dinesh Viswakarma, Shoaib Noor, E. Prasad, Fusion studies in $^{12}\text{C} + ^{182,184,186}\text{W}$ reactions at energies below and near the Coulomb barrier
Phys. Rev. C **106**, 024614 (2022).
2. **S. Sanila**, A. M. Vinodkumar, B. R. S. Babu, Systematics for multinucleon transfer in heavy ion reactions
Pramana **94**, 70 (2020).
3. P. Jisha, A. M. Vinodkumar, **S. Sanila**, K. Arjun, B. R. S. Babu, J. Gehlot, S. Nath, N. Madhavan, Rohan Biswas, A. Parihari, A. Vinayak, Amritraj Mahato, E. Prasad, and A. C. Visakh, Role of positive transfer Q values in fusion cross sections for $^{18}\text{O} + ^{182,184,186}\text{W}$ reactions
Phys. Rev. C **105**, 054614 (2022).
4. A. C. Visakh, E. Prasad, P. V. Laveen, M. Shareef, A. Shamlath, S. Nath, N. Madhavan, J. Gehlot, Gonika, Rohan Biswas, A. Parihari, J. Khuyagbaatar, B. Lommel, B. Kindler, A. M. Vinodkumar, B. R. S. Babu, **S. Sanila**, K. M. Varier, and S. Appannababu, Fusion studies in $^{16}\text{O} + ^{142,150}\text{Nd}$ reactions at energies near the Coulomb barrier
Phys. Rev. C **104**, 054602 (2021).

Conference Proceedings

1. **S. Sanila**, A. M. Vinodkumar, B. R. S. Babu, Systematics for one and two neutron transfer in heavy ion reactions, DAE Symp. Nucl. Phys. **62**, 564 (2017).
2. **S. Sanila** A. M. Vinodkumar, B.R.S. Babu, S.R. Abhilash, S. Ojha, G.R. Umapathy, D. Kabiraj, Fabrication of thin targets of $^{180}\text{WO}_3$, DAE Symp. Nucl. Phys. **62**, 1094 (2017).
3. P. Jisha, A.M. Vinodkumar, **S. Sanila**, K. Arjun, B.R.S. Babu, J.Gehlot, S. Nath, N. Madhavan, Biswas Rohan, A. Parihari, A. Vinayak, Mahato Amritraj, A.C. Visakh, E. Prasad, Comparisons of evaporation residue cross-section of ^{16}O and ^{18}O induced reactions on W isotopes DAE Symp. Nucl. Phys. **65**, 271 (2021).
4. P. V. Laveen, E. Prasad, N. Madhavan, J. Gehlot, S. Nath, A.C. Visakh, M. Shareef, A. Shamlath, M.M. Hosamani, DVGRKS. Kumar, Md Moin. Shaikh, V. Srivastav, **S. Sanila**, R. Tripath, T.N. Nag, Evaporation residue cross section measurement for the $^{28}\text{Si} + ^{188,192}\text{Os}$ reactions DAE Symp. Nucl. Phys. **62**, 650 (2017).

Acknowledgements

First and foremost, I would like to express my sincere and deep sense of gratitude to my thesis supervisor Dr. A. M. Vinodkumar, professor, Department of Physics, University of Calicut, for his invaluable guidance and constant support during my PhD studies. He is always available to his students and responds more promptly than one can imagine. He taught me how to address or approach various scientific problems. His effective guidance and encouragement were essential to completing this work. It was a great pleasure and experience to work under his guidance.

I am deeply indebted to our collaborator and my M.Sc. teacher, Dr. E. Prasad, Assistant Professor, Department of Physics, School of Physical Sciences, Central University of Kerala, who inspired me to pursue a research career in experimental nuclear physics.

I would like to express my sincere gratitude to Dr. B. R. S. Babu, former professor, Department of Physics, University of Calicut, for his valuable advice and critical remarks about my work.

It is my great pleasure to express my deep sense of gratitude and sincere thanks to Dr. N. Madhavan, Dr. S. Nath, and Dr. J. Gehlot, Scientists, IUAC, New Delhi, for their continuous support and help all the time and during the experiments. I would like to thank the Pelletron group, IUAC, New Delhi for providing good quality beams during the experiments.

I would like to thank my friends and collaborators, Rohan Biswas, Chandra Kumar, Gonika, Anjali Rani, A. Parihari, Dinesh Viswakarma, and Shoaib Noor, for their help and support all the time and throughout the experiments.

I would like to express my sincere thanks to Dr. C. D. Ravikumar, Professor and Head, Department of Physics, University of Calicut, for providing me with all the facilities available in the department during my Ph. D.

I am extremely grateful to all the former H.O.Ds, Department of Physics, University of Calicut, for providing support and for extending facilities to carry out my research work.

I am grateful to other faculty members and office staffs of the Department of Physics, University of Calicut.

I wish to express my heartfelt thanks to my colleagues Jisha, Irshad, Arjun, and Jinu for their care and support. I received a lot of direct and indirect help from former and current research students. I am taking this opportunity to thank all of them.

I would like thank to University of Calicut and IUAC, New Delhi, for financial support in the form of fellowship.

I wish to express my sincere and endless gratitude to my family who have supported me all through this journey. I express my sincere thanks to my husband, Dr. Marimuthu N, and his family for their support.

Finally, I would like to thank all my colleagues and my friends from different universities and institutes all over the country who helped and inspired me during this journey.

Sanila. S

Contents

List of Figures	iv
Preface	vii
1 Introduction	1
1.1 Classification of heavy ion reactions	1
1.2 Heavy ion fusion reactions	6
1.3 Non-compound nuclear fission processes	10
1.4 Motivation of the present work	12
1.5 Present study	17
1.6 Plan of the thesis	18
Bibliography	19
2 Theoretical models	26
2.1 One-dimensional barrier penetration model	26
2.2 Coupled-channel formalism	29
2.3 Coupled-Channel code CCFULL	31
2.3.1 Coupling matrix elements	34
2.4 Statistical model	36
2.5 Statistical model code: HIVAP	38
Bibliography	42

3	Experimental Details	45
3.1	Introduction	45
3.2	15 UD tandem accelerator	45
3.3	Heavy Ion Reaction Analyzer (HIRA)	48
3.4	Detection system	52
3.4.1	Silicon Surface Barrier Detector (SSBD)	52
3.5	Multi-Wire Proportional Counters	53
3.6	Electronic setup	55
3.7	Experimental Details	56
	Bibliography	59
4	Data Analysis and Results	60
4.1	Introduction	60
4.2	Data analysis	60
4.3	Coupled-channel calculations	67
4.3.1	$^{12}\text{C}+^{182}\text{W}$ reaction	68
4.3.2	$^{12}\text{C}+^{184}\text{W}$ reaction	69
4.3.3	$^{12}\text{C}+^{186}\text{W}$ reaction	70
4.4	Statistical model calculations	72
4.5	Comparison with the nearby systems	76
4.6	Discussion	78
	Bibliography	82
5	Study of Quasifission processes in $^{180-198}\text{Hg}$ compound nuclei	85
5.1	Introduction	85
5.2	Systematic analysis for $^{180-198}\text{Hg}$ CN	88
5.3	Dependence of QF on entrance channel parameters	92
	Bibliography	94

6 Summary and Outlook	99
6.1 Future plan	102
Bibliography	103

List of Figures

1.1	Different processes involved in heavy ion collisions as a function of impact parameter.	2
1.2	Schematic illustration of the ℓ dependence of the partial cross section for compound nucleus (CN)	4
1.3	Schematic representation of the compound nucleus formation and decay.	8
1.4	Schematic illustration of fusion-fission, quasifission and deep inelastic scattering in a heavy ion reactions.	11
1.5	Calculated mass distributions of fission fragments for induced fission of $^{180,184,188,192,196}\text{Hg}$	14
3.1	Schematic representation of 15 UD Pelletron accelerator at IUAC, New Delhi.	47
3.2	A schematic diagram of Heavy Ion Reaction Analyzer (HIRA) . .	50
3.3	A complete view of Heavy Ion Reaction Analyzer (HIRA) setup .	50
3.4	Schematics of the multi-wire proportional counter.	53
3.5	Photograph of the multi-wire proportional counter.	54
3.6	The schematic diagram of the electronics and data acquisition system used in the ER measurements.	56
3.7	Inside view of target chamber with target ladder.	57

4.1	Two dimensional plot between ΔE and TOF of events recorded at the focal plane of HIRA for $^{12}\text{C}+^{182}\text{W}$ reaction at 70.0 MeV.	62
4.2	Two dimensional plot between X-position and TOF of events recorded at the focal plane of HIRA for $^{12}\text{C}+^{182}\text{W}$ reaction at 70.0 MeV.	62
4.3	Two dimensional plot between X-position and ΔE of events recorded at the focal plane of HIRA for $^{12}\text{C}+^{182}\text{W}$ reaction at 70.0 MeV.	63
4.4	Measured ER cross sections for the $^{12}\text{C}+^{182,184,186}\text{W}$ reactions.	65
4.5	Measured fusion cross sections along with CC calculation for the $^{12}\text{C}+^{182}\text{W}$ reaction.	68
4.6	Measured fusion cross sections along with CC calculation for the $^{12}\text{C}+^{184}\text{W}$ reaction.	70
4.7	Measured fusion cross sections along with CC calculation for the $^{12}\text{C}+^{186}\text{W}$ reaction.	71
4.8	Experimental ER and fission excitation functions for $^{12}\text{C}+^{182}\text{W}$ reaction along with HIVAP calculations.	74
4.9	Experimental ER and fission excitation functions for $^{12}\text{C}+^{184}\text{W}$ reaction along with HIVAP calculations.	75
4.10	Experimental ER and fission excitation functions for $^{12}\text{C}+^{186}\text{W}$ reaction along with HIVAP calculations.	75
4.11	Reduced cross sections as a function of $E_{c.m.}$ for reactions forming Hg nuclei.	77
4.12	Reduced cross sections as a function of $E_{c.m.}$ for reactions forming CN close to Hg nuclei.	77

4.13	Comparison of present measurements and calculations with the measurements and calculation by Rajagopalan <i>et al.</i> and Delagrangre <i>et al.</i> for $^{12}\text{C}+^{182}\text{W}$ reaction.	80
4.14	Comparison of present measurements and calculations with the measurements and calculation by Delagrangre <i>et al.</i> for $^{12}\text{C}+^{186}\text{W}$ reaction.	80
5.1	Measured ER cross sections along with statistical model calculations as a function of E^* for the reactions forming ^{180}Hg to ^{188}Hg CN.	90
5.2	Measured ER cross sections along with statistical model calculations as a function of E^* for the reactions forming ^{190}Hg to ^{198}Hg CN.	91
5.3	The variation of P_{CN} with the entrance-channel mass asymmetry (α).	92
5.4	The variation of P_{CN} with the effective fissility parameter (χ_{eff}).	93

Abstract

Inclusion of various channels into coupled-channel calculations is highly successful in interpreting experimental sub barrier fusion cross sections. The statistical-model is used to explain the basic features of composite system de-excitation in the above Coulomb barrier energies. However, in ^{12}C -induced reactions with $^{182,186}\text{W}$ targets, measured fusion cross sections are significantly lower than those predicted by various theoretical models and by fusion systematics (Rajagopalan *et al.*, Phys. Rev. C 25, 2417 (1982) and Delagrange *et al.*, Nucl. Phys. A 429, 173 (1984)). To study the fusion cross sections for reactions forming ^{194}Hg , ^{196}Hg and ^{198}Hg compound nuclei, we have measured the evaporation residue (ER) cross sections for $^{12}\text{C}+^{182,184,186}\text{W}$ systems at energies below and near the Coulomb barrier. The experiment was carried out at Inter University Accelerator Centre (IUAC), New Delhi using ^{12}C beams. The measured fusion cross sections are compared with coupled-channel and statistical model calculations. Coupled-channel calculations with the coupling of static deformation effects of target nuclei, and using the selected potential parameters for $^{12}\text{C}+^{182}\text{W}$ reaction very well explains the measured fusion cross-sections for $^{12}\text{C}+^{182,184,186}\text{W}$ reactions in the sub-barrier energy region. However, deviations from the measured cross sections have been noticed at higher excitation energies for $^{12}\text{C}+^{184,186}\text{W}$ reactions. The statistical model calculations with compound nucleus formation probability, $P_{CN} = 1$ and fission barrier scaling parameter, $k_f = 0.96$ describes our measured evaporation residue as well as measured fission cross sections from literature.

From these results, we can conclude that the previously reported disagreement between measured and calculated fusion cross sections for $^{12}\text{C}+^{182,186}\text{W}$ reactions could be due to the missing of evaporation residue events in their detection system.

In addition, a systematic analysis was performed for the reactions forming $^{180-198}\text{Hg}$ compound nuclei, which shows the dependence of quasifission processes on entrance channel mass asymmetry and effective fissility parameter. Additional experiments with reactions leading to the formation of the Hg compound nuclei with entrance channel mass asymmetry 0.1-0.3 and effective fissility parameter 0.63-0.70 are needed to confirm these findings.

Chapter 1

Introduction

The availability of various heavy ion beams from different accelerator facilities all over the world and the development of new spectrometers have given a new impetus to the field of nuclear reaction dynamics. Measured fusion excitation functions for light and medium-heavy nuclei were successfully explained by the predictions of the well-known Wong's formula [1]. In the heavier mass region, the reaction mechanism is no more a simple process. The energetic heavy ions carry a large amount of angular momentum in the entrance channel, as a consequence, the fission saddle point lies outside the barrier and leads to non-compound nuclear processes like quasifission, fast fission, etc. The reaction dynamics are closely linked to the nuclear structure of the participating species and are still a fascinating research topic.

1.1 Classification of heavy ion reactions

Reactions induced by projectiles heavier than an alpha particle are considered to be heavy ion-induced reactions. For understanding the reaction dynamics, structural properties of nuclei etc, scattering, fusion reactions, transfer reactions, and Coulomb excitation were employed. The mechanisms of the heavy ion induced reactions can be classified based on the classical impact parameter, angular momentum, and entrance channel parameters. An example of the

classification of the reactions as a function of impact parameters is shown in Fig. 1.1. The associated de-Broglie wavelength in heavy ion collisions is much smaller compared to the dimensions involved, so the concept of classical trajectory is valid in heavy ion collisions.

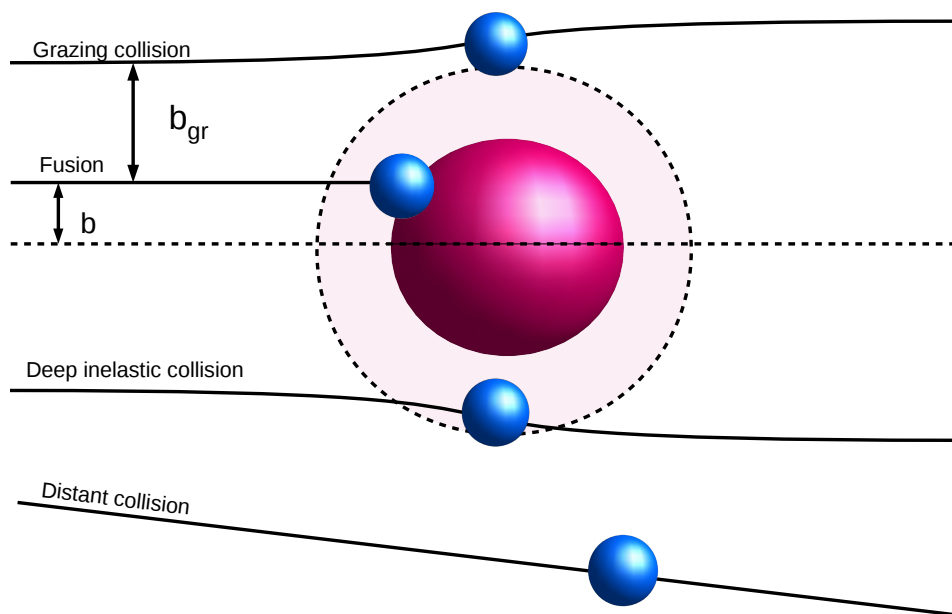


Figure 1.1: Different processes involved in heavy ion collisions as a function of impact parameter.

In the semi-classical approach, the impact parameter, b is defined as the perpendicular distance between the projectile velocity direction and the center of the target nucleus. The minimum value of the impact parameter at which nuclear forces are negligible in comparison with the Coulomb interaction is called the “grazing impact parameter”, b_{gr} and the dominant collision process is quasielastic reactions. In the quasielastic process, a small fraction of the kinetic energy gets converted into internal excitation energies, which include inelastic excitations and transfer reactions. If the impact parameter is very large ($b > b_{gr}$) the collision process is dominated by elastic (Rutherford) scattering, and the reaction partners get excited due to the Coulomb repulsion. If the impact parameter,

$b < b_{gr}$ the nuclear interaction overcomes the Coulomb repulsion and are usually known as deep inelastic collisions (DIC). In such collisions, a considerable quantity of kinetic energy and angular momentum are transferred from the relative motion to the intrinsic excitations of the colliding ions. Though considerable mass and energy exchange may have occurred, the collision partners hold their identities, and the reaction leads to fragments that may be identified as target-like or projectile-like. The head-on collisions lead to the fusion of the projectile and the target nuclei and form a composite system. The fused composite system equilibrates in all degrees of freedom and forms the intermediate state known as the compound nucleus (CN). The formed CN is in a highly excited state and it decays by the emission of light particles or fission. During the fusion processes, the available kinetic energy is completely turned into the intrinsic excitation energy of the CN, and all the angular momenta can be converted into the spin of the fused nuclei.

The type of reaction that may occur between two heavy nuclei can be related to the entrance channel angular momentum [2]. The impact parameters b are related to the relative angular momenta, ℓ , of the entrance channel by the semi-classical relation,

$$\ell = \frac{b}{\lambda} \tag{1.1}$$

where λ is the reduced wavelength. The angular momentum limits for the reaction components are determined from a sharp cutoff model. This approach have some inconsistency, in reality, the angular momentum limits to the various reaction categories are not sharp. In Fig. 1.2, we show various reaction mechanisms as a function of angular momentum. The nuclear reactions do not occur above a certain angular momentum, ℓ_{max} , above which the collision processes are dominant with Coulomb excitation (CE) and elastic (EL) processes. Various types of damped reactions may occur between the angular momentum ℓ_f and ℓ_{max} values. In this type of reaction, the collision partners preserve their identity,

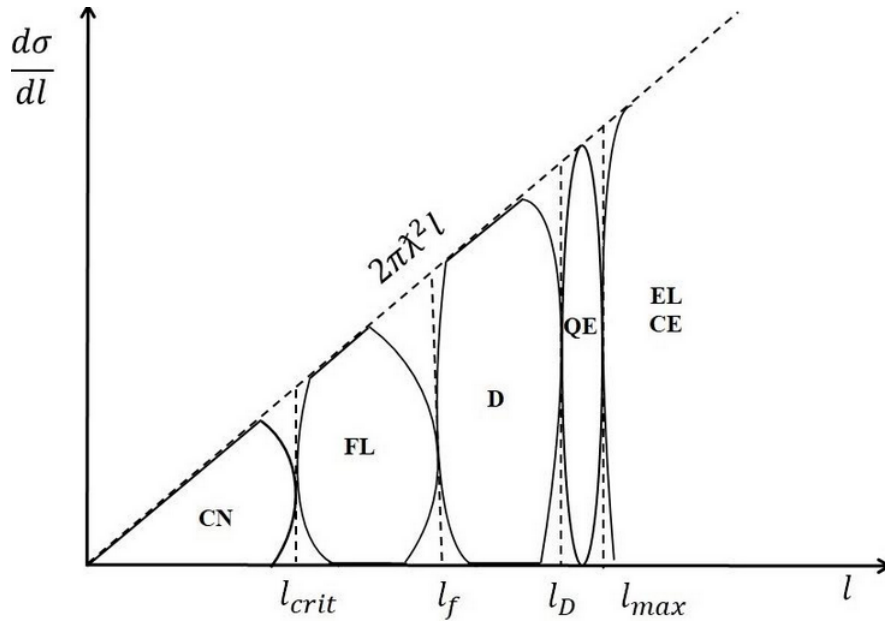


Figure 1.2: Schematic illustration of the ℓ dependence of the partial cross section for compound nucleus (CN), fusion-like (FL), damped (D), quasielastic (QE), Coulomb excitation (CE) and elastic (EL) processes. The long-dashed line represents the geometrical partial cross section. Vertical dashed lines represent the extensions of the various ℓ windows in a sharp cutoff model.

even though considerable mass and energy exchange may have occurred between the target and projectile nuclei, and the reaction products may be identified as target-like or projectile-like.

Below a certain angular momentum ℓ_f , the trajectory of the system is influenced by a conditional saddle in the internuclear potential energy surface [2]. The conditional saddle is a saddle at frozen mass asymmetry. The conditional saddle point is not a true saddle since the potential energy there is not stationary in the mass asymmetry coordinate. The unconditional or fission saddle is a stationary point for all coordinates in the potential surface. The conditional saddle could have a considerable influence on the reaction trajectory. Since mass asymmetry is a slowly evolving parameter, the conditional saddle causes a considerable increase in the reaction time. This allows both the evolution of the system to shapes that no longer describe separate nuclei and a relaxation of the mass asymmetry [2]. The formed composite system is termed as “mononucleus” by Swiatecki [3]. Mononucleus is a nuclear configuration without a pronounced

neck, trapped inside the conditional saddle.

Effective fissility parameter χ_{eff} is related to repulsive and attractive forces in the entrance channel, which is proportional to the ratio of the electric repulsion to the nuclear attraction for di-nuclear configurations. Blocki *et al.* [4] has defined the effective fissility parameter as

$$\chi_{eff} = \frac{(Z^2/A)_{eff}}{(Z^2/A)_{crit}} \quad (1.2)$$

where

$$(Z^2/A)_{eff} = \frac{4Z_P Z_T}{A_P^{1/3} A_T^{1/3} (A_P^{1/3} + A_T^{1/3})} \quad (1.3)$$

and

$$(Z^2/A)_{crit} = 50.883 \left[1 - 1.782612 \left(\frac{N - Z}{A} \right)^2 \right] \quad (1.4)$$

For heavy systems, having $(Z^2/A)_{eff}$ sufficiently large, the fusion cross section measurements may be influenced by the dynamical entrance-channel effects, and the “mononucleus” reactions may not be identical to the compound nucleus reactions. In terms of the entrance channel angular momentum, the “mononucleus” reactions outside the fission saddle occur between angular momenta ℓ_f and ℓ_{crit} and are termed as fusion-like (FL) processes.

The compound nucleus reactions occur at angular momenta less than ℓ_{crit} . For light systems with sufficiently small $(Z^2/A)_{eff}$, and at a low ℓ value, the conditional saddle will not affect the trajectories, and all “mononucleus” reactions are compound nucleus reactions. For light systems with sufficiently small $(Z^2/A)_{eff}$ value, the values of ℓ_f and ℓ_{crit} are the same, which means all mononucleus reactions are compound nucleus reactions.

1.2 Heavy ion fusion reactions

When two heavy ions approach each other, they experience strong Coulomb repulsion due to the positive charge of the nuclei and an attractive nuclear force. In addition to the Coulomb and nuclear potentials, a repulsive centrifugal potential also contributes to the total effective potential. The total effective potential can be written as,

$$V = V_C + V_N + V_{Cent} \quad (1.5)$$

where V_C is the repulsive Coulomb potential,

$$V_C = \begin{cases} \frac{1.438Z_P Z_T}{r} & r > R_C \\ \frac{1.438Z_P Z_T}{2R_C} \left(3 - \frac{r^2}{R_C^2}\right) & r < R_C \end{cases} \quad (1.6)$$

R_C is the charge radius.

V_N is the attractive nuclear potential in the entrance channel. Woods-Saxon parametrization for the nuclear potential is

$$V_N = \frac{-V_0}{1 + \exp((r - R_0)/a)} \quad (1.7)$$

V_0 is the depth parameter of the Woods-Saxon potential, R_0 is the radius parameter and a is the surface diffuseness parameter.

V_{Cent} is the repulsive centrifugal potential

$$V_{Cent} = \frac{\hbar^2 \ell(\ell + 1)}{2\mu r^2} \quad (1.8)$$

The competition between the repulsive Coulomb potential and the attractive nuclear potential produces a barrier called fusion barrier with an energy pocket inside it. Due to the effects of repulsive centrifugal force at higher angular momenta, the barrier height will increase and decrease the depth of the energy pocket.

Fusion is the process of amalgamation of two or more nuclei to form a single heavier nucleus. Fusion is possible only when the system overcomes the Coulomb barrier. After overcoming the Coulomb barrier, the projectile-target system gets captured or trapped inside the attractive potential pocket. Capture is the first step towards the fusion process. During the reaction, nucleons are exchanged between the target and projectile, which results in the transfer of energy and angular momentum from the relative motion to the intrinsic degrees of freedom of the composite system [2]. The fused composite system equilibrates in all degrees of freedom, such as energy, shape, and N/Z ratio, and forms an intermediate system called the compound nucleus (CN). If the nucleus does not hold together long enough to equilibrate in all degrees of freedom, it does not reach statistical or thermal equilibrium, so the fusion process is inherently a slow process [5]. The compound nuclear lifetime lies between 10^{-19} s and 10^{-16} s, which is longer than the time required for the incident particle to travel across the diameter of the target nucleus, i.e., about 10^{-22} s. Depending upon the incident energy of the projectile, the formed compound nucleus has a certain amount of excitation energy and a broad angular momentum distribution. The kinetic energy of the projectile is converted into the excitation energy and angular momentum of the compound nucleus. The excited CN decays to the ground state by the emission of several particles called fusion evaporation or fusion-fission. The decay of formed CN is independent of its mode of formation [6]. In the fusion evaporation process, the excited CN decays by the emission of light particles such as neutron, proton, alpha, and γ ray, which leads to the formation of a cold residual nucleus. The bound residual nucleus is called evaporation residue (ER). The mass of the ER is slightly lower than that of the compound nucleus. For a lighter system, the dominant decay mode is evaporation. Hence, ERs are the unambiguous signatures of CN formation. When the compound nucleus is medium heavy, the fission process competes strongly with the evaporation of particles in each stage of the evaporation process. So, the total fusion cross section (σ_{fus}) is given by

the sum of the ER cross section (σ_{ER}) and fission cross section (σ_{fiss}).

$$\sigma_{fus} = \sigma_{ER} + \sigma_{fiss} \quad (1.9)$$

In addition to the excitation energy and angular momentum, the decay mode is governed by the statistical properties of nuclei. A schematic representation of compound nucleus formation and its decay is shown in Fig. 1.3.

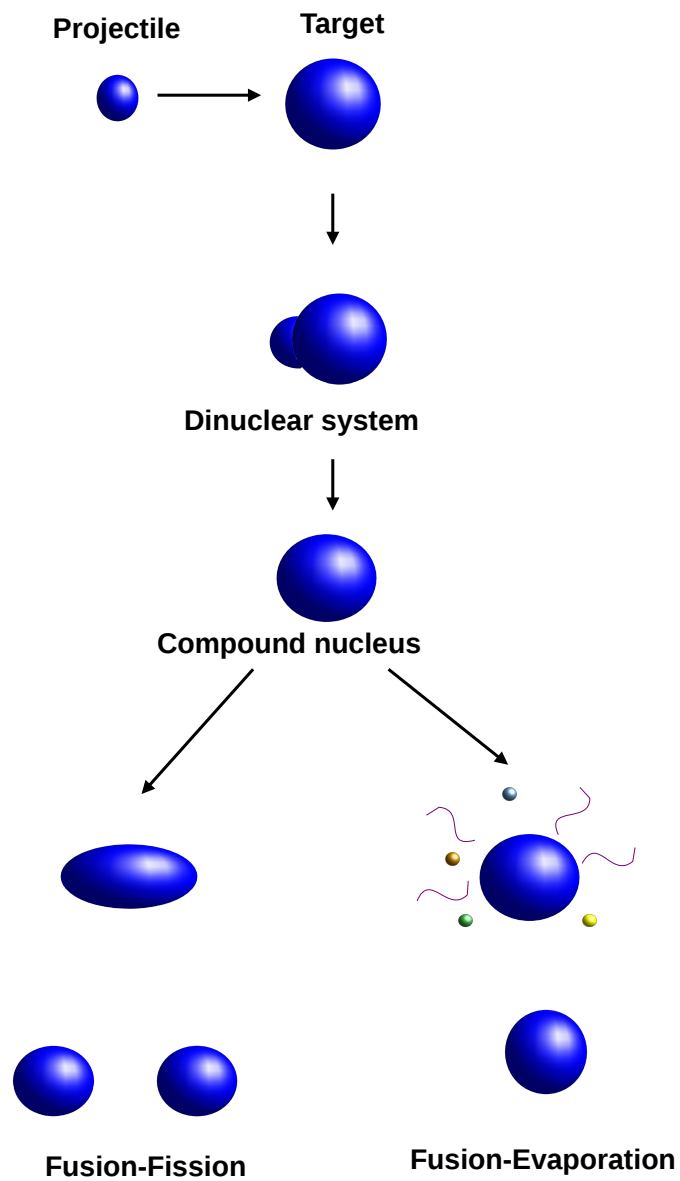


Figure 1.3: Schematic representation of the compound nucleus formation and decay.

In a fusion-fission process, the compound nucleus splits up into two or more. These fission fragments are repelled from each other by a repulsive Coulomb force. As a result, total kinetic energy is independent of the initial compound nucleus excitation energy. Therefore, the excitation energy of the fission fragments is proportional to the compound nucleus excitation energy [7]. The excited fission fragments decay via emission of particles and γ rays. These emitted particles are called “post-scission” particles and the particles emitted before the scission, i.e., during the fission process by the fissioning nucleus, are called “pre-scission” particles. Fission takes over the particle evaporation at higher energies and angular momenta. In the case of heavier nuclei, the CN decay competes with the fission.

The ER cross section can be written as the product of capture cross sections (σ_{cap}), CN formation probability (P_{CN}), and the survival probability (W_{sur}) of the completely fused system against fission.

$$\sigma_{ER} = \sigma_{cap} P_{CN} W_{sur} \quad (1.10)$$

P_{CN} is the probability that the di-nuclear system crosses the inner fusion barrier and forms the CN. W_{sur} is the survival probability of the completely fused system against fission. In the case of mass asymmetric systems, especially for fusion reactions with light and medium nuclei, the compound nucleus formation probability is close to unity ($P_{CN} \approx 1$). For heavier systems, depending upon the energy, angular momentum, mass asymmetry of the entrance channel, etc, after capture processes the composite system may evolve either towards a fully equilibrated CN or re-separates before achieving complete equilibration. These non-equilibrated processes are known as the non-compound nuclear fission (NCNF) processes.

1.3 Non-compound nuclear fission processes

Non-compound nuclear fission (NCNF) processes are the major obstacles to the formation of superheavy elements (SHE). The NCNF processes will occur at higher excitation energies and angular momenta. At higher excitation energies for reactions using heavier projectiles, the conditional saddle is higher than the unconditional saddle, and the system needs additional energy (extra push) to pass this saddle. After crossing the conditional saddle, the system equilibrates in all degrees of freedom except shape. Because of the dissipative losses incurred during this stage, the system fails to pass the unconditional inner saddle and moves toward re-separation. The CN formation processes occur below ℓ_{crit} and it cannot carry too much angular momentum. Ngô *et al.* [8] described the results of a dynamical model for dissipative heavy ion collisions which showed that a fused trajectory can lead either to a compound nucleus or to a NCNF processes. According to Ngô *et al.* [9], there are four types of dissipative reactions in heavy ion collisions, such as deep inelastic collision, fast fission, quasifission (QF), and pre-equilibrium fission. Fast fission, quasifission (QF) and pre-equilibrium fission come under the category of NCNF processes.

Pre-equilibrium fission: Ramamurthy and Kapoor [10] proposed the concept of pre-equilibrium fission process to explain the anomalous angular anisotropies observed in many heavy ion fusion-fission reactions. According them, a composite system that has equilibrated in all degrees of freedom except the K degree of freedom, where K is the projection of the total angular momentum J on the nuclear symmetry axis, will re-separate in a very short interval of time. The main difference between CN fission and pre-equilibrium fission is that in the latter case the K degree of freedom is not equilibrated and the fission occurs before 8×10^{-21} seconds.

Fast fission: Fast fission processes are dominant at higher beam energies and the systems with greater fissility. The fission barrier of the composite system decreases with an increase in angular momentum values and vanishes at certain ℓ values which may be lower than ℓ_{crit} . Hence the composite system cannot

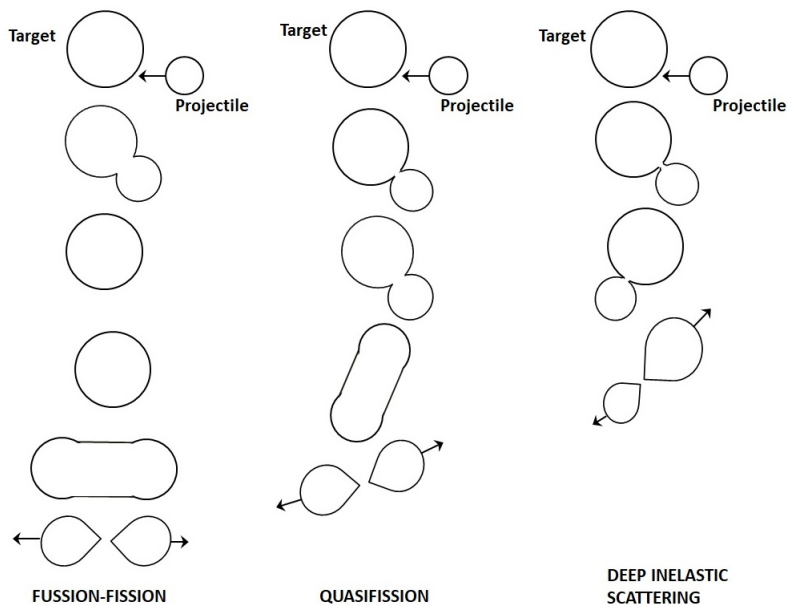


Figure 1.4: Schematic illustration of fusion-fission, quasifission and deep inelastic scattering in a heavy ion reactions.

get trapped inside the fission barrier and gets separated into fission-like fragments [11]. This process appears as a kind of delayed deep inelastic process. The reaction time for this process, which is of the order 10^{-21} to 10^{-20} s.

Quasifission: In terms of reaction time scales, quasifission bridges the gap between deep inelastic collisions and CN formation, which originates due to the compact saddle point configuration of the system compared to the contact configuration. The difference between fusion-fission, quasifission, and deep inelastic scattering in a heavy ion reactions are shown as a schematic in Fig. 1.4.

The competition between complete fusion and quasifission processes is influenced by entrance channel properties such as the charge product of the projectile and target ($Z_P Z_T$), the deformations of the colliding partners, and the entrance channel mass asymmetry ($\alpha = \frac{A_P - A_T}{A_P + A_T}$, where A_P and A_T are the mass numbers of projectile and target respectively). The highest of all conditional saddle point is called Businaro-Gallone saddle point [12] and the corresponding mass asymmetry is called Businaro-Gallone critical mass asymmetry, (α_{BG}), ie., a point where potential is maximum for a given fissility. According to the Businaro-Gallone [12] criterion, Quasifission (QF) appears for systems with $\alpha < \alpha_{BG}$.

The experimental signatures of quasifission includes a strong mass-angle correlation, broadened fragment mass widths, larger angular anisotropies and a reduction in the ER cross sections [13]. From the analysis of a large data set of mass-angle distributions of fission-like fragments obtained in heavy ions reactions, du Rietz *et al.* [14] found that QF appears for the reactions with mean fissility parameter $\chi_m > 0.68$ and QF becomes dominant at $\chi_m > 0.765$. The mean fissility is a linear combination of compound nucleus fissility χ_{CN} and the effective fissility χ_{eff} and given by [14],

$$\chi_m = 0.75\chi_{eff} + 0.25\chi_{CN} \quad (1.11)$$

1.4 Motivation of the present work

Heavy ion fusion reaction is a complex many-body process. Considerable experimental and theoretical efforts has been received in the field of heavy ion fusion reactions. Heavy ion fusion studies can provide important insights into the reaction dynamics and decay properties of excited compound nuclei (CN) [15–24]. Evaporation residue (ER) measurement is a powerful method for studying fusion processes in mass asymmetric projectile-target systems. Fission fragments must be taken into account when calculating total fusion cross sections and understanding the dynamics of the CN de-excitation. The statistical-model framework has been used to describe the de-excitation of the composite system, such as the emission of light particles and γ -rays with competition from the fission processes. Even though the fundamental concepts of composite system de-excitation are relatively well understood by statistical model calculations, some fission fragment angular anisotropies and ER measurements have been found to deviate from statistical model calculations [25–27].

Experimental fusion cross section in comparison with coupled-channel calculations would provide information regarding the effect of projectile/target deformations as well as the coupling of the inelastic channels to the fusion process. At

the higher excitation energy, the one-dimensional barrier penetration model (1D-BPM) explains nuclear fusion quite reasonably. However, 1D-BPM fails to reproduce the enhanced sub-barrier fusion cross sections. The enhanced sub-barrier fusion cross sections were found to be due to the coupling of the internal degrees of freedom, such as static deformation of the collision partners, collective surface vibrations and transfer channels [28]. Tunneling through a multidimensional potential barrier successfully explains the observed experimental sub-barrier fusion enhancement [15].

The experimental observation of an asymmetric fission of ^{180}Hg [29] led to study of the fission of Hg nuclei both theoretically and experimentally [30–43]. Andreev *et al.* [36] calculated the mass distributions for fission of different Hg isotopes using the improved scission-point model and compared the results with the experimental data [44]. They found that the mass distribution is quite asymmetric for ^{180}Hg and ^{184}Hg . For ^{188}Hg the asymmetry is less pronounced. In the case of $^{192,196}\text{Hg}$ and ^{198}Hg the mass distribution looks more symmetric but with a dip on the top. Their calculated mass distributions of fission fragments for induced fission of $^{180,184,188,192,196}\text{Hg}$ shown in Fig. 1.5.

Prasad *et al.* [32] observed mass asymmetric fission in neutron deficient ^{182}Hg nuclei populated by heavy ion fusion. They suggested that the observed asymmetric fission in ^{182}Hg and its absence in ^{195}Hg is due to the difference in the dynamical evolution of ^{182}Hg and ^{195}Hg CN. Hg nuclei exhibit structural changes as one goes from neutron deficient ^{180}Hg to relatively neutron rich ^{198}Hg nuclei. Kozulin *et al.* [30] studied the dependence of the symmetric and asymmetric fission of $^{180,182,183}\text{Hg}$ and ^{178}Pt nuclei as a function of excitation energy and isospin. They found that the existence of a well deformed proton shell at $Z \approx 36$ and less deformed proton shell at $Z \approx 46$ as responsible for the new type of asymmetric fission. Bogachev *et al.* [31] observed that proton numbers play a stabilizing role in the asymmetric fission of excited pre-actinide nuclei. Also, they found that the yield of symmetric fission for ^{190}Hg , formed in the $^{36}\text{Ar}+^{154}\text{Sm}$ reaction, is lower than for ^{180}Hg , formed in the $^{36}\text{Ar}+^{144}\text{Sm}$ reaction, at the same excitation

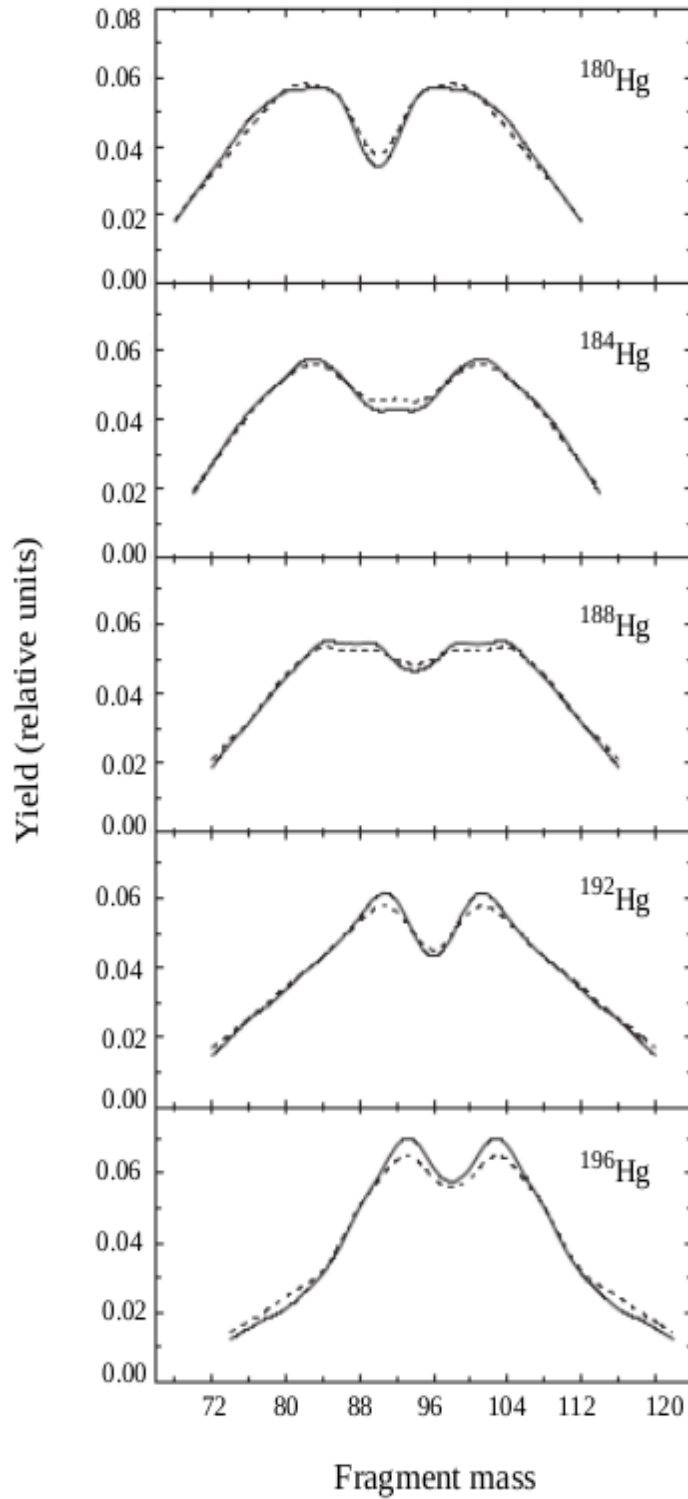


Figure 1.5: Calculated mass distributions of fission fragments for induced fission of $^{180,184,188,192,196}\text{Hg}$ with bombarding energies of 10 MeV (solid lines) and 30 MeV (dashed lines) above the corresponding Coulomb barriers for spherical nuclei (Reproduced from [36]).

energies of CN at the saddle point. Kozulin *et al.* [45] observed a large contribution (more than 70%) of quasifission (QF) in the case of $^{68}\text{Zn}+^{112}\text{Sn}$ reaction. However QF was not observed in the case of $^{36}\text{Ar}+^{144}\text{Sm}$ reaction forming the same CN [33, 43, 46]. du Rietz *et al.* [14] analyzed large set of experimental mass-angular distributions of fission-like fragments and found that the threshold value for the QF appearance for composite systems with $Z_{CN} = 80$ is $Z_P Z_T = 1450 \pm 100$ (where Z_{CN} , Z_P and Z_T are the atomic number of the CN, projectile and target respectively). Also, they reported that QF appears for the reactions with mean fissility parameter $\chi_m > 0.68$ and QF becomes dominant at $\chi_m > 0.765$. In the case of $^{68}\text{Zn}+^{112}\text{Sn}$, the value of χ_m (0.695) and the $Z_P Z_T$ (1500) are close to the threshold values for the onset of the QF processes. So such a large contribution of QF was unexpected. Kaur *et al.* [47] measured ER cross sections for $^{48}\text{Ti}+^{140,142}\text{Ce}$ reactions forming $^{188,190}\text{Hg}$ CN, to understand the influence of neutron shell closure of target nuclei on CN formation. They observed that the effects of shell closure in the target nucleus on fusion cross sections is negligible. Further, they found no evidence of QF processes in the $^{48}\text{Ti}+^{140,142}\text{Ce}$ systems. Sikkeland *et al.* [48] have measured the fission excitation function for $^{12}\text{C}+^{182}\text{W}$ reaction. Andersen *et al.* [49] measured fission cross sections and fission angular distributions for $^{12}\text{C}+^{182,183,184,186}\text{W}$ reactions. Rajagopalan *et al.* [50] measured evaporation residues (ER), fission fragments (FF), and charged particle emission for the systems $^{12}\text{C}+^{182}\text{W}$, $^{19}\text{F}+^{175}\text{Lu}$, $^{20}\text{Ne}+^{174}\text{Yb}$ and $^{40}\text{Ar}+^{154}\text{Sm}$ forming ^{194}Hg at excitation energies ranging from 57 to 195 MeV. In the case of $^{12}\text{C}+^{182}\text{W}$ reaction, the measured fusion cross sections overestimated by calculations based on systematics and various theoretical models. However, measurements with heavier projectiles, ^{19}F , ^{20}Ne , and ^{40}Ar , all show reasonable agreement with the calculated cross sections. This discrepancy in the case of $^{12}\text{C}+^{182}\text{W}$ was attributed to missing ER events due to small recoil energies in their detection system. Furthermore, Rajagopalan *et al.* have shown that non-equilibrium mechanisms have a bigger role in the ER cross sections in the case of ^{12}C and ^{19}F in comparison to ^{40}Ar induced reactions.

Delagrang *et al.* [51] used a time-of-flight setup to measure the ER events in $^{12}\text{C}+^{181}\text{Ta}$ and $^{12}\text{C}+^{182,186}\text{W}$ reactions to investigate the inconsistency between measurements and calculations. Their measurements observed similar cross sections as Rajagopalan *et al.* [50]. Also, Delagrang *et al.* measured fission cross sections for $^{12}\text{C}+^{182,186}\text{W}$ reactions in the 56-87 MeV excitation energies. They observed a significant difference in the fission yield of ^{194}Hg CN in comparison to ^{198}Hg compound nuclei at $E^* = 82$ MeV ($\sigma_{fiss} = 536 \pm 52$ mb for ^{194}Hg and $\sigma_{fiss} = 166 \pm 68$ mb for ^{198}Hg). One of the explanations given for this discrepancy is that it is caused by the competition between evaporation of neutrons and fission. Stokstad *et al.* [26] reported lower values of the fusion cross sections for $^{40}\text{Ar}+^{144,148}\text{Sm}$ at higher excitation energies compared to $^{40}\text{Ar}+^{154}\text{Sm}$, which formed $^{184,188,194}\text{Hg}$ respectively. They suggested that the lowering of the cross sections for $^{40}\text{Ar}+^{144,148}\text{Sm}$ could be a result of the dynamic effects such as deformation or orientation of the target nuclei before fusion or the distortion of the target nucleus in the Coulomb field of the projectile.

Miller *et al.* [52] reported that the probability of ^1H and ^4He evaporation from ^{194}Hg CN increases rapidly with energy and appears to protect the system from fission. Rajagopalan *et al.* [50] confirmed that most ^1H and ^4He are evaporated prior to fission. Alexander *et al.* [53] have unfolded the effects of excitation energy and spin on the decay of ^{194}Hg CN. They suggested that at higher excitation energies ($E^* > 98$ MeV), the competition between fission and evaporation is highly sensitive to the relative values of the level densities. In order to study the spin dependence of dissipation effects in fission, Hui *et al.* [54] measured ER excitation function in coincidence with γ -ray multiplicity for the $^{19}\text{F}+^{175}\text{Lu}$ reaction forming ^{194}Hg CN. Their measurements show that there is no dissipation effects in the pre-saddle region of the fission processes.

Calculated fusion cross sections based on various theoretical models and systematics showed large deviation with respect to measured cross sections for $^{12}\text{C}+^{182,186}\text{W}$ reactions [50, 51] in the laboratory energy range 77 to 167 MeV. However, fusion cross section measurements with heavier projectiles forming

^{194}Hg CN follow the fusion systematics [50]. This necessitated measuring the ER cross sections for $^{12}\text{C}+^{182,184,186}\text{W}$ forming $^{194,196,198}\text{Hg}$ nuclei to study the observed discrepancies between the measurements and predicted cross sections.

1.5 Present study

Large deviations in fusion measurements for $^{12}\text{C}+^{182,186}\text{W}$, from calculations based on various theoretical models and by fusion systematics is reported by Rajagopalan *et al.* [50] and Delagrange *et al.* [51]. However, other reactions using heavier projectiles leading to the formation of the same CN agree calculations based on various theoretical models and by fusion systematics. This scenario demanded us to measure the ER cross sections for $^{12}\text{C}+^{182,184,186}\text{W}$ forming $^{194,196,198}\text{Hg}$ nuclei. Rajagopalan *et al.* [50] and Delagrange *et al.* [51] carried out the investigations in the energy range 77 to 167 MeV in the laboratory energy frame for $^{12}\text{C}+^{182,186}\text{W}$ reactions. Due to the small kinetic energy of the ERs, no data for near and below the Coulomb barrier energies were available in either measurement. For the first time, we are measuring the fusion-evaporation residues for the reactions $^{12}\text{C}+^{184}\text{W}$ and we are extending the ER measurements for $^{12}\text{C}+^{182,186}\text{W}$ over a wide range of excitation energies, to understand the fission-evaporation competition.

The current study was undertaken to address the fusion dynamics in the ^{12}C -induced reactions and compare them with the coupled-channel and statistical model calculations. In order to study the effects of target/projectile deformation effects on fusion cross sections, the measured fusion cross sections for $^{12}\text{C}+^{182,184,186}\text{W}$ are compared with the coupled-channel calculations. To understand the detailed compound nuclear decay processes, we have carried out the statistical model calculations for these reactions.

The other aspect of this thesis is to study the variation of probability of compound nucleus formation (P_{CN}) with the effective fissility parameter (χ_{eff}) and the entrance-channel mass asymmetry (α) and to look for any system-

atic, that may follow the Hg CN. We performed statistical model calculations for $^{90}\text{Zr}+^{90-96}\text{Zr}$ [55–57], $^{40}\text{Ar}+^{144-154}\text{Sm}$ [26], $^{124,130,134}\text{Te}+^{58,64}\text{Ni}$ [58], $^{14}\text{N}+^{181}\text{Ta}$ [59], $^{19}\text{F}+^{175}\text{Lu}$ [54] and $^{86}\text{Kr}+^{99-104}\text{Ru}$ [60] reactions, in addition to our measurements for $^{12}\text{C}+^{182,184,186}\text{W}$, to obtain a detailed analysis of the decay properties of the neutron deficient as well as neutron-rich Hg CN.

1.6 Plan of the thesis

The aim of this thesis is to investigate the dynamics of heavy ion fusion at energies below and near the Coulomb barrier in the ^{12}C -induced reactions. A mass spectrometer was used to measure the evaporation residues for the $^{12}\text{C}+^{182,184,186}\text{W}$ reactions. The measurements ranged from 12 % below to 45 % above the Coulomb barrier energies. The measured fusion cross sections are compared with coupled-channel and statistical model calculations.

A general introduction and literature survey of the present thesis are described in Chapter 1, Chapter 2 gives a brief review of theoretical models that are relevant to this work. In Chapter 3, we discuss the experimental setup, detectors, and electronics used in the present measurements. In Chapter 4 we present the data analysis and obtained cross sections compared with coupled-channel calculations and statistical model calculations. Chapter 5 deals with the systematic analysis to explore the variation of fusion probability with mass asymmetry and effective fissility parameters. In Chapter 6, we present a summary of the thesis and the scope of future works.

Bibliography

- [1] C. Y. Wong, Phys. Rev. Lett. **31**, 766 (1973).
- [2] J. R. Birkelund and J. R. Huizenga, Annu. Rev. Nucl. Part. Sci. **33**, 265 (1983).
- [3] W. J. Swiatecki, Nucl. Phys. A **376**, 275 (1982).
- [4] J. P. Blocki, H. Feldmeier, and W. J. Swiatecki, Nucl. Phys. A **459**, 145 (1986).
- [5] T. D. Thomas, Annu. Rev. Nucl. Sci **18**, 343 (1968).
- [6] N. Bohr, Nature **137**, 344 (1936).
- [7] P. Paul and M. Thoennessen, Annu. Rev. Nucl. Part. Sci. **44**, 65 (1994).
- [8] C. Ngô, C. Gregoire, B. Remaud, and E. Tomasi, Nucl. Phys. A **400**, 259 (1983).
- [9] C. Ngô, Prog. Part. Nucl. Phys. **16**, 139 (1986).
- [10] V. S. Ramamurthy and S. S. Kapoor, Phys. Rev. Lett. **54**, 178 (1985).
- [11] B. Borderie, M. Berlinger, D. Gardès, F. Hanappe, L. Nowicki, J. Péter, B. Tamain, S. Agarwal, J. Girard, C. Grégoire, J. Matuszek, and C. Ngô, Z. Phys. A At. nucl. **299**, 263 (1981).
- [12] U. L. Businaro and S. Gallone, Il Nuovo Cimento (1955-1965) **5**, 315 (1957).
- [13] R. G. Thomas, Pramana - J. Phys **85**, 303 (2015).
- [14] R. du Rietz, E. Williams, D. J. Hinde, M. Dasgupta, M. Evers, C. J. Lin, D. H. Luong, C. Simenel, and A. Wakhle, Phys. Rev. C **88**, 054618 (2013).

- [15] M. Dasgupta, D. J. Hinde, N. Rowley, and A. M. Stefanini, *Annu. Rev. Nucl. Part. Sci* **48**, 401 (1998).
- [16] B. B. Back, H. Esbensen, C. L. Jiang, and K. E. Rehm, *Rev. Mod. Phys.* **86**, 317 (2014).
- [17] P. Kaur, M. Maiti, T. N. Nag, and S. Sodaye, *Phys. Rev. C* **105**, 014629 (2022).
- [18] R. N. Sagaidak, M. L. Chelnokov, V. I. Chepigin, V. A. Gorshkov, O. N. Malyshev, A. G. Popeko, A. I. Svirikhin, and A. V. Yeremin, *Phys. Rev. C* **105**, 024604 (2022).
- [19] F. Gollan, D. Abriola, A. Arazi, M. A. Cardona, E. de Barbará, J. de Jesús, D. Hojman, R. M. I. Betan, J. Lubian, A. J. Pacheco, B. Paes, D. Schneider, and H. O. Soler, *Phys. Rev. C* **104**, 024609 (2021).
- [20] N. Wang and W. Ye, *Phys. Rev. C* **103**, 024611 (2021).
- [21] J. Gehlot, A. M. Vinodkumar, N. Madhavan, S. Nath, A. Jhingan, T. Varughese, T. Banerjee, A. Shamlath, P. V. Laveen, M. Shareef, P. Jisha, P. S. Devi, G. N. Jyothi, M. M. Hosamani, I. Mazumdar, V. I. Chepigin, M. L. Chelnokov, A. V. Yeremin, A. K. Sinha, and B. R. S. Babu, *Phys. Rev. C* **99**, 034615 (2019).
- [22] S. Nath, P. V. M. Rao, S. Pal, J. Gehlot, E. Prasad, G. Mohanto, S. Kalkal, J. Sadhukhan, P. D. Shidling, K. S. Golda, A. Jhingan, N. Madhavan, S. Muralithar, and A. K. Sinha, *Phys. Rev. C* **81**, 064601 (2010).
- [23] Kavita, K. S. Golda, T. K. Ghosh, A. Jhingan, P. Sugathan, A. Chatterjee, B. R. Behera, A. Kumar, R. Kumar, N. Saneesh, M. Kumar, A. Yadav, C. Yadav, N. Kumar, A. Banerjee, A. Rani, S. K. Duggi, R. Dubey, K. Rani, S. Noor, J. Acharya, and H. Singh, *Phys. Rev. C* **100**, 024626 (2019).

- [24] P. Jisha, A. M. Vinodkumar, B. R. S. Babu, S. Nath, N. Madhavan, J. Gehlot, A. Jhingan, T. Banerjee, I. Mukul, R. Dubey, N. Saneesh, K. M. Varier, E. Prasad, A. Shamlath, P. V. Laveen, and M. Shareef, *Phys. Rev. C* **101**, 024611 (2020).
- [25] B. B. Back, D. J. Blumenthal, C. N. Davids, D. J. Henderson, R. Hermann, D. J. Hofman, C. L. Jiang, H. T. Penttilä, and A. H. Wuosmaa, *Phys. Rev. C* **60**, 044602 (1999).
- [26] R. G. Stokstad, W. Reisdorf, K. D. Hildenbrand, J. V. Kratz, G. Wirth, R. Lucas, and J. Poitou, *Z. Phys. A* **295**, 269 (1980).
- [27] A. Shrivastava, S. Kailas, A. Chatterjee, A. M. Samant, A. Navin, P. Singh, and B. S. Tomar, *Phys. Rev. Lett.* **82**, 699 (1999).
- [28] K. Hagino and N. Takigawa, *Prog. Theor. Phys* **128**, 1061 (2012).
- [29] A. N. Andreyev, J. Elseviers, M. Huyse, P. Van Duppen, S. Antalic, A. Barzakh, N. Bree, T. E. Cocolios, V. F. Comas, J. Diriken, D. Fedorov, V. Fedosseev, S. Franchoo, J. A. Heredia, O. Ivanov, U. Köster, B. A. Marsh, K. Nishio, R. D. Page, N. Patronis, M. Seliverstov, I. Tsekhanovich, P. Van den Bergh, J. Van De Walle, M. Venhart, S. Vermote, M. Veselsky, C. Wagemans, T. Ichikawa, A. Iwamoto, P. Möller, and A. J. Sierk, *Phys. Rev. Lett.* **105**, 252502 (2010).
- [30] E. M. Kozulin, G. N. Knyazheva, I. M. Itkis, M. G. Itkis, Y. S. Mukhamejanov, A. A. Bogachev, K. V. Novikov, V. V. Kirakosyan, D. Kumar, T. Banerjee, M. Cheralu, M. Maiti, R. Prajapat, R. Kumar, G. Sarkar, W. H. Trzaska, A. N. Andreyev, I. M. Harca, A. Mitu, and E. Vardaci, *Phys. Rev. C* **105**, 014607 (2022).

- [31] A. A. Bogachev, E. M. Kozulin, G. N. Knyazheva, I. M. Itkis, M. G. Itkis, K. V. Novikov, D. Kumar, T. Banerjee, I. N. Diatlov, M. Cheralu, V. V. Kirakosyan, Y. S. Mukhamejanov, A. N. Pan, I. V. Pchelintsev, R. S. Tikhomirov, I. V. Vorobiev, M. Maiti, R. Prajapat, R. Kumar, G. Sarkar, W. H. Trzaska, A. N. Andreyev, I. M. Harca, and E. Vardaci, *Phys. Rev. C* **104**, 024623 (2021).
- [32] E. Prasad, D. J. Hinde, K. Ramachandran, E. Williams, M. Dasgupta, I. P. Carter, K. J. Cook, D. Y. Jeung, D. H. Luong, S. McNeil, C. S. Palshetkar, D. C. Rafferty, C. Simenel, A. Wakhle, J. Khuyagbaatar, C. E. Düllmann, B. Lommel, and B. Kindler, *Phys. Rev. C* **91**, 064605 (2015).
- [33] K. Nishio, A. N. Andreyev, R. Chapman, X. Derkx, C. E. Dllmann, L. Ghys, F. P. Heberger, K. Hirose, H. Ikezoe, J. Khuyagbaatar, B. Kindler, B. Lommel, H. Makii, I. Nishinaka, T. Ohtsuki, S. D. Pain, R. Sagaidak, I. Tsekhanovich, M. Venhart, Y. Wakabayashi, and S. Yan, *Phys. Lett. B* **748**, 89 (2015).
- [34] S. Panebianco, J.-L. Sida, H. Goutte, J.-F. m. c. Lemaître, N. Dubray, and S. Hilaire, *Phys. Rev. C* **86**, 064601 (2012).
- [35] H. Paşca, A. V. Andreev, G. G. Adamian, and N. V. Antonenko, *Phys. Rev. C* **101**, 064604 (2020).
- [36] A. V. Andreev, G. G. Adamian, and N. V. Antonenko, *Phys. Rev. C* **86**, 044315 (2012).
- [37] A. V. Andreev, G. G. Adamian, N. V. Antonenko, and A. N. Andreyev, *Phys. Rev. C* **88**, 047604 (2013).
- [38] J. D. McDonnell, W. Nazarewicz, J. A. Sheikh, A. Staszczak, and M. Warda, *Phys. Rev. C* **90**, 021302 (2014).

- [39] T. Ichikawa, A. Iwamoto, P. Möller, and A. J. Sierk, *Phys. Rev. C* **86**, 024610 (2012).
- [40] P. Möller, J. Randrup, and A. J. Sierk, *Phys. Rev. C* **85**, 024306 (2012).
- [41] C. Schmitt, A. Lemasson, K.-H. Schmidt, A. Jhingan, S. Biswas, Y. H. Kim, D. Ramos, A. N. Andreyev, D. Curien, M. Ciemala, E. Clément, O. Dorvaux, B. De Canditiis, F. Didierjean, G. Duchêne, J. Dudouet, J. Frankland, B. Jacquot, C. Raison, D. Ralet, B.-M. Retailleau, L. Stuttgé, and I. Tsekhanovich, *Phys. Rev. Lett.* **126**, 132502 (2021).
- [42] M. Warda, A. Staszczak, and W. Nazarewicz, *Phys. Rev. C* **86**, 024601 (2012).
- [43] E. Prasad, D. J. Hinde, M. Dasgupta, D. Y. Jeung, A. C. Berriman, B. M. A. Swinton-Bland, C. Simenel, E. C. Simpson, R. Bernard, E. Williams, K. J. Cook, D. C. Rafferty, C. Sengupta, J. F. Smith, K. Vo-Phuoc, and J. Walshe, *Phys. Lett. B* **811**, 135941 (2020).
- [44] M. G. Itkis, N. A. Kondratev, S. I. Mulgin, V. N. Okolovich, A. Y. Rusanov, and G. N. Smirenkin, *Sov. J. Nucl. Phys.* **52**, 601 (1990).
- [45] E. M. Kozulin, E. Vardaci, W. H. Trzaska, A. A. Bogachev, I. M. Itkis, A. V. Karpov, G. N. Knyazheva, and K. V. Novikov, *Phys. Lett. B* **819**, 136442 (2021).
- [46] D. Kumar, E. M. Kozulin, M. Cheralu, G. N. Knyazheva, I. M. Itkis, M. G. Itkis, K. V. Novikov, A. A. Bogachev, N. I. Kozulina, I. N. Diatlov, I. V. Pchelintsev, I. V. Vorobiev, T. Banerjee, Y. S. Mukhamejanov, A. N. Pan, V. V. Saiko, P. P. Singh, R. N. Sahoo, A. N. Andreyev, D. M. Filipescu, M. Maiti, R. Prajapat, and R. Kumar, *Bull. Russ. Acad. Sci.: Phys* **84**, 1001 (2020).

- [47] D. P. Kaur, B. R. Behera, N. Madhavan, S. Nath, J. Gehlot, A. Kaur, Raghav, Gonika, R. Biswas, Subodh, Amit, A. Parihari, K. Rani, H. Arora, Shruti, and S. Pal, Nucl. Phys. A **1019**, 122384 (2022).
- [48] T. Sikkeland, J. E. Clarkson, N. H. Steiger-Shafir, and V. E. Viola, Phys. Rev. C **3**, 329 (1971).
- [49] J. U. Andersen, A. S. Jensen, E. Laegsgaard, K. O. Nielsen, J. S. Forster, I. V. Mitchell, D. Ward, and W. M. Gibson, Proc. Conf. on physics and chemistry of fission, 1979 **vol. I** (IAEA, Vienna 1980).
- [50] M. Rajagopalan, D. Logan, J. W. Ball, M. Kaplan, H. Delagrange, M. F. Rivet, J. M. Alexander, L. C. Vaz, and M. S. Zisman, Phys. Rev. C **25**, 2417 (1982).
- [51] H. Delagrange, A. Benachou, F. Hubert, Y. Llabador, B. Heusch, J. Coffin, P. Engelstein, P. Fintz, and G. Guillaume, Nucl. Phys. A **429**, 173 (1984).
- [52] J. M. Miller, D. Logan, G. L. Catchen, M. Rajagopalan, J. M. Alexander, M. Kaplan, J. W. Ball, M. S. Zisman, and L. Kowalski, Phys. Rev. Lett. **40**, 1074 (1978).
- [53] J. M. Alexander, H. Delagrange, M. Rajagopalan, M. F. Rivet, and L. C. Vaz, Z. Phys. A At. nucl. **307**, 149 (1982).
- [54] S. K. Hui, C. R. Bhuinya, A. K. Ganguly, N. Madhavan, J. J. Das, P. Sugathan, D. O. Kataria, S. Murlithar, L. T. Baby, V. Tripathi, A. Jhingan, A. K. Sinha, P. V. Madhusudhana Rao, N. V. S. V. Prasad, A. M. Vinodkumar, R. Singh, M. Thoennessen, and G. Gervais, Phys. Rev. C **62**, 054604 (2000).
- [55] M. Beckerman, J. Wiggins, H. Aljuwair, and M. K. Salomaa, Phys. Rev. C **29**, 1938 (1984).

- [56] J. G. Keller, K.-H. Schmidt, H. Stelzer, W. Reisdorf, Y. K. Agarwal, F. P. Hessberger, G. Münzenberg, H.-G. Clerc, and C.-C. Sahn, *Phys. Rev. C* **29**, 1569 (1984).
- [57] J. G. Keller, K. H. Schmidt, F. P. Hessberger, G. Münzenberg, W. Reisdorf, H. G. Clerc, and C. C. Sahn, *Nucl. Phys. A* **452**, 173 (1986).
- [58] D. Shapira, F. Liang, C. Gross, R. Varner, J. Beene, A. Galindo-Uribarri, J. Campo, P. Hausladen, P. Mueller, D. Stracener, J. Kolata, and H. Amro, *AIP Conf. Proc.* **853** (2006).
- [59] M. S. Asnain, M. Shuaib, I. Majeed, M. K. Sharma, V. R. Sharma, A. Yadav, D. P. Singh, P. P. Singh, U. Gupta, R. N. Sahoo, A. Sood, M. Kaushik, S. Kumar, R. Kumar, B. P. Singh, and R. Prasad, *Phys. Rev. C* **104**, 034616 (2021).
- [60] W. Reisdorf, F. P. Hessberger, K. D. Hildenbrand, S. Hofmann, G. Münzenberg, K.-H. Schmidt, W. F. W. Schneider, K. Smmerer, G. Wirth, J. V. Kratz, K. Schutt, and C.-C. Sahn, *Nucl. Phys. A* **444**, 154 (1985).

Chapter 2

Theoretical models

The study on nuclear reactions is concerned with complex many-body quantum mechanical systems. Different models are required for predicting as well as interpreting the experimental results. The standard way to address the influence of nuclear structure on heavy ion fusion reactions is the coupled-channel approach. The statistical model is one of the most successful model to understand decay of the compound nucleus. In this chapter, we describe the coupled-channel and statistical model used in the present thesis work.

2.1 One-dimensional barrier penetration model

Generally, the fundamental features of the nuclear reactions are explained in terms of an interaction that depends on the separation of the center of mass of the projectile and target. The fusion barrier referred to as the total potential possesses a maximum at a distance where the repulsive and attractive forces balance each other [1]. According to the one-dimensional barrier penetration model (1D-BPM), if the nuclei have sufficient energy to overcome the Coulomb barrier, the nuclei are to be captured and fused. Within this 1D-BPM the fusion cross section (σ_{fus}) at an energy E can be written by a summation over partial

waves [2],

$$\sigma_{fus} = \pi\lambda^2 \sum_{\ell=0}^{\infty} (2\ell + 1) T_{\ell}(E) P_{\ell}(E) \quad (2.1)$$

where λ is the asymptotic wave length, $T_{\ell}(E)$ is the transmission coefficient for the partial wave of angular momentum ℓ , $P_{\ell}(E)$ the fusion probability for the penetrating wave, and E is the energy in center of mass frame. For energies above the Coulomb barrier, many models use the sharp cutoff approximation, where fusion will occur below a certain angular momentum $\ell_{crit}(E)$ and $T_{\ell}(E)P_{\ell}(E)$ will be

$$T_{\ell}(E)P_{\ell}(E) = \begin{cases} 1, & \text{for } \ell \leq \ell_{crit}(E) \\ 0, & \text{for } \ell > \ell_{crit}(E) \end{cases}$$

which reduces Eq. 2.1 to the classical formula in the limit of $\ell_{crit}(E) \gg 1$

$$\sigma_{fus} = \pi\lambda^2 (\ell_{crit}(E) + 1)^2 \simeq \pi R_B^2 \left(1 - \frac{V_B}{E}\right) \quad (2.2)$$

where V_B is the barrier height and R_B is the radial separation.

Fusion is possible only when the system has sufficient energy to overcome the Coulomb barrier. For energies above the Coulomb barrier, the $T_{\ell}(E)P_{\ell}(E)$ will have a value of 1, while for energies below the Coulomb barrier, $T_{\ell}(E)P_{\ell}(E) = 0$. However, at energies below the Coulomb barrier, quantum mechanical tunneling is responsible for the fusion processes. The values of $T_{\ell}(E)$ are calculated from a given real potential and $P_{\ell}(E)$ are taken to be unity. The ℓ dependent potential can be approximated near its maximum by a parabola of curvature $\hbar\omega_{\ell}$. The transmission coefficient $T_{\ell}(E)$ for each partial wave can be written by the Hill-Wheeler formula [3],

$$T_{\ell}(E) = \frac{1}{1 + \exp[2\pi(V(R_{\ell}) - E)/\hbar\omega_{\ell}]} \quad (2.3)$$

where $V(R_\ell)$ is the interaction barrier for the ℓ^{th} partial wave. The frequency, ω_ℓ is related to the effective potential $V(r, \ell)$ by

$$\omega_\ell = \left| \frac{1}{\mu} \frac{d^2 V(r, \ell)}{dr^2} \right|_{R_\ell, \ell_{cr}}^{1/2} \quad (2.4)$$

Assumed that the radial separation R_ℓ , and the curvature of the barrier, $\hbar\omega_\ell$ are insensitive to ℓ . Hence,

$$V(R_\ell) \cong V_B + \frac{\hbar^2 \ell(\ell + 1)}{2\mu R_B^2} \quad (2.5)$$

and

$$\hbar\omega_\ell = \hbar\omega_0 \quad (2.6)$$

Using above approximation and replacing the summation in Eq. (2.1) by an integral one can obtain the Wong formula [4] for σ_{fus} ,

$$\sigma_{fus} = \frac{R_B^2 \hbar\omega_0}{2E} \left[1 + \exp \left\{ \frac{2\pi}{\hbar\omega_0} (E - V_B) \right\} \right] \quad (2.7)$$

For $E \gg V_B$ this equation reduced to

$$\sigma_{fus} = \pi R_B^2 \left(1 - \frac{V_B}{E} \right) \quad (2.8)$$

and for $E \ll V_B$

$$\sigma_{fus} = \frac{R_B^2 \hbar\omega_0}{2E} \exp \left[\frac{2\pi}{\hbar\omega_0} (E - V_B) \right] \quad (2.9)$$

From Eq. 2.7, it is clear that the σ_{fus} depends on the quantities, the barrier height V_B , radial position R_B , and the curvature of the potential barrier $\hbar\omega$. The 1D-BPM successfully described fusion cross sections for light nuclei and medium-heavy nuclei [1, 5]. However, sub-barrier cross sections for heavier systems show an enhancement in comparison to 1D-BPM predictions [1]. Coupled-channel

formalism is needed to describe the enhanced sub-barrier cross sections [6–9].

2.2 Coupled-channel formalism

The failure of 1D-BPM to explain the sub-barrier fusion cross section enhancement compared to the predictions from 1D-BPM leads to more microscopic description by incorporating the physical processes that influence fusion processes. Dasso *et al.* [7, 8] provided a formal basis for the effects of inelastic excitations and transfer reactions on sub-barrier fusion cross sections based on the well-known coupled-channel formalism. Through this approach, they showed that sub-barrier fusion enhancement is the consequence of coupling of the relative motion of the colliding nuclei to several nuclear intrinsic motions.

The total wave function can be expanded in terms of the channel states ϕ_ν

$$\psi^{(+)} = \sum_{\nu} \frac{\chi_{\nu}(r)}{r} \phi_{\nu} \quad (2.10)$$

where r is the separation between the center of mass of the two nuclei and (+) sign indicates the incoming wave. The wave function $\psi^{(+)}$ should satisfy the Schrödinger equation

$$[H_0 + V] \psi^{(+)} = E \psi^{(+)} \quad (2.11)$$

where H_0 is the Hamiltonian for intrinsic and relative motion and V is the interaction energy

$$\frac{d^2 \chi_{\nu}}{dr^2} + \frac{2\mu_{\nu}}{\hbar^2} [E_{\nu} - V_{\nu}^{eff}(r) \chi_{\nu}] = \frac{2\mu_{\nu}}{\hbar^2} \sum_{n \neq \nu} V_{\nu n}^{coup}(r) \chi_n \quad (2.12)$$

This is the coupled equations for the radial distorted wave functions, where

$$V_{\nu}^{eff}(r) = \frac{\hbar^2 \ell_{\nu}(\ell_{\nu} + 1)}{2\mu_{\nu} r^2} + \langle \phi_{\nu} | V | \phi_{\nu} \rangle \quad (2.13)$$

and

$$V_{\nu n}^{coup}(r) = \langle \phi_\nu | V | \phi_n \rangle, \quad \nu \neq n \quad (2.14)$$

μ_ν is the reduced mass, ℓ_ν is the partial wave and E_ν is the relative energy for a given channel ν .

Dasso *et al.* [7, 8] solved the coupled equations using the ingoing-boundary conditions. They considered the entrance channel $\nu = 1$ and N additional channels which couple to it. In additions to that they assumed the couplings to the bound-state V^{coup} are similar for each channel and neglected the cross-channel couplings. From Eq.2.12, one can observe that the waves in the N excited channels are equivalent to one another. Thus, the $(N + 1)$ coupled equations can be replaced by

$$\frac{d^2\chi_1}{dr^2} + \frac{2\mu}{\hbar^2} [E - V^{eff}] \chi_1 = \frac{2\mu}{\hbar^2} \sqrt{N} V^{coup} \tilde{\chi} \quad (2.15)$$

$$\frac{d^2\tilde{\chi}}{dr^2} + \frac{2\mu}{\hbar^2} [E - V^{eff}] \tilde{\chi} = \frac{2\mu}{\hbar^2} \sqrt{N} V^{coup} \chi_1 \quad (2.16)$$

These equations can be solved by introducing

$$\chi_1 = \frac{1}{2} [\chi_+ + \chi_-]$$

$$\tilde{\chi} = \frac{1}{2} [\chi_+ - \chi_-]$$

$$\frac{d^2\chi_\pm}{dr^2} + \frac{2\mu}{\hbar^2} [E - (V_\pm^{eff} \pm \sqrt{N} V^{coup})] \chi_\pm = 0 \quad (2.17)$$

Then, the total transmitted flux is

$$T = T_1 + \tilde{T} = \frac{1}{2} [T_+ + T_-]$$

where T_\pm is the flux transmitted by the potential $V^{eff} \pm \sqrt{N} V^{coup}$.

In the classical limit the coefficients T_\pm are step functions changing from zero to one at energies equal to the barrier heights $V_B \pm \sqrt{N} V_B^{coup}$. When the coupling

is included

$$T = \begin{cases} 1, & E > V_B^{eff} + \sqrt{N}V_B^{coup} \\ \frac{1}{2}, & V_B^{eff} - \sqrt{N}V_B^{coup} < E < V_B^{eff} + \sqrt{N}V_B^{coup} \\ 0, & E < V_B^{eff} - \sqrt{N}V_B^{coup} \end{cases} \quad (2.18)$$

The coupling between different channels lead to the modification of the potential barrier. When the coupling between channels is taken into account, the step function is smoothed due to quantum mechanical effects. The coupling spreads the energy range over which T varies from zero to one by the amount $2\sqrt{N}V_B^{coup}$ with respect to the limit of no coupling. The coupling to the intrinsic degrees of freedom cause the potential energy landscape to become multidimensional, with multiple minima and maxima. The total transmission is the sum of the transmission coefficients of each barrier. Tunneling through the multi-dimensional barrier explains the sub-barrier enhancement in fusion cross sections.

2.3 Coupled-Channel code CCFULL

As stated in the previous section, the influence of nuclear structure on heavy ion fusion reactions is studied in the coupled-channel approach. To study the sub-barrier fusion, simplified coupled-channel codes such as CCFUS [10], CCDEF [11, 12] and CCMOD [13] or realistic coupled-channel code CCFULL [14, 15] have been used. The parent codes of CCMOD, CCFUS and CCDEF, calculate the cross sections using the Wong's formula [4]. Wong's formula does not take ℓ dependence of the barrier curvature or radius into account. CCMOD use the modified Wong's formula by replacing the barrier radius R_B as

$$R_E = R_B - a \ln \left[1 + 2 \frac{(E - V_B)}{V_B} \right] \quad (2.19)$$

CCFULL is a coupled-channel code, which calculates fusion cross sections and the mean angular momenta of the CN under the influence of couplings between the relative motion and nuclear collective motions [16]. CCFULL directly inte-

grates coupled second-order differential equations using the modified Numerov method. The coupled-channel equations are solved by imposing the incoming wave boundary condition (IWBC) and a barrier penetrability is calculated for each partial wave. The program CCFULL includes the couplings to full order and thus it does not introduce the expansion of the coupling potential. For heavy ion reactions, to reduce the dimension of the coupled-channel equations with full space, one can replace the angular momentum of the relative motion in each channel with the total angular momentum (J), which is called no-Coriolis approximation/iso-centrifugal approximation. The program CCFULL employs the no-Coriolis approximation. Then the coupled-channel equations are given by

$$\left[-\frac{\hbar^2}{2\mu} \frac{d^2}{dr^2} + \frac{J(J+1)\hbar^2}{2\mu r^2} + V_N^{(0)}(r) + \frac{Z_P Z_T e^2}{r} + \epsilon_\nu + E \right] \psi_\nu(r) + \sum_m V_{\nu m}(r) \phi_m(r) = 0 \quad (2.20)$$

where ϵ_ν is the excitation energy of the given channel ν . $V_{\nu m}$ are the matrix elements of the coupling Hamiltonian, which in the collective model consist of Coulomb and nuclear components. $V_N^{(0)}$ is the nuclear potential in the entrance channel. In the program, the Woods-Saxon parametrization is used for nuclear potential.

As already mentioned, CC equations are solved by IWBC. The boundary conditions are

$$\phi_\nu(r) \longrightarrow T_\nu \exp\left(-i \int_{r_{min}}^r k_\nu(r') dr'\right), \quad r \leq r_{min} \quad (2.21)$$

$$\phi_\nu(r) \longrightarrow H_J^{(-)}(k_\nu r) \delta_{\nu,0} + R_\nu H_J^{(+)}(k_\nu r), \quad r > r_{max} \quad (2.22)$$

where $k_\nu(r)$ is the local wave number for the channel ν

$$k_\nu(r) = \sqrt{\frac{2\mu}{\hbar^2} \left(E - \epsilon_\nu - \frac{J(J+1)\hbar^2}{2\mu r^2} - V_N(r) - \frac{Z_P Z_T e^2}{r} - N_{\nu\nu}(r) \right)} \quad (2.23)$$

$H_J^{(-)}$ and $H_J^{(+)}$ are the incoming and the outgoing Coulomb functions, respectively. The solution of the coupled-channel equations with these boundary conditions is

given by

$$\phi_m(r) = \sum_{\nu} T_{\nu} \chi_{\nu m}(r) \quad (2.24)$$

$\chi_{\nu m}(r)$ is the wave function of the m^{th} channel. At $r = r_{max}$, $\chi_{\nu m}$ can be expressed by a superposition of the incoming and outgoing Coulomb waves as

$$\chi_{\nu m}(r) = C_{\nu m} H_J^{(-)}(k_m r) + D_{\nu m} H_J^{(+)}(k_m r) \quad r \rightarrow r_{max} \quad (2.25)$$

The coefficients $C_{\nu m}$ and $D_{\nu m}$ are

$$C_{\nu m} = \frac{H_{Jm}^{(+)(i-1)} \chi_{\nu m}^{(i+1)} - H_{Jm}^{(+)(i+1)} \chi_{\nu m}^{(i-1)}}{H_{Jm}^{(+)(i-1)} H_{Jm}^{(-)(i+1)} - H_{Jm}^{(+)(i+1)} H_{Jm}^{(-)(i-1)}} \quad (2.26)$$

and

$$D_{\nu m} = \frac{H_{Jm}^{(-)(i-1)} \chi_{\nu m}^{(i+1)} - H_{Jm}^{(-)(i+1)} \chi_{\nu m}^{(i-1)}}{H_{Jm}^{(-)(i-1)} H_{Jm}^{(+)(i+1)} - H_{Jm}^{(-)(i+1)} H_{Jm}^{(+)(i-1)}} \quad (2.27)$$

The transmission coefficients and inclusive penetrability are given by

$$T_{\nu} = (C^{-1})_{\nu 0} \quad (2.28)$$

$$P_J(E) = \sum_{\nu} \frac{k_{\nu}(r_{min})}{k_0} |T_{\nu}|^2 \quad (2.29)$$

The fusion cross section and the mean angular momentum of compound nucleus are

$$\sigma_{fus}(E) = \sum_J \sigma_J(E) = \frac{\pi}{k_0^2} \sum_J (2J+1) P_J(E) \quad (2.30)$$

$$\langle l \rangle = \sum_J J \sigma_J(E) / \sum_J \sigma_J(E) \quad (2.31)$$

respectively.

2.3.1 Coupling matrix elements

If we consider a rotational nucleus as a target, having quadrupole and hexadecapole deformations, the nuclear coupling Hamiltonian can be obtained by changing the target radius in the nuclear potential to a dynamical operator

$$R_0 \rightarrow R_0 + \hat{O} = R_0 + \beta_2 R_T Y_{20} + \beta_4 R_T Y_{40} \quad (2.32)$$

where R_T is parametrized as $r_{coup} A_T^{1/3}$, and β_2 and β_4 are the quadrupole and hexadecapole deformation parameters of the deformed target nucleus, respectively. The nuclear coupling Hamiltonian is thus given by

$$V_N(r, \hat{O}) = \frac{-V_0}{1 + \exp((r - R_0 - \hat{O})/a)} \quad (2.33)$$

The matrix elements of the coupling Hamiltonian between the $|\nu\rangle = |I0\rangle$ and $|m\rangle = |I'0\rangle$ states of the rotational band of the target can be obtained by diagonalizing the matrix \hat{O} , whose elements are given by

$$\begin{aligned} \hat{O}_{II'} &= \sqrt{\frac{5(2I+1)(2I'+1)}{4\pi}} \beta_2 R_T \begin{pmatrix} I & 2 & I' \\ 0 & 0 & 0 \end{pmatrix}^2 \\ &+ \sqrt{\frac{9(2I+1)(2I'+1)}{4\pi}} \beta_4 R_T \begin{pmatrix} I & 4 & I' \\ 0 & 0 & 0 \end{pmatrix}^2 \end{aligned} \quad (2.34)$$

Then the nuclear coupling matrix elements are

$$V_{\nu m}^{(N)} = \sum_{\alpha} \langle I0|\alpha\rangle \langle \alpha|I'0\rangle V_N(r, \lambda_{\alpha}) - V_N^{(0)}(r) \delta_{\nu, m} \quad (2.35)$$

Hagino *et al.* [17] found that the second order coupling in the Coulomb interaction causes no visible effects to the fusion cross sections. Therefore, CCFULL use the linear coupling approximation for the Coulomb coupling. The matrix elements

of the Coulomb coupling form factor are then given by

$$V_{\nu m}^{(C)} = \frac{3Z_P Z_T R_T^2}{5 r^3} \sqrt{\frac{5(2I+1)(2I'+1)}{4\pi}} \left(\beta_2 + \frac{2}{7} \sqrt{\frac{5}{\pi}} \beta_2^2 \right) \begin{pmatrix} I & 2 & I' \\ 0 & 0 & 0 \end{pmatrix}^2 \\ + \frac{3Z_P Z_T R_T^4}{9 r^5} \sqrt{\frac{9(2I+1)(2I'+1)}{4\pi}} \left(\beta_4 + \frac{9}{7} \beta_2^2 \right) \begin{pmatrix} I & 4 & I' \\ 0 & 0 & 0 \end{pmatrix}^2$$

The total coupling matrix element is given by the sum of $V_{\nu m}^{(N)}$ and $V_{\nu m}^{(C)}$.

In the case of a vibrational nuclei, the operator \hat{O} in the nuclear coupling Hamiltonian is given by

$$\hat{O} = \frac{\beta_\lambda}{\sqrt{4\pi}} R_T (a_{\lambda 0}^\dagger + a_{\lambda 0}) \quad (2.36)$$

where λ is the multi-polarity of the vibrational mode, $a_{\lambda 0}^\dagger$ is the creation operator and $a_{\lambda 0}$ is the annihilation operator of the phonon. The matrix element of this operator between the phonon state $|\nu\rangle$ and the phonon state $|m\rangle$ is given by

$$\hat{O}_{\nu m} = \frac{\beta_\lambda}{\sqrt{4\pi}} R_T (\sqrt{m} \delta_{\nu, m-1} + \sqrt{\nu} \delta_{\nu, m+1}) \quad (2.37)$$

The nuclear coupling matrix elements are calculated according to Eq. 2.35.

The Coulomb coupling matrix elements of the vibrational degrees of freedom are

$$V_{\nu m}^{(C)}(r) = \frac{\beta_\lambda}{\sqrt{4\pi}} \frac{3}{2\lambda + 1} Z_P Z_T e^2 \frac{R_T^\lambda}{r^{\lambda+1}} (\sqrt{m} \delta_{\nu, m-1} + \sqrt{\nu} \delta_{\nu, m+1}) \quad (2.38)$$

Transfer reactions with positive Q-values would lead to an increase in the transmission, as a consequence, enhancement in the sub-barrier fusion cross sections compared to 1D-BPM predictions. Beckerman *et al.* [18] observed the influence of couplings to transfer channels on $^{58}\text{Ni} + ^{64}\text{Ni}$ fusion cross sections for the first time. The coupling to pair transfer channels with positive Q values has the largest influence on the sub-barrier fusion cross sections, whereas the coupling to single-nucleon transfer channels has a smaller impact. Because the form factors for single-nucleon transfer, $F_{1N}(r) \propto \exp(-r/a)$, are long ranged, whereas the

pair-transfer form factor, $F_{2N}(r) \propto \exp(-2r/a)$, which is short range and proportional to the square of single-nucleon transfer form factors [5].

The program CCFULL have an option to include a pair-transfer coupling between the ground states. It uses the macroscopic coupling form factor given by Dasso *et al.* [19, 20],

$$F_{trans}(r) = F_t \frac{dV_N^{(0)}}{dr} \quad (2.39)$$

where F_t is the coupling strength.

2.4 Statistical model

In fusion processes a projectile and target fuse together and equilibrate in all degrees of freedom and form a composite system called the compound nucleus (CN). The decay of excited CN is completely independent of its entrance channel [21]. Statistical model assumes that possible decay channels are equally likely to be populated. The description of a nuclear reaction in terms of the decay of an equilibrium system in which phase relations can be neglected is called the ‘Statistical Model’. A quantitative formulation of the statistical model was first proposed by Weisskopf [22]. The statistical model is one of the most successful models to understand fusion-fission or fusion-evaporation reactions. The de-excitation or cooling of the CN, including competition from the fission process, explained by statistical evaporation calculations [23].

The probability per unit time for the CN at excitation energy E^* to emit particle n into a energy interval between ϵ and $\epsilon+d\epsilon$ is [24, 25]

$$P(\epsilon, E^*)d\epsilon = \frac{(2S_n + 1)M_n \epsilon \sigma_n(\epsilon, U) \rho_n(U) d\epsilon}{\pi^2 \hbar^3 \rho_C(E^*)} \quad (2.40)$$

where M_n , and S_n , are the mass and spin of particle n . The level density of the CN at excitation energy E^* is $\rho_C(E^*)$, the level density of the residual nucleus at excitation energy U is $\rho_n(U)$ and $\sigma_n(\epsilon, U)$ is the inverse reaction cross

sections. The inverse reaction cross sections are the cross sections for the formation of the CN when particle n is incident upon the excited residual nucleus. The difference between the total reaction cross sections and the cross sections for CN formation is usually ignored (direct-interaction contribution is small), so $\sigma_n(\epsilon, U) = \sigma_n(\epsilon)$ [24].

The relative yields of different particles and the emission spectrum of any particular particle can be described by,

$$N_n(\epsilon) = C(2S_n + 1)M_n\epsilon\sigma_n(\epsilon)\rho_n(U) \quad (2.41)$$

where $N_n(\epsilon)$ is the number of particles of type n emitted per unit energy interval, and C is a constant which is the same for all emitted particles and emission energies. Eq. 2.41 is often called an evaporation equation [24]. In Eq. 2.40 and 2.41 the level density and the reaction cross sections do not have dependence on angular momentum. Angular-momentum dependence on compound nuclear decay has been discussed by Wolfenstein [26], Hauser and Feshbach [27], Ericson and Strutinski [28] and Douglas and MacDonald [29].

The formation of CN and its decay of the various intermediate states are uncorrelated. The cross section for the formation of a particular product is given by [30],

$$\sigma = \frac{\pi\lambda^2}{(2I_1 + 1)(2I_2 + 1)} \sum_{S_1=|I_1-I_2|}^{|I_1+I_2|} \sum_{l_1=0}^{\infty} T_{l_1} \sum_{J=|l_1-S_1|}^{|l_1+S_1|} \frac{\Gamma_J^b}{\Gamma_J^T} (2J + 1) \quad (2.42)$$

where Γ_J^b is the width for decay to the product of interest and Γ_J^T is the total width. In case of the medium-mass nuclei at excitations well above the neutron-binding energy, neutron emission is the dominant decay process and its probability is slightly affected by angular momentum, in this case Γ_J^b/Γ_J^T does not depend strongly on the spin of the CN [30]. The symbols I_1 and I_2 represent the spins of target nucleus and projectile respectively and S_1 is the channel spin $S_1 = |I_1 + I_2|$. The spin of the compound nucleus $J = |l_1 + S_1|$.

As discussed, the CN loses its memory of the entrance channel and leads to decay, which is governed by phase space. A dominating part of the phase space in a nuclear reaction is the density of levels in the residual nucleus. The nuclear level densities increase with excitation energy. When the excitation energy is increased, the spacing between the levels is considerably decreased compared to near the ground state. The level density has an exponential increase with excitation energy. Most considerations of the nuclear level density at elevated energies have been based on Fermi gas models. The nuclear level density as a function of excitation energy E^* and angular momentum J can be written as [30],

$$\rho(E^*, J) = (2J + 1) \exp \left[\frac{-(J + \frac{1}{2})^2}{(2\sigma^2)} \right] \rho(E^*) \quad (2.43)$$

The quantity $\rho(E^*)$ depends only on excitation energy and is approximately equal to the density of states with $J=0$. σ^2 is the spin-cutoff parameter, which may depend on excitation energy and angular momentum.

2.5 Statistical model code: HIVAP

The de-excitation of the formed compound nuclei is described in the framework of the statistical model. Several computer codes CASCADE [31], PACE4 [32], HIVAP [33, 34], etc are successful in modeling the statistical decay. The code PACE4 uses Monte Carlo procedure to determine the decay sequence of an excited nucleus. In PACE4, the transmission coefficients (T_ℓ) for light particle emission are obtained by an optical model calculation and in subsequent stages of de-excitation which are obtained by extrapolation. Also, a fission decay mode added using a rotating liquid drop fission barrier routine. At each stage of de-excitation PACE4 calculate angular momentum projection, this enables the determination of the angular distribution of the emitted particles. For efficiency calculations, the dominant ER channels were simulated using PACE4 for $^{12}\text{C} + ^{182,184,186}\text{W}$ reactions, at all measured energies.

The statistical model code CASCADE calculate T_ℓ exactly for every de-

excitations. The inclusion of friction in the fission motion results in a modification of the normal Bohr-Wheeler expression [35], this modifications to the fission decay width has been incorporated into the CASCADE statistical model code.

HIVAP (Heavy Ion VAPorisation statistical-evaporation model) is a statistical model code used to calculate cross sections from heavy ion fusion reactions [33, 34, 36]. The HIVAP code includes the statistical de-excitation of the excited compound nucleus through neutron, γ -ray, and charged particle emission as well as fission. The HIVAP code makes use of conventional statistical decay theory, which considers ER production processes as two-step processes, i.e., 1) compound nucleus formation and 2) it's entirely independent of subsequent de-excitation by nuclear fission and/or emission of light particles and γ rays. Further, HIVAP code incorporates new insights into level density calculations, interaction barriers, ground-state masses and shell-effects, and fission barriers. In HIVAP code, fusion mechanism is assumed to occur whenever the projectile-target system overcomes the interaction potential barrier calculated from Bass's global nucleus-nucleus potential [37]. To estimate the cross sections at the sub-barrier region, the WKB (Wentzel-Kramer-Brillouin) approximation is used to evaluate the transmission coefficients. Coupled-channel effects are taken into account phenomenologically through the use of fluctuating barrier [34, 38], which may be necessary at near and sub-barrier energies. To phenomenologically parameterize this barrier distribution, a Gaussian distribution cut-off at both ends after five standard deviations has been employed.

Level density parameters, fission barriers, and masses are the main sensitive parameters used in the second de-excitation stage. Both the fission barriers and the nuclear level density are influenced by the ground-state shell effects, which are calculated by subtracting the empirical [39] and liquid drop masses [40]. According to Reisdorf's macroscopic description, the nuclear level densities in fission and evaporation channels are provided by ratios of level densities $a_f/a_n \geq 1$, due to the different nuclear shapes at the saddle point (fission) and equilibrium state

(light-particle and γ -emission) [33, 34]. The influence of shell effects is included by an energy backshift in the level density parameter a . Shell effects is washed out with increasing energy.

For the level density HIVAP uses,

$$\rho(E, J) = \frac{1}{24} \left(\frac{\hbar}{2\theta} \right)^{\frac{3}{2}} (2J + 1) a^{\frac{1}{2}} U_J^{-2} \exp \left[2(U_J)^{\frac{1}{2}} \right] \quad (2.44)$$

where $U_J = (E - E_r(J) + P)$ and θ is the moment of inertia. $E_r(J)$ is the yrast energy of either the equilibrium configuration or the saddle-point configuration.

$$E_r(J) = \frac{\hbar^2 J(J + 1)}{2\theta} \quad (2.45)$$

The pairing correction P was obtained from experimental odd-even mass fluctuations and the level density parameter a can be written as

$$a = \tilde{a} \left(1 + \left[1 - e^{-\frac{E}{E_d}} \right] \delta W_{g.s.} / E \right) \quad (2.46)$$

where \tilde{a} is the macroscopic value of a and the expression in brackets describes the fading influence of the ground-state shell correction energy $\delta W_{g.s.}$ on the level density, the damping constant E_d being 18 MeV.

At energies well above the fusion barrier, fission has a significant influence on the production cross sections of ERs. The HIVAP calculation is determined by the fission barrier scaling factor (k_f) of the liquid drop (LD) fission barrier (B_f^{LD}) [41], which modify the fission barrier as

$$B_f(l) = k_f B_f^{LD} + \delta W_{g.s.} \quad (2.47)$$

The Reisdorf and Schädel parameters [34] are the standard set of parameters used for this calculation in HIVAP code, which is listed in Table 2.1. Using the Reisdorf and Schädel parameters, the results of HIVAP calculations agree well

Table 2.1: Reisdorf and Schädel Parameter set [34], used for the statistical model calculations.

Variable	Description	Value
LEVELPAR	Scale parameter for the level density	1.153
AF / AN	Level density ratio parameter value	1
BARFAC	Scale parameter for the fission barrier	1
EDAMP	Shell effect damping energy (MeV)	18.0
DELTA	Nuclear pairing correction energy (MeV)	11.0
V0	Initial value of the nuclear potential (MeV)	70.0
R0	Nuclear radius parameter (fm)	1.12
D	Fuzziness in the nuclear radius parameter (fm)	0.75
Q2	Nuclear quadrupole moment (fm ²)	1050
CRED	Scale parameter for the interaction barrier	1.0
SIGR0	Fluctuation of the interaction barrier (% of R0)	3.0
SIGR0	Integration limits in (SIGR0) for barrier fluctuations	5.0
XPUSH	Extra push theory threshold fissility parameter	0.7
APUSH	Slope coefficient from extra push theory	18.0
FPUSH	Angular momentum coefficient from extra push theory	0.75

with the measured ER cross sections for hot fusion reactions [34]. These set of parameters phenomenologically reproduces many of the experimental super heavy element production cross sections obtained with actinide targets [34]. Patin [42] altered the Reisdorf and Schädel input parameters for HIVAP to model the experimental results of cold fusion reactions more accurately. This parameters set were called the Patin parameters. Modifications to the standard input parameters of the HIVAP code explained the fusion cross sections for other reactions [38, 42].

Bibliography

- [1] M. Dasgupta, D. J. Hinde, N. Rowley, and A. M. Stefanini, *Annu. Rev. Nucl. Part. Sci* **48**, 401 (1998).
- [2] L. C. Vaz, J. M. Alexander, and G. Satchler, *Physics Reports* **69**, 373 (1981).
- [3] D. L. Hill and J. A. Wheeler, *Phys. Rev.* **89**, 1102 (1953).
- [4] C. Y. Wong, *Phys. Rev. Lett.* **31**, 766 (1973).
- [5] B. B. Back, H. Esbensen, C. L. Jiang, and K. E. Rehm, *Rev. Mod. Phys.* **86**, 317 (2014).
- [6] R. Broglia, C. H. Dasso, S. Landowne, and G. Pollaro, *Phys. Lett. B* **133**, 34 (1983).
- [7] C. H. Dasso, S. Landowne, and A. Winther, *Nucl. Phys. A* **407**, 221 (1983).
- [8] C. H. Dasso, S. Landowne, and A. Winther, *Nucl. Phys. A* **405**, 381 (1983).
- [9] C. H. Dasso, S. Landowne, and A. Winther, *Nucl. Phys. A* **432**, 495 (1985).
- [10] C. H. Dasso and S. Landowne, *Comput. Phys. Commun.* **46**, 187 (1987).
- [11] M. Dasgupta, A. Navin, Y. K. Agarwal, C. V. K. Baba, H. C. Jain, M. L. Jhingan, and A. Roy, *Nucl. Phys. A* **539**, 351 (1992).
- [12] J. Fernandez-Niello, C. H. Dasso, and S. Landowne, *Comput. Phys. Commun.* **54**, 409 (1989).
- [13] J. O. Newton, R. D. Butt, M. Dasgupta, D. J. Hinde, I. I. Gontchar, C. R. Morton, and K. Hagino, *Phys. Rev. C* **70**, 024605 (2004).
- [14] K. Hagino, N. Rowley, and A. T. Kruppa, *Comput. Phys. Commun.* **123**, 143 (1999).

- [15] K. Hagino and N. Takigawa, *Prog. Theor. Phys* **128**, 1061 (2012).
- [16] K. Hagino, *Sub-barrier fusion reactions* (2022), 2201.08061.
- [17] K. Hagino, N. Takigawa, M. Dasgupta, D. J. Hinde, and J. R. Leigh, *Phys. Rev. C* **55**, 276 (1997).
- [18] J. A. Becker, N. Roy, E. A. Henry, M. A. Deleplanque, C. W. Beausang, R. M. Diamond, J. E. Draper, F. S. Stephens, J. A. Cizewski, and M. J. Brinkman, *Phys. Rev. C* **41**, R9 (1990).
- [19] C. H. Dasso and A. Vitturi, *Phys. Lett. B* **179**, 337 (1986).
- [20] C. H. Dasso and G. Pollarolo, *Phys. Lett. B* **155**, 223 (1985).
- [21] N. Bohr, *Nature* **137**, 344 (1936).
- [22] V. F. Weisskopf and D. H. Ewing, *Phys. Rev.* **57**, 472 (1940).
- [23] P. Paul and M. Thoennessen, *Annu. Rev. Nucl. Part. Sci.* **44**, 65 (1994).
- [24] D. Bodansky, *Annu. Rev. Nucl. Sci* **12**, 79 (1962).
- [25] T. Ericson, *Advances in Physics* **9**, 425 (1960).
- [26] L. Wolfenstein, *Phys. Rev.* **82**, 690 (1951).
- [27] W. Hauser and H. Feshbach, *Phys. Rev.* **87**, 366 (1952).
- [28] T. Ericson and V. Strutinski, *Nucl. Phys. A* **8**, 284 (1958).
- [29] A. Douglas and N. MacDonald, *Nucl. Phys. A* **13**, 382 (1959).
- [30] T. D. Thomas, *Annu. Rev. Nucl. Sci* **18**, 343 (1968).
- [31] F. Phlhofer, *Nucl. Phys. A* **280**, 267 (1977).
- [32] A. Gavron, *Phys. Rev. C* **21**, 230 (1980).

- [33] W. Reisdorf, Z. Phys. A **300**, 227 (1981).
- [34] W. Reisdorf and M. Schädel, Z. Phys. A Hadrons Nucl. **343**, 47 (1992).
- [35] N. Bohr and J. A. Wheeler, Phys. Rev. **56**, 426 (1939).
- [36] D. Vermeulen, H.-G. Clerc, C.-C. Sahn, K.-H. Schmidt, J. G. Keller, G. Münzenberg, and W. Reisdorf, Z. Phys. A **318**, 157 (1984).
- [37] R. Bass, Phys. Rev. Lett. **39**, 265 (1977).
- [38] H. M. Devaraja, Y. K. Gambhir, M. Gupta, and G. Münzenberg, Phys. Rev. C **93**, 034621 (2016).
- [39] G. Audi and A. H. Wapstra, Nucl. Phys. A **595**, 409 (1995).
- [40] W. D. Myers and W. J. Swiatecki, Ark. Fys. **36**, 343 (1967).
- [41] S. Cohen, F. Plasil, and W. Swiatecki, Annals of Physics **82**, 557 (1974).
- [42] J. B. Patin, Experimental Cross Sections for Reactions of Heavy Ions and ^{208}Pb , ^{209}Bi , ^{238}U , and ^{248}Cm Targets, Ph.D. thesis, Brookhaven (2002).

Chapter 3

Experimental Details

3.1 Introduction

In this chapter, we describe the accelerator facility, the experimental setup, detectors, electronics, measurements, and other experimental facilities used in the current work. In the present study, we have measured the ER cross sections for $^{12}\text{C}+^{182,184,186}\text{W}$ reactions forming the $^{194,196,198}\text{Hg}$ compound nuclei. The measurements were carried out using ^{12}C beams provided by 15 UD tandem accelerator at Inter-University Accelerator Centre (IUAC), New Delhi. An energetic primary ^{12}C beams is bombarded on thin isotopically enriched $^{182,184,186}\text{W}$ targets. To separate the ERs from the unwanted reaction products and unreacted primary beams we use a recoil separator, Heavy Ion Reaction Analyzer (HIRA). HIRA separate ERs from the beam background and transferred them to its focal plane (FP). A two-dimensional position-sensitive multi-wire proportional counter detector (MWPC) was used to detect ERs at the HIRA's focal plane.

3.2 15 UD tandem accelerator

The 15 UD Pelletron accelerator at IUAC [1, 2], is an electrostatic tandem accelerator. A tandem accelerator is a combination of two Van de Graff accelerators.

The Pelletron accelerator column is installed in a vertical configuration in an insulating tank of length 26.5 m and diameter 5.5 m, filled with SF₆ insulating gas. It is capable of accelerating ion beams of all stable nuclei, from proton to uranium, except inert gases, up to an energy of about 200 MeV depending upon the ions. A high-voltage terminal is situated at the center of the vertical accelerating tank. It can be charged to a high potential that can be varied from 4 to 15 MV. The portion above the terminal is called the low energy section and the portion below the terminal is called the high energy section. Resistor based voltage grading system is used to maintain a potential gradient from the top of the tank to the terminal, and subsequently from the terminal to the bottom. Earlier the accelerator had corona based voltage grading system to define the potential [3]. Use of shorting rods and change of insulating gas pressure are the only options in a corona-based system to generate large changes in terminal potential. With the use of this resistor-based voltage gradient system, voltage stability of the accelerator has improved and no shorting rods are used now for generating variations in terminal voltages. The terminal has thirty modules, 15 on each side. Each module can hold a potential difference of ~ 1 MV. The schematic diagram of the accelerator is shown in Fig. 3.1.

There is an ion source, Multi Cathode Source of Negative Ions by Cesium Sputtering (MC-SNICS) [4], at the top of the pelletron for the production of negative ions. Earlier, NEC made single sample SNICS ion source (Source of Negative Ion by Cesium Sputtering) was used for the production of negative ions, but at present, it is being operated with MC-SNICS to produce beams with higher currents and to deliver beams without a delay to the users [4]. The negative ions emerging from the ion source are pre-accelerated up to ~ 300 keV in Ion Source. The pre-accelerated ions are focused and are mass analyzed using the 90° bending injector magnet. After focusing and mass selection using a 90° bending injector magnet, injecting them into the low energy accelerating section and gain energy

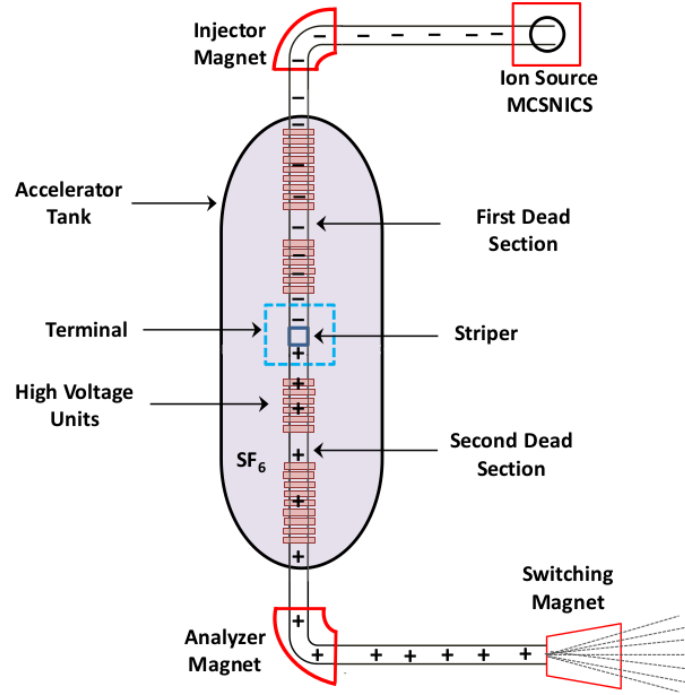


Figure 3.1: Schematic representation of 15 UD Pelletron accelerator at IUAC, New Delhi.

(in MeV).

$$E_{int} = (E_0 + V) \quad (3.1)$$

where E_0 is the energy of the ion gained in pre-acceleration and V is the terminal potential in MV. The injected ions are driven down towards the high voltage terminal in the center due to the high voltage terminal. The accelerated negative ions pass through a stripper at the terminal. The stripper can be a very thin carbon foil or a small volume of gas. When the negatively charged ions pass through the stripper, they lose electrons, and consequently, the positive ions will be in different charge states. The charge state distribution of these ions depends upon the energy of the ions being accelerated. These positive ions are repelled by the positive terminal and they move from the terminal to the bottom of the tank due to the negative potential gradient. The ions with a particular charge state are selected using a 90° bending dipole magnet called an analyzer magnet.

Energy gained by the ions after emerging out of the tank is given by

$$E_{final} = [E_0 + V(1 + q)] \quad (3.2)$$

In the high energy dead section, there is a second stripper assembly. This will aid further stripping and result in a greater charge state and thus more energy. When both strippers are used during acceleration, final energy is given by,

$$E_{final} = E_0 + V(1 + (0.4 * q_1) + (0.6 * q_2)) \quad (3.3)$$

where q_1 and q_2 are the ion charge states. After departing the tank, the ions are bent 90° by the analyzer magnet. Also, this magnet helps in the selection of ion energy. Using the switcher magnet, these beams are then switched to the pre-selected beamline among the many beamlines (experimental area). The entire machine is controlled by a computer and operated from the control room. IUAC pelletron accelerator can provide both DC and pulsed beams, depending on the experimental requirements. The pulsing system's components are based on the principles of ion velocity modulation and electrostatic or magneto-static deflection. A chopper, a buncher, and a Traveling Wave Deflector (TWD) make up the pulsing system. These components are installed in the pre-acceleration stage, between the injector magnet and the tank top. The chopper uses a pair of plates in which a radio frequency field is applied to cut off the beam at regular intervals. TWD determines the repetition rate of the beam pulses by selecting and eliminating these pulses at regular intervals, and the buncher bunches these chopped beam pulses by compressing them in time. The effective current intensity of the beam is reduced as a result of this deviation.

3.3 Heavy Ion Reaction Analyzer (HIRA)

A Recoil Mass Spectrometer (RMS) or recoil separator is an instrument used for beam rejection and mass analysis of the reaction products in a nuclear re-

action [5]. Placed at zero degrees with respect to the beam, RMS's are capable of separating and rejecting the beam-like particles from nuclear reaction products and dispersing heavy residues of fusion reactions according to m/q (mass to charge) along the focal plane. It is working under the principle of dispersion of ions in electric and magnetic fields. An ideal recoil separator should have a large solid angle of acceptance, large mass dispersion, good mass resolution, no energy dispersion at the final point, large energy and mass acceptances, and large transmission efficiency.

Heavy Ion Reaction Analyzer (HIRA) [6] is a recoil mass spectrometer. The electromagnetic configuration selected for HIRA is QQ-ED-M-MD-ED-QQ, a schematic diagram of HIRA is shown in Fig. 3.2 and a photograph of the HIRA is shown in Fig. 3.3, where Q stands for the quadrupole doublet, ED for the electrostatic dipoles, MD for the magnetic dipole, and M for the multipoles. The ion-optical parameters of ED-MD-ED combination of HIRA are unique and quite different from other existing recoil mass spectrometers. The HIRA has an energy acceptance of $\pm 20\%$, mass acceptance of $\pm 5\%$, acceptance of 1-10 *msr* (variable), mass dispersion of 0-10 *mm* % (variable) and mass resolution is 1/300 (typical).

In the case of heavy ion-induced complete fusion reactions, HIRA rejects primary beam particles and transfer reaction products, and it transports the ERs to the FP and disperses them as per mass to charge ratio (m/q) values. The overall length of HIRA from the target chamber to the focal plane chamber is ~ 8.8 *m*. One of the main features of the HIRA is the ability to rotate around a fixed axis. The entire spectrometer is installed on a platform that can rotate with the help of a motor about the vertical axis passing through the target and beam axis on a curved monorail. The HIRA can be rotated from angles -15° to $+40^\circ$ maintaining a very high vacuum.

HIRA is the first RMS with a feature that allows the primary beam to be removed without scattering from the anode of the first electrostatic dipole. To do this, a horizontal slot (of 15 *mm*) is cut out at the center of the second half of the anode

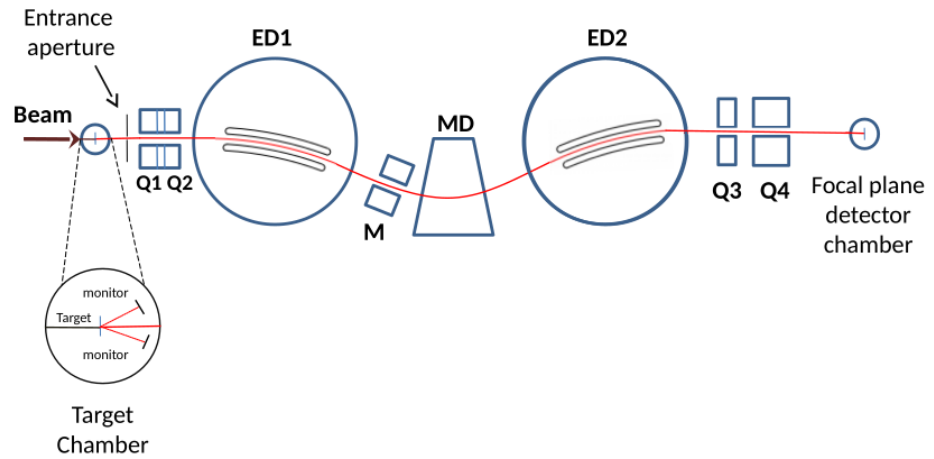


Figure 3.2: A schematic diagram of Heavy Ion Reaction Analyzer (HIRA). Q, ED, M, and MD stand for magnetic quadrupole, electrostatic dipole, magnetic multipole, and magnetic dipole, respectively.



Figure 3.3: A complete view of Heavy Ion Reaction Analyzer (HIRA) setup [7], where the beam enters from the right side, it goes to the focal plane, situated on the left.

plate in ED1. This slot permits scattered beam particles to be caught on a beam catcher behind ED1 and lowers the focal plane background. The electric dipole (ED) effectively rejects beams by taking advantage of the significantly differing electrical rigidities of the beam particles and reaction products. The electrostatic deflector consists of two coaxial cylindrical plates, one of them serves as an anode and the other as a cathode. If the energy of the positive ions entering the energy filter is too high, the radial electric field will not deflect them enough, and they will collide with the anode plate. When the energy is low, the ions are more deflected and collide with the cathode plate. When a particle enters the field, it experiences an electrostatic force,

$$qE = \frac{mv^2}{\rho} \quad (3.4)$$

or

$$E\rho = \frac{mv^2}{q} = \frac{2T}{q} \quad (3.5)$$

where E is the electric field between deflector plates, m is mass, v is velocity, q is charge state and T is the kinetic energy of the particle. The quantity $E\rho$ is called electric rigidity.

The magnetic dipole (MD) does the m/q (m =mass of products and q =charge state) selection. When the ions entering the perpendicular magnetic field of uniform flux density B , it will follow a circular path, with radius ρ .

$$qvB = \frac{mv^2}{\rho} \quad (3.6)$$

or

$$B\rho = \frac{mv}{q} = \frac{p}{q} \quad (3.7)$$

where $B\rho$ is the magnetic rigidity.

There is a multipole (M) between ED1 and MD. It helps to achieve energy achro-

maticity at the focus plane by reducing angle and energy-dependent aberrations. To reduce the mass-dependent 'focal plane tilt/curvature' aberration there is a superimposition of suitable sextupole and octupole fields on the quadrupole field of the exit quadrupole doublet.

Using the combination of electric dipole and magnetic dipole, the particles can be separated based on their m/q ratio and follows well-defined trajectories. The ions having different m values and the same m/q ratio will be focused at the same point at the detector plane. This is called m/q ambiguity. For example, if the isobaric nuclei (same mass number but different atomic numbers) have the same energy and same charge state will have identical trajectories. Such ions are therefore not separated by the spectrometer. It can be resolved by the Time Of Flight (TOF) method.

3.4 Detection system

HIRA separates ERs from high beam background and unwanted reaction products. Detection of the particle of our interest is very important in an experiment. Interaction of particles with matter can be used to detect and identify those particles. In the present experiment, ERs from complete fusion evaporations are the particles of interest to detect. Detectors that can provide both position and energy information can be used to identify these reaction products. For the current ER measurements, we have used two silicon surface barrier detectors (monitor detectors) in the target chamber and a multi-wire proportional counter (MWPC) is at the focal plane.

3.4.1 Silicon Surface Barrier Detector (SSBD)

For the present experiments two SSBD (monitors) were placed in the target chamber to measure the elastically scattered beam particles. These detectors, each with an active area of 50 mm^2 with a collimator diameter of 1 mm , were placed at $\pm 15^\circ$ relative to the beam axis for beam normalization and also for

beam monitoring.

3.5 Multi-Wire Proportional Counters

Multi-Wire Proportional Counters (MWPC) was invented by Georges Charpak in 1968 [8]. At very low gas pressure, MWPCs are highly suitable to detect heavy ionizing particles. The MWPC consists of thin parallel and equally spaced anode wires centered between two cathode planes. The separation between the plane of the anode wires and the cathode plane is usually a few millimeters. Depending on the intended mode of operation, the chamber is filled with a suitable mixture of gases. The MWPC provides us with high detection efficiency, fast rise time, gain, and also good position resolution.

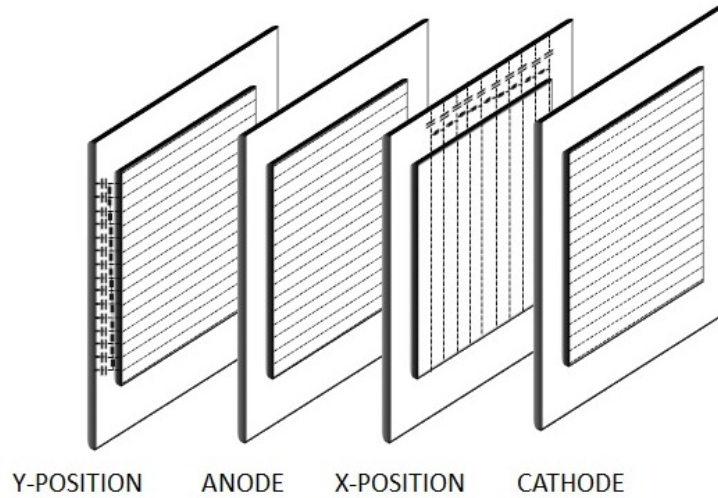


Figure 3.4: Schematics of the multi-wire proportional counter.

When the particle interacted with the gas medium, it gets ionized and the produced electrons will drift toward an anode wire. Secondary electrons are generated due to the inelastic collisions of these primary electrons with the gas molecules. Further inelastic collisions can cause an “electronic avalanche” or “charge multiplication”. The electron avalanche is rapidly collected by the anode wires and the positive ions move in the opposite direction toward the cathode.

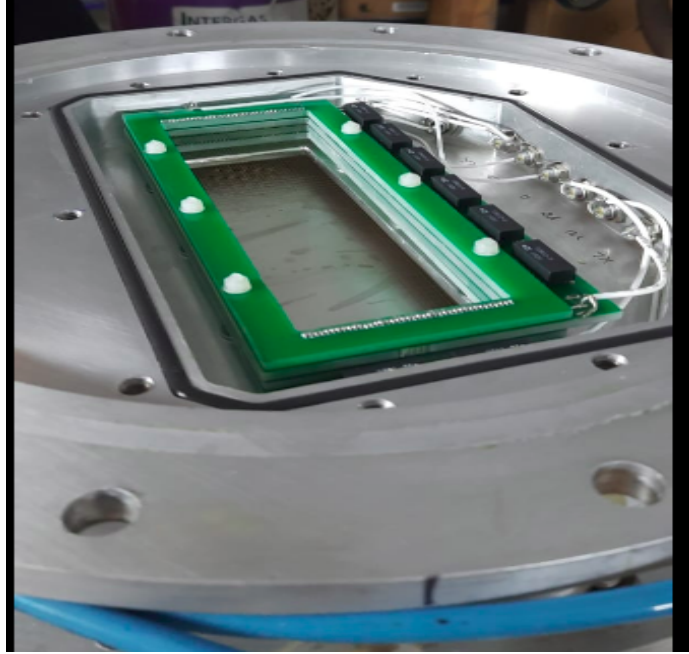


Figure 3.5: Photograph of the multi-wire proportional counter.

The MWPC is said to be “position sensitive” if it is possible to decode which of the wires the signal originated on. The operating parameters such as gas pressure, voltages on electrodes etc. can be adjusted to make it sensitive to heavier particles.

For the current measurements, a two-dimensional position-sensitive MWPC with an active area of $15\text{ cm} \times 5\text{ cm}$ was placed at the focal plane of the HIRA to detect the ERs [9]. The MWPC used in the present experiment has four electrode geometry, Cathode, X position electrode, anode, and Y position electrode. Fig. 3.4 shows a schematic of the detector geometry. Electrodes are wireframes, made up of gold-plated tungsten wires with an interwire spacing of 1.27 mm. X position frame has 120 wires and the Y position frame has 40 wires. The inter-electrode gap is 3.2 mm. A mylar foil of thickness $0.5\ \mu\text{m}$ was used as the entrance window of the MWPC, which separated the gas volume (2-3 mbar isobutane) of the MWPC from the vacuum inside the HIRA. The MWPC has a total of six output signals, cathode, anode, two X position signals X-left (XL) and X-right (XR) from both ends of the X position electrode and two Y position signals Y-up (YU) and Y-down (YD) from the two ends of Y position electrode. Photograph

of the MWPC used for the present measurements is shown in Fig. 3.5.

3.6 Electronic setup

The block diagram of the electronic setup used in the present experiment is shown in Fig. 3.6. The MWPC has total of six output signals, which are processed through a pre-amplifier before reaching the amplifier. Before applying the four position signals to a constant fraction discriminator (CFD), the signal needs a reasonable amplification. After pre-amplification, all four position signals are amplified through an 8-channel variable gate amplifier (VGA). The anode is the fastest signal, so it is taken as the timing start. The cathode signal gives the energy loss (ΔE) information instead of total energy. Both the signals, anode and cathode and four position signals are processed through CFD. The delayed CFD outputs, anode, and four positions signal are fed to time to digital converter (TDC). A delayed anode signal was used as a trigger for TDC. The Monitor detector signals (ML and MR) were processed through pre-amplifiers, and amplifiers and were given to the analog to digital converter (ADC). After the pre-amplification, the signal, ML, and MR, processed through IUAC's custom-made spectroscopic amplifier, which is not only shaped the signals but also provides the timing signals (NIM). These timing signals and MWPC anode were logical OR-ed using a logic fan-in and fan-out unit. Further, all the timing signals (anode and all the position signals) are fed to the gate and delay generator (GDG) and this signal was used as the master gate for the ADC. Also, cathode signals from CFD and ML and MR signals from the spectroscopic amplifier are fed to the ADC. For the TOF set-up, anode signal is taken as start and the signal from the traveling wave deflector (TWD) as the stop. The signal coming from the TWD is of the form TTL, it will convert into NIM signals and be fed to the time to amplitude converter (TAC). The TAC output was also fed to the ADC.

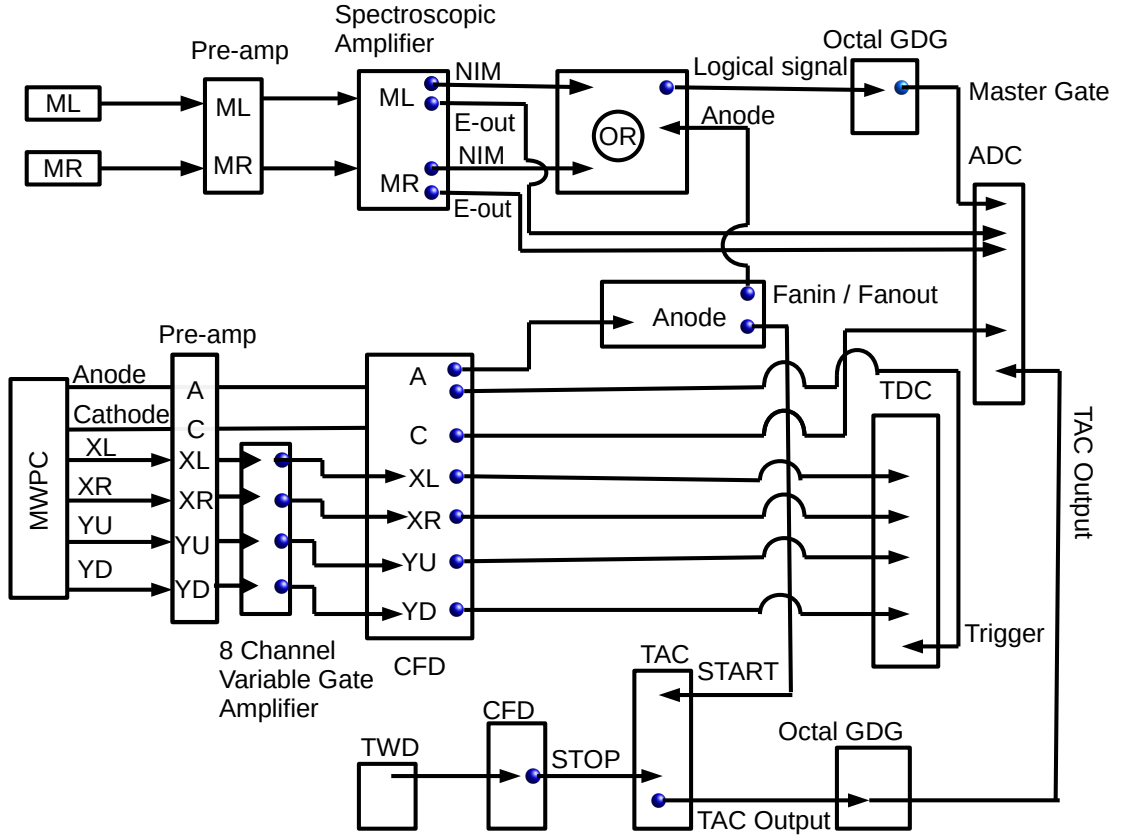


Figure 3.6: The schematic diagram of the electronics and data acquisition system used in the ER measurements.

3.7 Experimental Details

The measurements of $^{12}\text{C}+^{182,184,186}\text{W}$ performed using pulsed carbon beam with pulse separation $8 \mu\text{s}$ at 52-58 MeV, $4 \mu\text{s}$ at 60-72 MeV and 500 ns at 76-84 MeV. The targets used were $^{182,184,186}\text{W}$ with the thickness 70, 100 and $100 \mu\text{g}/\text{cm}^2$ on carbon backing 20, 35 and $25 \mu\text{g}/\text{cm}^2$ respectively. The enrichment for the $^{182,184,186}\text{W}$ targets were 91.6, 95.2 and 94.0 % respectively. The targets were mounted on a target ladder, which contains four slots, three for targets and one for quartz crystal. The targets were mounted on the target ladder in such a way that the carbon backing faces the beam first. The quartz crystal was used for viewing the beam spot using a CCD camera and TV monitor. The beam was first tuned on the quartz crystal mounted on the target ladder. After successful tuning of the beam on quartz, W targets were introduced in the beam

position for ER measurements. Two silicon surface barrier detectors (monitors) were placed in the target chamber, one on each side of the beam direction, to measure the elastically scattered beam particles for normalization and absolute cross section determination. Inside view of target chamber shown in Figure 3.7.

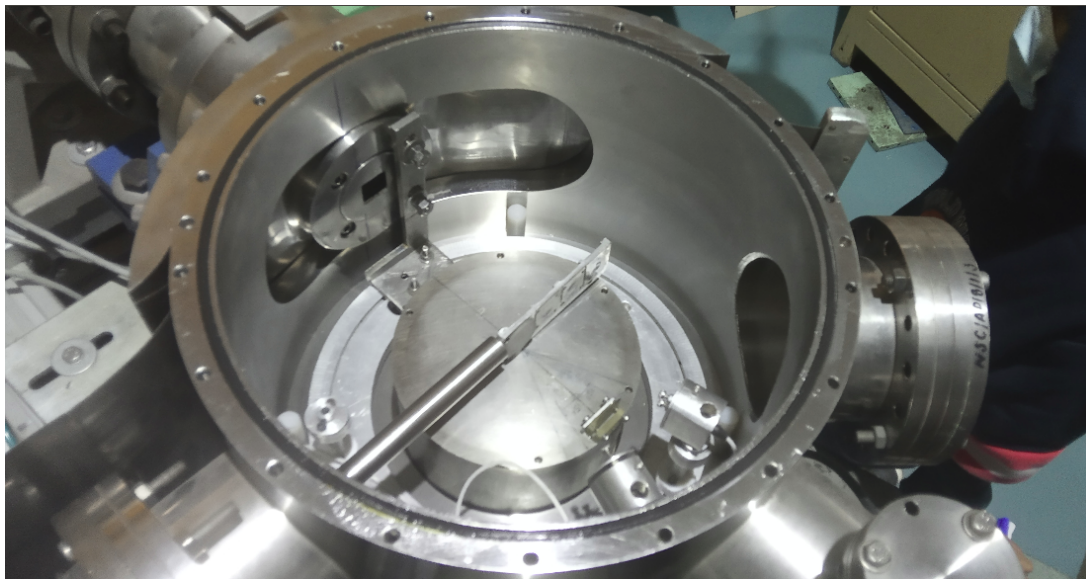


Figure 3.7: Inside view of target chamber with target ladder.

A carbon charge reset foil with a large surface area and a thickness of $10 \mu\text{g}/\text{cm}^2$ was placed 10 cm downstream of the target to reset the charge state of ERs to statistical distribution after possible internal conversion processes. The HIRA [6] separated ERs from the beam background and transported them to its focal plane (FP). The magnetic field values of HIRA were optimized for maximum transmission in each energy. For single beam energy, several exit channels are populated. However, HIRA is configured for the most dominant channel. HIRA magnetic fields were optimized by scanning the charge state, energy, and mass of the most probable ERs, for $^{12}\text{C}+^{184,186}\text{W}$ reactions at 64 MeV beam energy and for $^{12}\text{C}+^{182}\text{W}$ reaction at 84 MeV beam energy, which are listed in Table. 3.1.

Table 3.1: HIRA magnetic fields values, and charge state, energy, and mass of the most probable ERs, for $^{12}\text{C}+^{184,186}\text{W}$ reactions at 64 MeV beam energy and for $^{12}\text{C}+^{182}\text{W}$ reaction at 84 MeV beam energy.

System	Magnetic Field (T)	Energy of ERs (MeV)	Mass of ERs (amu)	Charge State of ERs
$^{12}\text{C}+^{182}\text{W}$	0.70116	4.50	191	7^+
$^{12}\text{C}+^{184}\text{W}$	0.81446	3.05	194	5^+
$^{12}\text{C}+^{186}\text{W}$	0.81191	3.00	196	5^+

The field values for other energies were scaled from the optimized values. For these experiments, the solid angle of acceptance for HIRA was kept at 5 msr . A two-dimensional position-sensitive MWPC was used at the HIRA's focal plane to detect ERs [9]. To separate the ERs from the beam-like particles, TOF was set up between the anode of the MWPC and the radio frequency (RF) of the beam pulsing system.

Bibliography

- [1] G. K. Mehta and A. P. Patro, Nucl. Instr. and Meth. A **268**, 334 (1988).
- [2] D. Kanjilal, S. Chopra, M. M. Narayanan, I. S. Iyer, V. Jha, R. Joshi, and S. K. Datta, Nucl. Instr. and Meth. A **328**, 97 (1993).
- [3] S. Chopra, N. S. Pawar, M. P. Singh, R. Kumar, J. Prasad, V. P. Patel, R. Pal, B. Kumar, S. Ojha, K. Devarani, T. Nandi, M. Sota, P. Barua, S. Gargari, R. Joshi, D. Kanjilal, and S. K. Datta, Pramana **59**, 753 (2002).
- [4] <https://www.iuac.res.in/pelletron-accelerator>.
- [5] C. N. Davids, Nucl. Instr. and Meth. B **204**, 124 (2003), 14th International Conference on Electromagnetic Isotope Separators and Techniques Related to their Applications.
- [6] A. K. Sinha, N. Madhavan, J. J. Das, P. Sugathan, D. O. Kataria, A. P. Patro, and G. K. Mehta, Nucl. Instrum. Methods Phys. Res. A **339**, 543 (1994).
- [7] <https://www.iuac.res.in/iuacoldwebsite/research/np/hira.html>.
- [8] G. Charpak, R. Bouclier, T. Bressani, J. Favier, and . Zupani, Nuclear Instruments and Methods **62**, 262 (1968).
- [9] J. Gehlot, A. Jhingan, T. Varughese, S. Nath, and N. Madhavan, DAE Symp. Nucl. Phys. **65**, 782 (2021).

Chapter 4

Data Analysis and Results

4.1 Introduction

In the case of $^{12}\text{C}+^{182,186}\text{W}$ reactions, the calculated fusion cross sections based on various theoretical models and systematics showed a large deviation with respect to the measured cross sections in the laboratory energy range 77 to 167 MeV [1, 2]. To study ERs for the reactions forming $^{194,196,198}\text{Hg}$, we have measured the evaporation residue cross sections for $^{12}\text{C}+^{182,184,186}\text{W}$ reactions at below and near the Coulomb barrier energies using HIRA spectrometer [3] as explained in Chapter 3. In this Chapter, we discuss the data analysis for these measurements and compare obtained cross sections with coupled-channel calculations and statistical model calculations.

4.2 Data analysis

The data were collected on an event by event basis, with each event containing information of the time of flight of ERs, positions and energy loss of the ERs in the MWPC. Timing and energy-loss signals from the MWPC at the focal plane (FP) of the spectrometer, along with the position data obtained from the wire grids using a delay line technique were processed using a CAMAC based data acquisition system. The data is analyzed in offline mode using the

software CANDLE [4]. HIRA separated ERs from majority of the high intense beam background and transported ERs to the FP. Also, some other reaction products (other than fusion products) and primary beam particle may reach the FP. To identify the ERs at the focal plane of the separator, we have created two dimensional spectrum of energy loss (ΔE) in MWPC versus time of flight (TOF), X-positions versus TOF and X-position vs ΔE . This method can be used to distinguish evaporation residues from beam-like particles. Figs. 4.1 - 4.3 shows the spectrum with ΔE versus time of flight (TOF), X-positions versus TOF, and X-position versus ΔE for the $^{12}\text{C}+^{182}\text{W}$ reaction at $E_{lab} = 70$ MeV. At this measurement HIRA set for the most probable ER energy 3.75 MeV, charge state 6^+ and mass 192 amu and the magnetic field 0.74869 T. These coincidence spectra were used to extract ER yields. The rectangular gate in the Figs. 4.1 - 4.3 show the ER events selected. The experimental data were normalized by dividing the ER counts (Y_{ER}) by the elastic scattering counts in the forward-angle normalization detectors (Y_{mon}). The total ER cross sections was extracted using Eq. 4.1.

$$\sigma_{ER} = \frac{Y_{ER}}{Y_{mon}} \left(\frac{d\sigma}{d\Omega} \right)_{Ruth} \Omega_{mon} \frac{1}{\epsilon_{HIRA}} \quad (4.1)$$

where ϵ_{HIRA} is the average transmission efficiency of HIRA and $\left(\frac{d\sigma}{d\Omega} \right)_{Ruth}$ is the differential Rutherford-scattering cross sections in the laboratory system, which is calculated using the equation

$$\left(\frac{d\sigma}{d\Omega} \right)_{Ruth} = 1.296 \left(\frac{Z_P Z_T}{E_{lab}} \right)^2 \left[\frac{1}{\sin^4 \frac{\theta}{2}} - 2 \left(\frac{A_P}{A_T} \right)^2 \right] \quad (4.2)$$

where Z_P and Z_T are the atomic numbers of the projectile and the target, respectively and θ is the monitor detector angle with respect to the beam direction. A_P and A_T are the masses of the projectile and targets respectively.

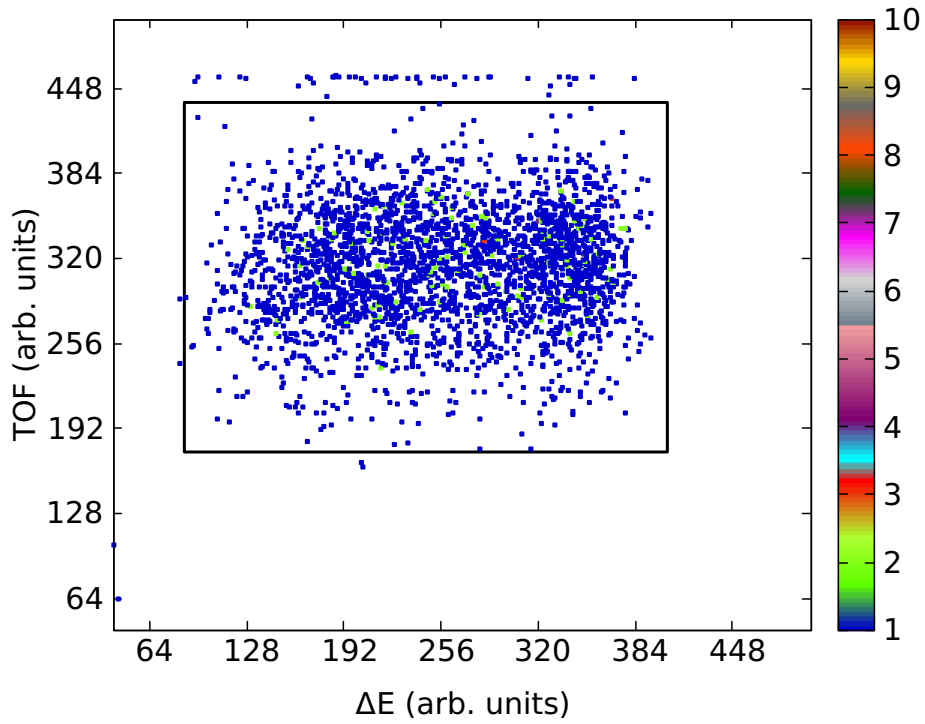


Figure 4.1: Two dimensional plot between ΔE and TOF of events recorded at the focal plane of HIRA for $^{12}\text{C}+^{182}\text{W}$ reaction at 70.0 MeV. The rectangular gate in the figure shows the ER events selected.

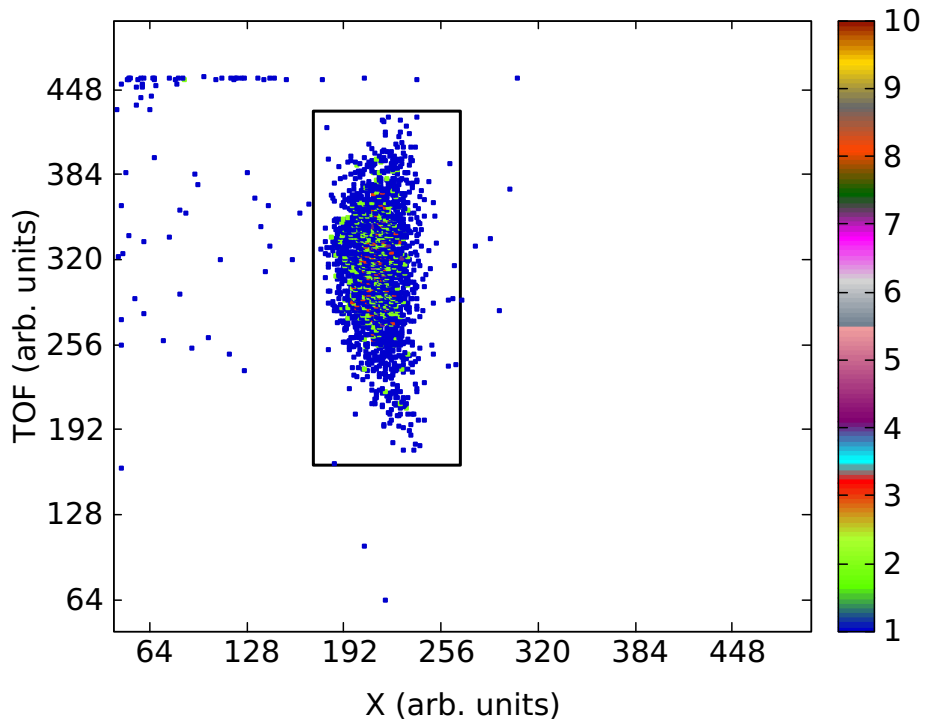


Figure 4.2: Two dimensional plot between X-position and TOF of events recorded at the focal plane of HIRA for $^{12}\text{C}+^{182}\text{W}$ reaction at 70.0 MeV. The rectangular gate in the figure shows the ER events selected.

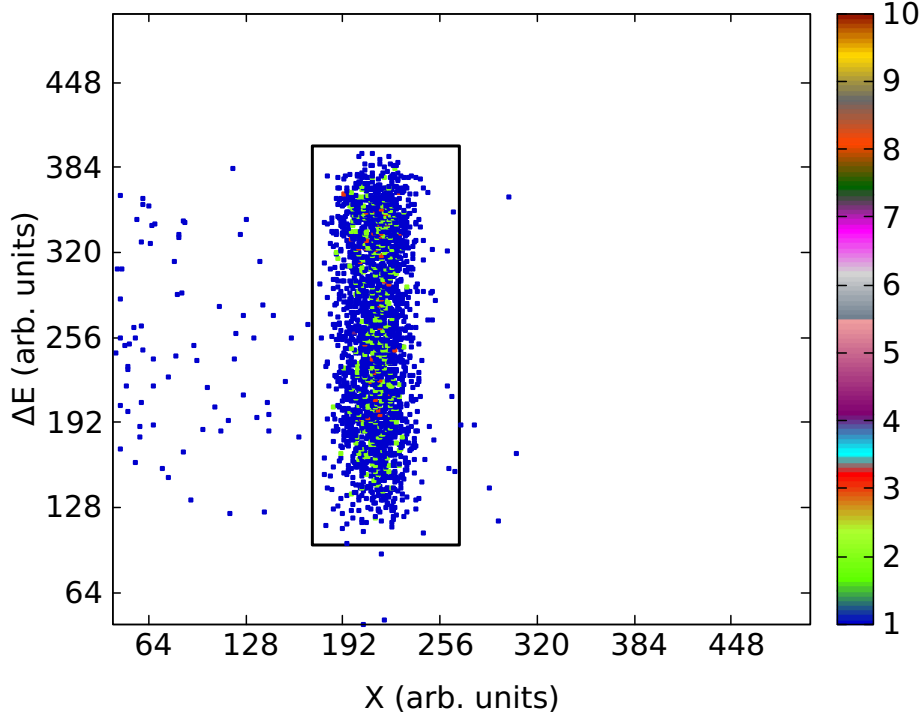


Figure 4.3: Two dimensional plot between X-position and ΔE of events recorded at the focal plane of HIRA for $^{12}\text{C}+^{182}\text{W}$ reaction at 70.0 MeV. The rectangular gate in the figure shows the ER events selected.

Apart from the experimental observables, transmission efficiency of the recoil separator is an important factor in an experiment. Transmission efficiency of the recoil mass spectrometer is the ratio of ERs reached at the focal plane to the total number of ERs produced at the target site. The transmission efficiency of the recoil mass spectrometer can be measured directly using the γ - coincidence method or it can be estimated [5]. In the case of weak evaporation channels, γ - coincidence method can not be employed effectively due to very low intensity of γ - rays. Also, measuring efficiencies for all exit channels of each E_{lab} will be a tedious task and not practicable. A Monte Carlo code developed by Nath *et al* [6], and compared the measured efficiencies for many cases and they found to be in agreement. We relied on this code for efficiency calculation of recoil mass spectrometer, HIRA. TERS generates the realistic values of ER displacement, angular distribution, charge state distribution, energy distribution etc, event by event and calculates the ER trajectories through the HIRA by first-order ion optical transfer matrices [5].

The transmission efficiency of HIRA depends on several factors like entrance channel mass asymmetry, beam energy, exit channel of interest, target thickness, angular acceptance of the HIRA, reference particle settings of the HIRA, and size of the FP detector. Among these parameters, the target thickness, angular acceptance of the HIRA, entrance channel mass asymmetry, and size of the FP detector remain unchanged throughout the experiment, while the rest of the parameters change [5]. The transmission efficiency of HIRA would be different for each E_{lab} . For a single beam energy, several exit channels are populated in the fusion reactions. However, HIRA field values were set for the most dominant channel. The magnetic field values of HIRA were optimized for maximum transmission in each energy. HIRA magnetic fields were optimized by scanning the charge state, energy, and mass of the most probable ERs, for $^{12}\text{C}+^{184,186}\text{W}$ reactions at 64 MeV beam energy and for $^{12}\text{C}+^{182}\text{W}$ reaction at 84 MeV beam energy. The field values for other energies were scaled from the optimized values. For $^{12}\text{C}+^{182,184,186}\text{W}$ reactions, the relative population for all ER channels was calculated using the statistical model code PACE4 [7–9]. The code was run for 100000 events at each energy for each particular reaction. Only evaporation channels with relative yield greater than 1% of total fusion cross sections were considered for efficiency calculations. The efficiency of HIRA is calculated for all these evaporation channels. The transmission efficiency for a given energy is calculated by taking the weighted average of all efficiencies over total ER, which has been used to calculate ER cross sections. The estimated error in HIRA efficiency is $\approx 10\%$ for $^{12}\text{C}+^{182,184,186}\text{W}$ reactions. For estimating the statistical errors in cross sections, we have extracted the $\frac{\sqrt{N}}{N}$ in focal plane detector as well as monitor detectors, where N is the total number of events detected in the detector. The errors due to uncertainties in the target thickness is not included in the listed errors.

In Fig. 4.4, we show the measured ER cross sections for the $^{12}\text{C}+^{182,184,186}\text{W}$ reactions as a function of center-of mass energy. Also, the measured ER cross sections for the $^{12}\text{C}+^{182,184,186}\text{W}$ reactions are listed in Table 4.1 - Table 4.3. The

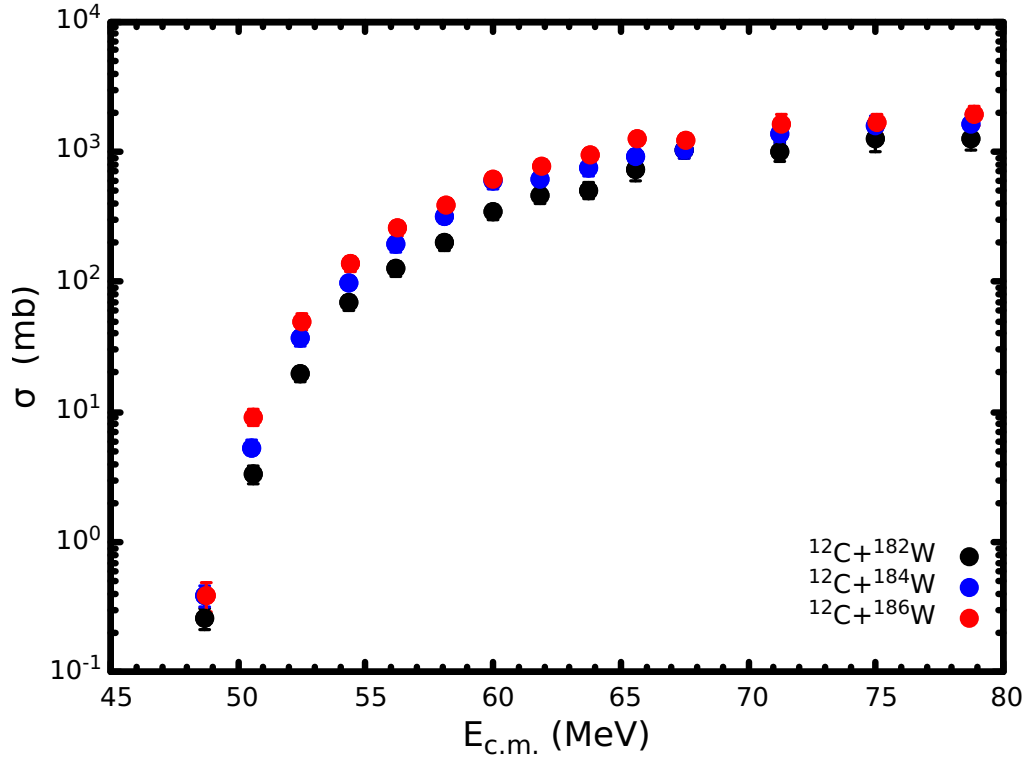


Figure 4.4: Measured ER cross sections for the $^{12}\text{C}+^{182,184,186}\text{W}$ reactions.

Table 4.1: Measured evaporation residue cross sections (σ_{ER}) for $^{12}\text{C}+^{182}\text{W}$ reaction. The quoted errors include the statistical error plus the error in the estimation of transmission efficiency.

$^{12}\text{C}+^{182}\text{W}$				
E_{lab} (MeV)	$E_{c.m.}$ (MeV)	E^* (MeV)	σ_{ER} (mb)	$\delta\sigma_{ER}$ (mb)
52	48.69	32.63	0.26	0.05
54	50.57	34.50	3.33	0.50
56	52.45	36.38	20	3
58	54.33	38.26	69	9
60	56.20	40.14	127	16
62	58.08	42.02	202	26
64	59.96	43.90	346	45
66	61.84	45.77	461	60
68	63.72	47.65	502	69
70	65.59	49.53	733	145
72	67.47	51.41	1022	136
76	71.23	55.16	1007	174
80	74.98	58.92	1256	265
84	78.74	62.67	1252	231

Table 4.2: Measured evaporation residue cross sections (σ_{ER}) for $^{12}\text{C}+^{184}\text{W}$ reactions. The quoted errors include the statistical error plus the error in the estimation of transmission efficiency.

$^{12}\text{C}+^{184}\text{W}$				
E_{lab} (MeV)	$E_{c.m.}$ (MeV)	E^* (MeV)	σ_{ER} (mb)	$\delta\sigma_{ER}$ (mb)
52	48.67	34.79	0.39	0.07
54	50.55	36.67	5.35	0.70
56	52.44	38.56	37	5
58	54.32	40.44	99	12
60	56.20	42.32	194	24
62	58.08	44.20	320	40
64	59.96	46.08	593	74
66	61.84	47.96	619	77
68	63.72	49.84	743	93
70	65.60	51.72	903	109
72	67.48	53.60	1018	129
76	71.24	57.36	1373	234
80	75.00	61.12	1575	298
84	78.75	64.87	1637	276

Table 4.3: Measured evaporation residue cross sections (σ_{ER}) for $^{12}\text{C}+^{186}\text{W}$ reactions. The quoted errors include the statistical error plus the error in the estimation of transmission efficiency.

$^{12}\text{C}+^{186}\text{W}$				
E_{lab} (MeV)	$E_{c.m.}$ (MeV)	E^* (MeV)	σ_{ER} (mb)	$\delta\sigma_{ER}$ (mb)
52	48.73	37.18	0.39	0.10
54	50.61	39.06	9.15	1.34
56	52.50	40.94	49	7
58	54.38	42.82	136	17
60	56.26	44.70	260	34
62	58.14	46.58	390	48
64	60.02	48.46	616	78
66	61.90	50.34	778	99
68	63.78	52.23	937	120
70	65.66	54.11	1267	156
72	67.54	55.99	1229	152
76	71.30	59.75	1639	290
80	75.06	63.51	1659	273
84	78.83	67.27	1925	332

quoted errors in Table 4.1 - Table 4.3 include the statistical error plus the error in the estimation of transmission efficiency. In order to account for energy loss, energy loss corrections were applied to both the carbon backing and the target's half-thickness with the assumption that the projectile-target interaction occurs in the middle of the target. $E_{c.m.}$ in Table 4.1-Table 4.3 is the energy in center of mass frame after energy loss corrections. For calculating excitation energy (E^*) Q-values are taken from [10].

4.3 Coupled-channel calculations

The measured ER cross sections for the $^{12}\text{C}+^{182,184,186}\text{W}$ reactions were analyzed using coupled-channel calculations to investigate the effect of coupling of different excited states of the target nuclei in the sub-barrier energy region. The coupled-channel code CCFULL calculates fusion cross sections and the mean angular momenta of the CN under the influence of couplings between the relative motion and nuclear collective motions [11, 12].

Fusion cross section is the sum of ER cross section (σ_{ER}) and fission cross section (σ_{fiss}). Statistical model [13–15] calculations have carried out for $^{12}\text{C}+^{182,184,186}\text{W}$ reactions in the laboratory energy range 52-84 MeV and observed that the calculated fission cross sections are negligibly small in the this energy region. At 84 MeV lab energy, the estimated fission cross sections is to be 6%, 4% and 2% for $^{12}\text{C}+^{182}\text{W}$, $^{12}\text{C}+^{184}\text{W}$ and $^{12}\text{C}+^{186}\text{W}$ respectively. In these reactions, fission become significant only at very high excitation energies [1, 2, 16, 17]. Considering these, in the measured energy range, we can equate capture cross sections (σ_{cap}), fusion cross sections as well as σ_{ER} ($\sigma_{cap} \approx \sigma_{fus} \approx \sigma_{ER}$). Hence, the fusion cross sections calculated using CCFULL [11, 12, 18] directly compare with the measured ER cross sections.

4.3.1 $^{12}\text{C}+^{182}\text{W}$ reaction

In the CC calculations the Woods-Saxon parametrization of the nuclear potential is used. In the current calculations, we have used the depth parameter of the Woods-Saxon potential V_0 , the radius parameter r_0 , and the diffuseness parameter a_0 as 72.0 MeV, 1.15 fm and 0.70 fm respectively. These parameters are obtained by a systematics analysis. First, we have reproduced the measured fusion cross section for $^{16}\text{O}+^{176,180}\text{Hf}$ forming $^{192,196}\text{Hg}$ CN [19], using the potential parameters $V_0 = 86.6$ MeV, $r_0 = 1.15$ fm and $a_0 = 0.70$ fm, selected from that of the nearest systems $^{16}\text{O}+^{186}\text{W}$ [20] and $^{16,18}\text{O}+^{181}\text{Ta}$ [21]. By scaling only the depth parameter, V_0 of $^{16}\text{O}+^{176,180}\text{Hf}$ reactions from 86.6 MeV to 72.0 MeV, we were able to reproduce the measured cross sections for $^{12}\text{C}+^{182}\text{W}$ reaction at energies above the Coulomb barrier. CC calculations using this potential parameters along with measured fusion cross sections are shown in Fig. 4.5. From this figure it is clear that the 1D-BPM calculations successfully explain the measured

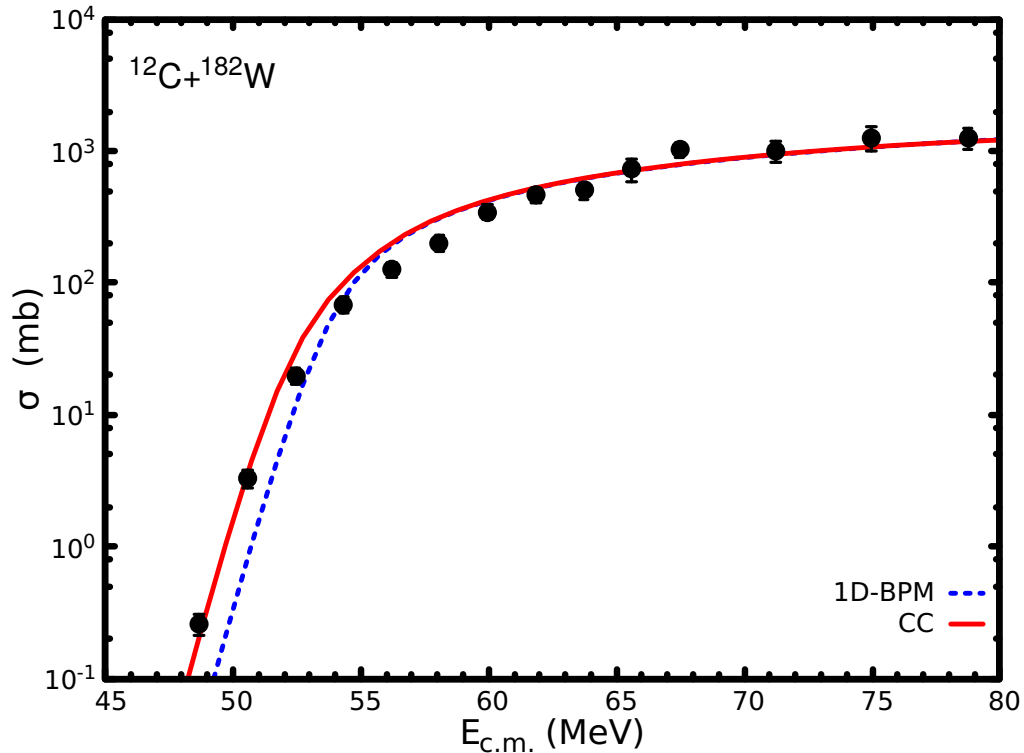


Figure 4.5: Measured fusion cross sections along with CC calculation for the $^{12}\text{C}+^{182}\text{W}$ reaction.

fusion cross sections at higher excitation energies. However, it fails to reproduce the fusion cross sections at below the Coulomb barrier energy region. It is known that the sub-barrier fusion cross sections are influenced by coupling of projectile and/or target deformations. In CC calculations, we have included the deformations, quadrupole and hexadecapole deformations, for ^{182}W nucleus, which reproduce the experimental sub-barrier measurements, where the projectile is assumed to be inert. The used parameters of the static quadrupole and hexadecapole deformations are $\beta_2 = 0.251$ [22] and $\beta_4 = -0.066$ [23] respectively, for the ^{182}W target. Also, the excitation energy of the first 2^+ state, 0.100 MeV [22], in the ground state rotational band of the target nuclei used in the CCFULL calculations. For the second and higher excited states, the excitation energy and couplings are often assumed to be those achieved within the coupling scheme. From Fig. 4.5, it is clear that CC calculations with the inclusion of target deformation effects explain the measured fusion cross section for $^{12}\text{C}+^{182}\text{W}$ reaction.

4.3.2 $^{12}\text{C}+^{184}\text{W}$ reaction

For $^{12}\text{C}+^{184}\text{W}$ reaction, we have used the same potential parameters of $^{12}\text{C}+^{182}\text{W}$ reaction $V_0 = 72.0$ MeV, $r_0 = 1.15$ MeV, and $a_0 = 0.70$ fm. The measured fusion cross sections and CCFULL calculations are shown in Fig. 4.6. From this figure it is clear that using these potential parameters, the CC calculations explain the measured cross sections at higher excitation energies.

In order to explain the observed sub-barrier measurement, we have included the quadrupole and hexadecapole deformation of ^{184}W nucleus into the CC calculations. Using quadrupole deformation parameter (β_2) of 0.262 [22] and hexadecapole deformation (β_4) of -0.093 [23] of ^{184}W nucleus, we have calculated the excitation functions of $^{12}\text{C}+^{184}\text{W}$ reaction.

From Fig. 4.6, we can observe that CC calculations with the static deformation effects of ^{184}W nucleus show reasonable agreement with the measured fusion cross section in the entire excitation energy. However, calculations show a slight

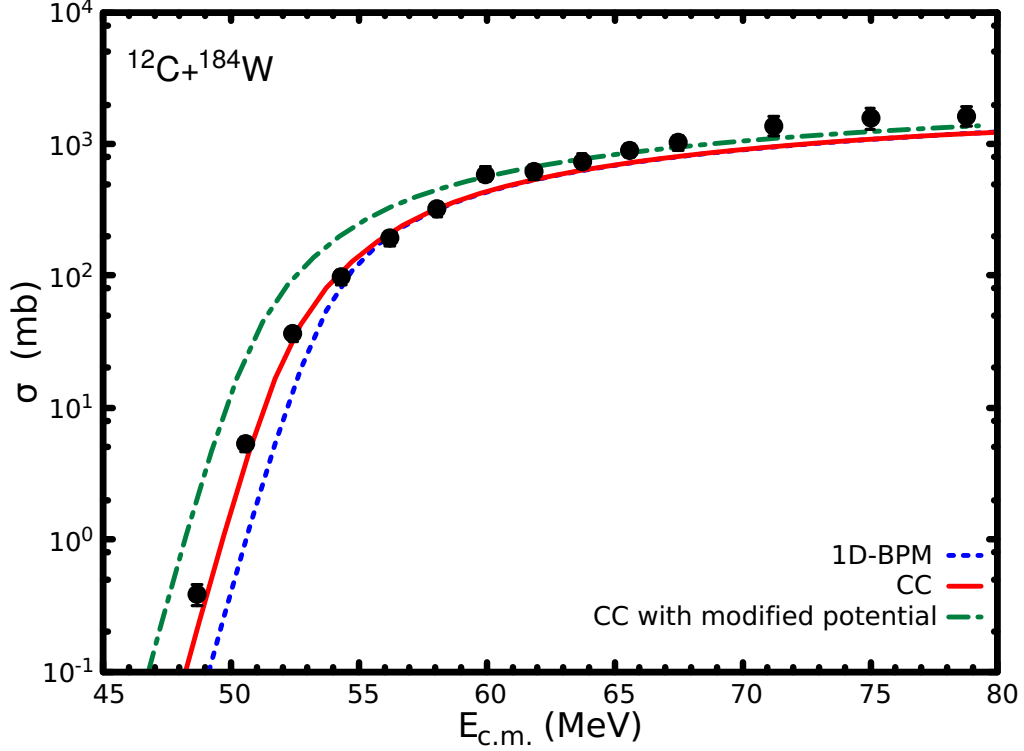


Figure 4.6: Measured fusion cross sections along with CC calculation for the $^{12}\text{C}+^{184}\text{W}$ reaction.

deviation at higher excitation energies.

In order to explain this observed deviations at higher excitation energies, we have used a different potential parameters, $V_0 = 105$ MeV, $r_0 = 1.15$ fm and $a_0 = 0.71$ fm for the reaction $^{12}\text{C}+^{184}\text{W}$. However, with the use of these potential parameters, CC calculations over predict the measured fusion cross sections at sub-barrier energies.

4.3.3 $^{12}\text{C}+^{186}\text{W}$ reaction

CC calculations were employed for $^{12}\text{C}+^{186}\text{W}$ reaction with the potential parameters $V_0 = 72$ MeV, $r_0 = 1.15$ fm and $a_0 = 0.70$ fm. For including the deformation effects of ^{186}W nuclei in CC calculations, we have taken into account their quadrupole ($\beta_2 = 0.226$ [22]) and hexadecapole ($\beta_4 = -0.095$ [23]) deformation parameters in the CCFULL calculations. The results of CC calculations along with the measured fusion cross sections are shown in Fig. 4.7.

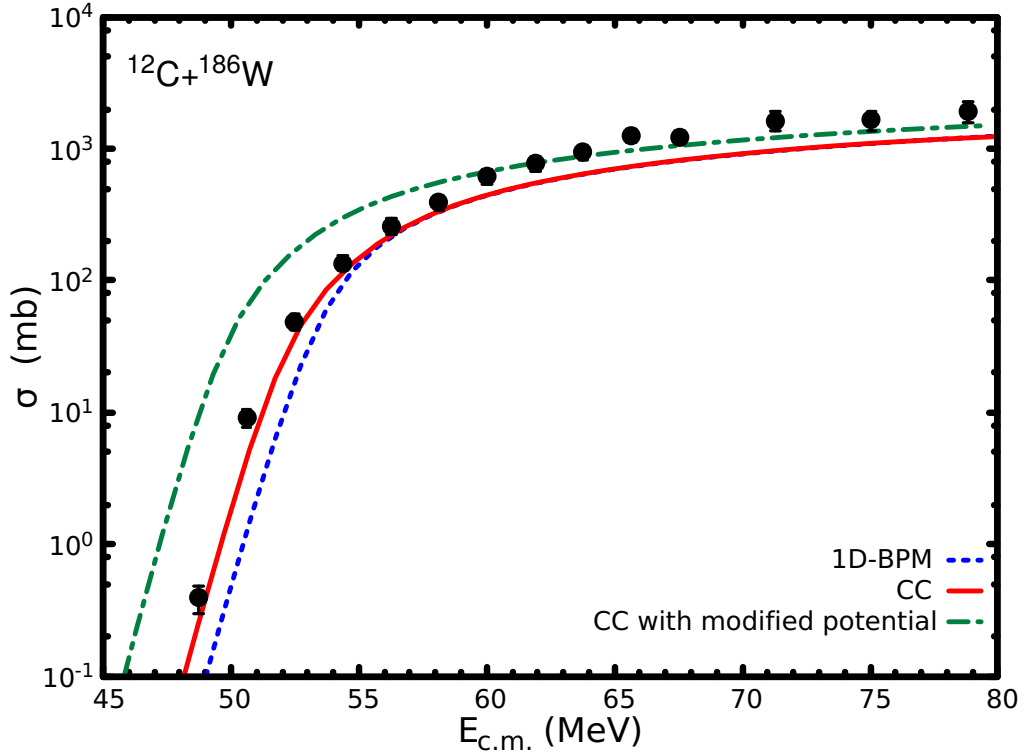


Figure 4.7: Measured fusion cross sections along with CC calculation for the $^{12}\text{C}+^{186}\text{W}$ reaction.

CC calculation with static deformation of the target nucleus reproduces the sub-barrier fusion cross sections quite well. Overall, CC calculations show reasonable agreement with the measurements for $^{12}\text{C}+^{186}\text{W}$ reaction. Similar in the case of $^{12}\text{C}+^{184}\text{W}$ reaction, CC calculations for $^{12}\text{C}+^{186}\text{W}$ reaction also shows slight deviations at higher excitation energies. If one uses a different potential, $V_0 = 115$ MeV, $r_0 = 1.16$ fm, and $a_0 = 0.73$ fm for $^{12}\text{C}+^{186}\text{W}$ reaction, CC calculations show good agreement with the measured fusion cross sections at higher excitation energies. With the use of these potential parameters, CC calculations over predict the measured fusion cross sections at sub-barrier energies. In Fig. 4.7, CC calculations with these modified potentials are also shown.

CC calculations is quite successful in describing the effects of static deformation and vibrational degrees of freedom in sub-barrier fusion cross section enhancement. However, the exact role of transfer channels is in sub-barrier fusion cross

section is not understood completely [24]. Kohley *et al* [25] observed that there is no noticeable enhancement in $^{132}\text{Sn}+^{58}\text{Ni}$ and $^{130}\text{Te}+^{58,64}\text{Ni}$ fusion cross sections, even though they have positive Q-value neutron transfer (PQNT) channels.

The $^{12}\text{C}+^{186}\text{W}$ reaction is having a positive transfer Q-value of 0.177 MeV for the -2n transfer reaction. All the other neutron transfer reactions have negative Q-values. Without the inclusion of the effects of PQNT channel, the fusion cross sections for $^{12}\text{C}+^{186}\text{W}$ reaction shows a reasonably good agreement with the CC calculations at sub-barrier energies. i.e., the PQNT have no effects on the observed sub-barrier fusion cross sections of $^{12}\text{C}+^{186}\text{W}$ reaction.

4.4 Statistical model calculations

The compound nucleus is a very complex many-body system, and its decay is described by statistical evaporation models. To study the detailed de-excitation processes of $^{194,196,198}\text{Hg}$ compound nuclei, we have carried out statistical model calculations for $^{12}\text{C}+^{182,184,186}\text{W}$ reactions. The statistical model code HIVAP (Heavy Ion VAPorisation statistical-evaporation model) [13–15] was used to investigate the de-excitation of the formed compound nuclei. HIVAP code takes into account the competition between various decay channels, such as neutron, proton, and α -particle evaporation, gamma-ray emissions, and fission. The HIVAP code using the standard set of Reisdorf and Schädel parameters is successful in the prediction of fusion reaction cross sections [14]. To explain the measured ER cross sections for $^{12}\text{C}+^{182,184,186}\text{W}$ reactions we have modified some of the parameters which are related to nuclear potential and fission barrier.

Level densities and nuclear masses are the main input parameters required to estimate the fission barrier. According to Reisdorf's macroscopic description [13, 14], the nuclear level densities in fission and evaporation channels are provided by ratios of level densities $a_f/a_n \geq 1$, due to the different nuclear shapes at the saddle point (fission) and equilibrium state (particle emission). For mass asymmetric systems, fission is significant only at energies well above the fusion barrier. At

these high energies, fission has a significant influence on the production cross sections of ERs. The HIVAP calculation is primarily determined by the fission barrier scaling factor (k_f) of the liquid drop (LD) fission barrier (B_f^{LD}) [26], which modify the fission barrier as

$$B_f(l) = k_f B_f^{LD} + \delta W_{g.s.} \quad (4.3)$$

in which $\delta W_{g.s.}$ is the ground state shell correction.

The potential parameters used for HIVAP calculations for $^{12}\text{C}+^{182,184,186}\text{W}$ are $V_0 = 72$ MeV, $r_0 = 1.12$ fm and $D = 0.62$ fm. Simultaneous analysis of fission and ER cross sections for $^{12}\text{C}+^{182,184,186}\text{W}$ reactions allow us to obtain the value of fission barrier. The fission cross sections for the systems $^{12}\text{C}+^{182,184,186}\text{W}$ were taken from literatures [1, 2, 16, 17]. Delagrange *et al.* [2] measured fission cross sections for $^{12}\text{C}+^{182,186}\text{W}$ reactions in the 56-87 MeV excitation energies. At $E^* = 82$ MeV, they observed a significant difference in the fission yield of ^{194}Hg CN in comparison to ^{198}Hg compound nuclei, $\sigma_{fiss} = 536 \pm 52$ mb for ^{194}Hg and $\sigma_{fiss} = 166 \pm 68$ mb for ^{198}Hg . This discrepancy might be attributed to the competition between evaporation of neutrons and fission. The HIVAP calculations with $k_f = 0.96$ show good agreement with the measured fission cross sections for $^{12}\text{C}+^{182,184,186}\text{W}$ reactions. From the HIVAP calculations, at $E^* = 82$ MeV, we obtained $\sigma_{fiss} = 521$ mb for ^{194}Hg CN and $\sigma_{fiss} = 209$ mb for ^{198}Hg CN. This means our statistical model calculations with $k_f = 0.96$ for $^{12}\text{C}+^{182,184,186}\text{W}$ reactions explains measured fission cross sections from literature [1, 2, 16, 17].

To explain the sub-barrier measurements we have considered the static deformation effects of tungsten nuclei in statistical model calculations, we have taken into account their quadrupole moment $Q_2=650, 616$ and 593 fm^2 [22] respectively for $^{182,184,186}\text{W}$ nuclei. These calculations reasonably explained the measured ER as well as fission cross sections [1, 2, 16, 17]. Comparison of statistical model calculation with the measured ER cross sections for $^{12}\text{C}+^{182,184,186}\text{W}$ reactions are shown in Figs. 4.8 - 4.10 respectively, where solid circles are the present measure-

ments and solid lines are corresponding HIVAP calculations. In the inset figures, we show the fission cross sections available in literature and their comparison with the calculations.

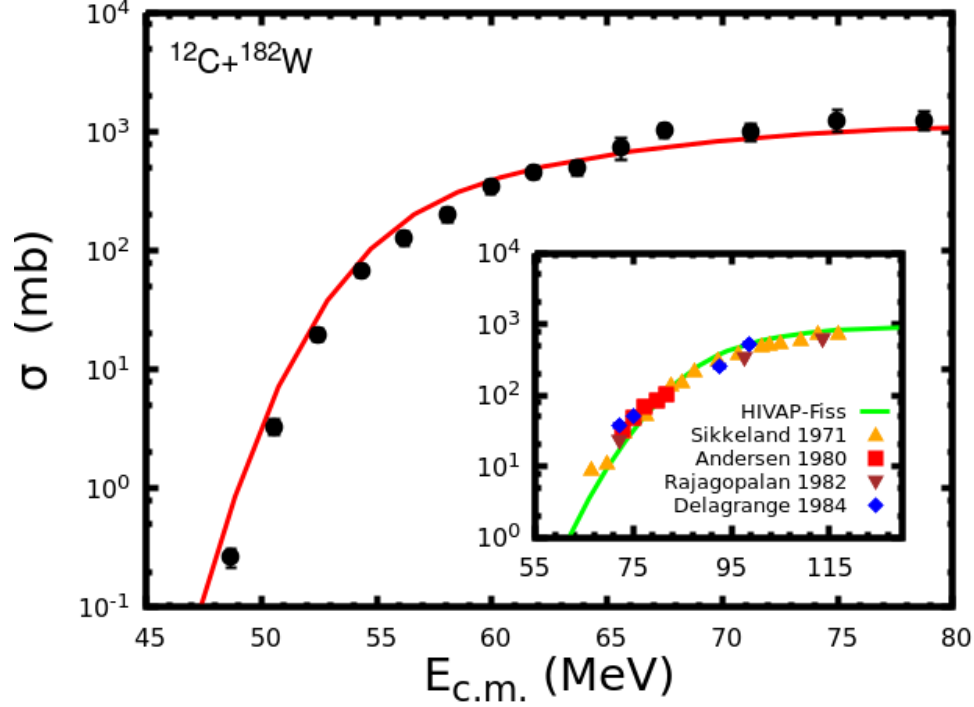


Figure 4.8: Experimental ER and fission excitation functions for $^{12}\text{C}+^{182}\text{W}$ reaction along with HIVAP calculations. The fission cross sections from literature [1, 2, 16, 17] and the corresponding HIVAP calculations shown in inset figures.

From Figs. 4.8, 4.9 and 4.10, it is clear that the statistical model calculations with fission barrier scaling factor, $k_f = 0.96$ for $^{12}\text{C}+^{182,184,186}\text{W}$ reactions explains our measured ER as well as measured fission cross sections from literature [1, 2, 16, 17]. Usually, in the case of an asymmetric system, the excitation functions at high energies describe with the variation of k_f . When the ER and fission excitation functions are fairly in agreement with the calculations with the same parameter values of the nuclear potential and k_f (fission barrier scaling factor) across the whole range of excitation energy, the CN formation probability is usually assumed to be unity in the case of an asymmetric system [27]. The HIVAP calculations using the same parameter values of the nuclear potential and k_f explain the measured ER excitation functions in the entire energy region

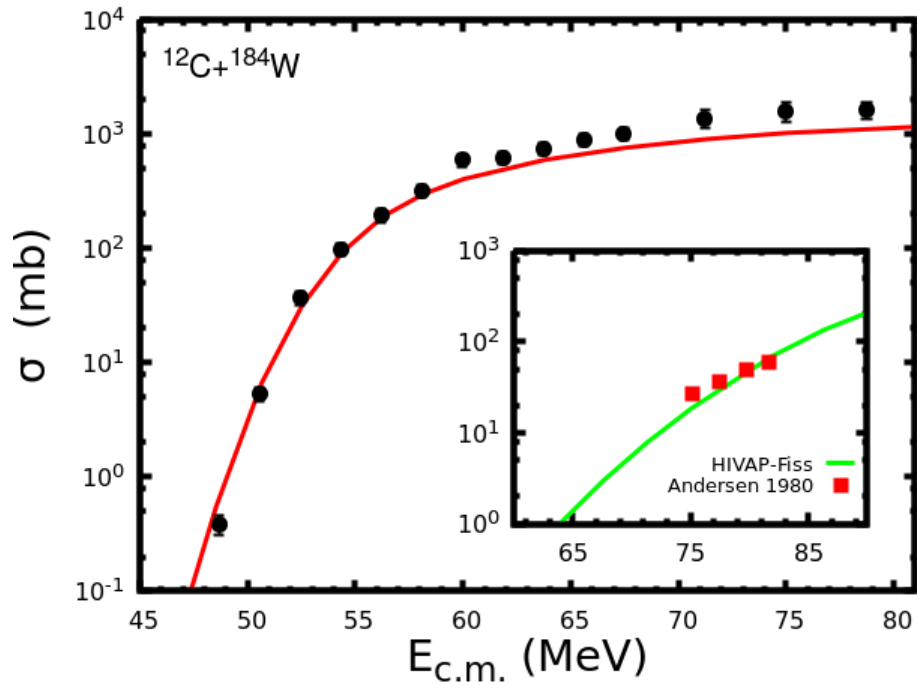


Figure 4.9: Experimental ER and fission excitation functions for $^{12}\text{C}+^{184}\text{W}$ reaction along with HIVAP calculations. The fission cross sections from literature [17] and the corresponding HIVAP calculations shown in inset figures.

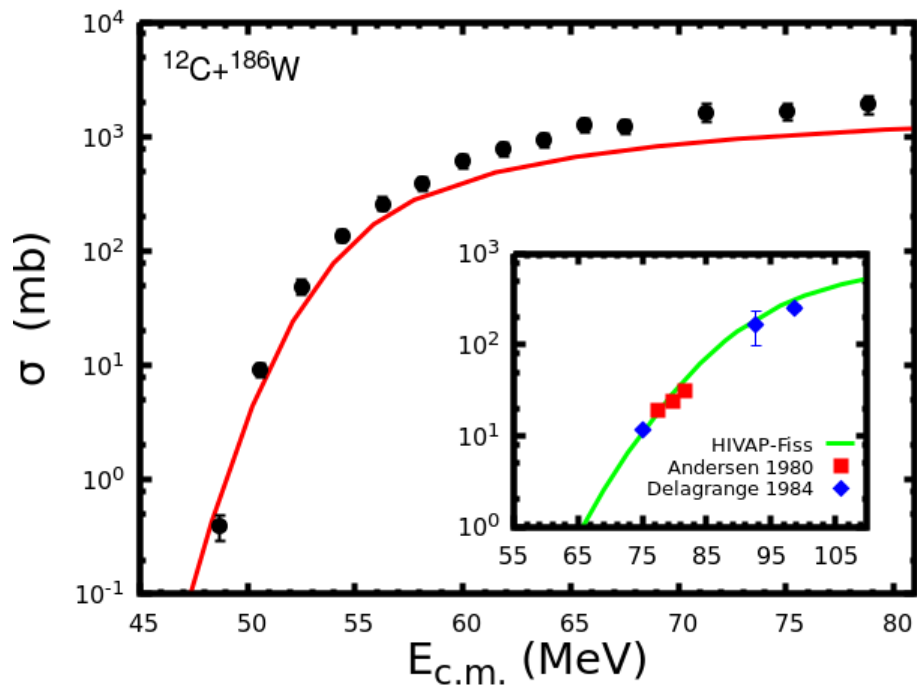


Figure 4.10: Experimental ER and fission excitation functions for $^{12}\text{C}+^{186}\text{W}$ reaction along with HIVAP calculations. The fission cross sections from literature [2, 17] and the corresponding HIVAP calculations shown in inset figures.

for $^{12}\text{C}+^{182,184,186}\text{W}$ reactions. This leads to the conclusion that the non-compound nuclear fission (NCNF) processes are not affecting the ER production of ^{12}C induced reactions forming $^{194,196,198}\text{Hg}$ CN. In the entire energy region, the measured ER and fission cross sections show reasonably good agreement with the statistical model calculations without including the dissipation or viscosity effects. This indicates the absence of dissipative effects in ER cross sections in these reactions.

4.5 Comparison with the nearby systems

Non-compound nuclear fission (NCNF) processes are usually not expected in reactions induced by ^{16}O and projectiles lighter than ^{16}O . However, a recent comprehensive study suggests that the NCNF may also play a role in ^{16}O -induced reactions [28]. In order to have a better understating of the entrance channel effects on the ER cross sections, ER measurements of additional systems that produce the $^{194-198}\text{Hg}$ CN and others close to these nuclei, $A = 194-198$, are considered for comparison with the present work. To explore the effects of the entrance channel, we compared the reduced cross sections ($\tilde{\sigma} = \frac{\sigma_{ER}}{\pi R_B^2}$, where R_B is the Bass [29] barrier radius) of $^{194,195,196,198}\text{Hg}$ CN formed by various projectile-target combinations, as shown in Fig. 4.11. If one compares $^{12}\text{C}+^{182,184,186}\text{W}$ reactions, no noticeable effects on the sub-barrier enhancement due to the addition of four neutrons (^{182}W to ^{186}W) is seen. In this figure, at higher excitation energies, $^{19}\text{F}+^{175}\text{Lu}$ reaction, forming ^{194}Hg CN, shows a significant reduction in reduced cross sections, which has been attributed to the increase in the level density parameter ratio [30].

Fig. 4.12 shows a comparison of reduced cross sections of $^{194,196,198}\text{Hg}$ CN with the reactions forming CN close to Hg nuclei. A comparison of present measurements with neighboring systems does not show any significant effect of the entrance channel mass asymmetry over the entire energy range. For all reactions considered, the reduced cross sections are comparable at both below

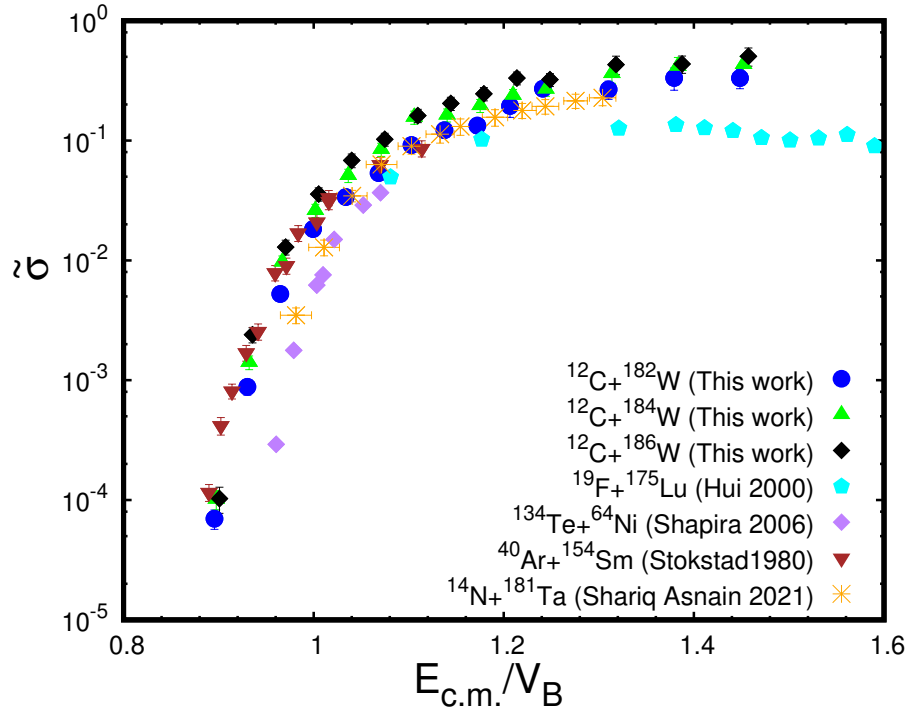


Figure 4.11: Reduced cross sections as a function of $E_{c.m.}$ for reactions forming Hg nuclei. Here reduced cross sections ($\tilde{\sigma}$) is obtained by $\frac{\sigma E_B}{\pi R_B^2}$ and V_B is the Bass barrier.

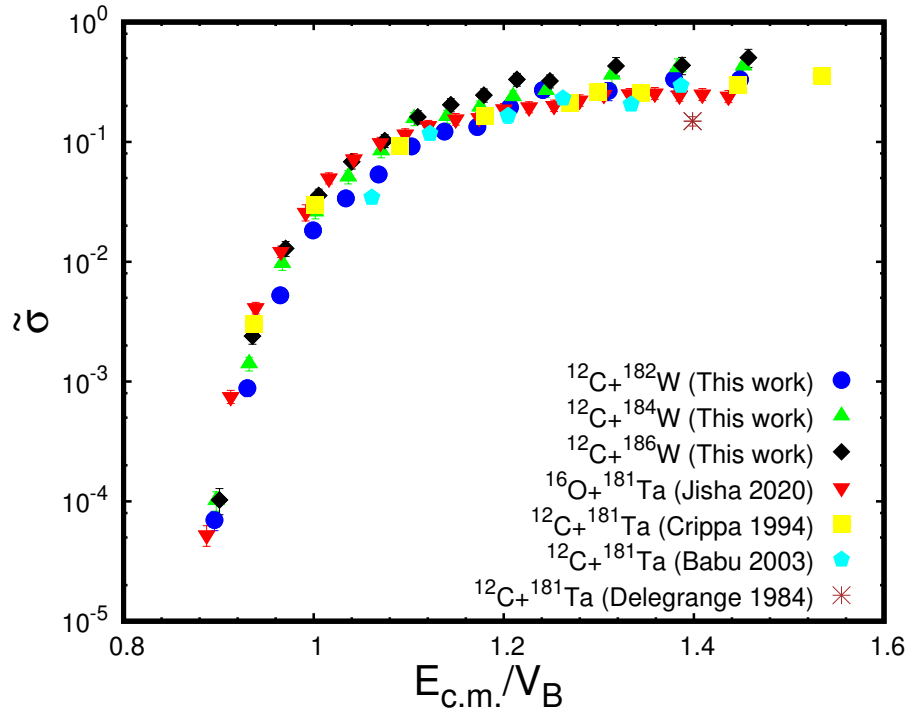


Figure 4.12: Reduced cross sections as a function of $E_{c.m.}$ for reactions forming CN close to Hg nuclei. Here reduced cross sections ($\tilde{\sigma}$) is obtained by $\frac{\sigma E_B}{\pi R_B^2}$ and V_B is the Bass barrier.

and above the barrier energy regions. When compared to the ER measurements of the $^{12}\text{C}+^{181}\text{Ta}$ reaction reported by Crippa *et al.* [31] and Babu *et al.* [32], the measurements by Delagrangé *et al.* [2] show smaller cross sections at higher excitation energies. This can be attributed to missing of ER events in Delagrangé *et al.* [2] detection system due to its small recoil energy.

4.6 Discussion

In order to get more information from experimental findings about compound-nucleus reactions for the present systems, we have compared the measurements with coupled-channel and statistical model calculations. The coupled-channel calculations without coupling reproduced the measured data quite well at higher excitation energies. We have accounted for the static deformation effects of the targets to reproduce the reported sub-barrier cross sections. In order to explain the measured sub-barrier cross sections, we have included the quadrupole (β_2) and hexadecapole (β_4) deformations of the target nuclei in the CC calculations. Using the static deformations effects of the $^{182,184,186}\text{W}$ targets, CC calculations explain the fusion cross sections for $^{12}\text{C}+^{182,184,186}\text{W}$ reactions, where the projectile is assumed to be inert. Overall, our measurements for $^{12}\text{C}+^{182,184,186}\text{W}$ reactions show reasonably good agreement with the CC calculations. We could not see any discrepancy between measurements and the calculated cross sections. Also, based on Fig. 4.4, one can conclude that the addition of four neutrons (^{182}W to ^{186}W) has no discernible effect on the observed sub-barrier measurements. Our study shows that coupled-channel calculations with the coupling of inelastic excitation channels and static effects of target nuclei provide a reasonably good description of all measurements.

The statistical model calculations with fission barrier scaling parameter, $k_f = 0.96$ reproduced the measured fission cross sections of the $^{12}\text{C}+^{182}\text{W}$ reaction [1, 2, 16, 17]. Furthermore, corresponding ER cross sections from statistical

Table 4.4: Comparison of present measurements for $^{12}\text{C}+^{182,186}\text{W}$ reactions with Rajagopalan *et al.* [1] and Delagrange *et al.* [2].

E_{lab} (MeV)	Present work σ_{ER} (mb)	Rajagopalan [1]			Delagrange [2]		
		σ_{ER} (mb)	σ_{fiss} (mb)	σ_{fus} (mb)	σ_{ER} (mb)	σ_{fiss} (mb)	σ_{fus} (mb)
$^{12}\text{C}+^{182}\text{W}$							
76	1007±174	-	-	-	-	-	-
77	-	545±10	23±8	568±10	-	37.6±3.5	-
80	1256±265	-	-	-	475±50	51.2±5.6	526±50
$^{12}\text{C}+^{186}\text{W}$							
80	1659±273	-	-	-	350±50	11.6±0.27	362±50

model calculations agree fairly well with the measured ER excitation functions. We successfully explained the fission and ER cross sections using the same k_f value of 0.96 for $^{12}\text{C}+^{182,184,186}\text{W}$. Without taking into account the dissipation or viscosity effects, the measured ER and fission cross sections for the whole energy area show good agreement with the statistical model calculations. Therefore, we can conclude that there is no evidence of a dissipative effect in ER measurements in the studied energy region.

ER and fission cross sections for $^{12}\text{C}+^{182,186}\text{W}$ reactions were measured by Rajagopalan *et al.* [1] and Delagrange *et al.* [2]. Their measured and calculated fusion cross sections show discrepancy in 77-167 MeV laboratory energy range. Therefore, the fusion cross sections obtained in our experiments and calculations are of immediate interest for their comparison with the measurements by Rajagopalan *et al.* [1] and Delagrange *et al.* [2]. In Figs. 4.13, 4.14, and Table 4.4 we compare the measured fusion cross sections for $^{12}\text{C}+^{182,186}\text{W}$ reactions with the measurements performed by Rajagopalan *et al.* [1] and Delagrange *et al.* [2]. Also, in these figures, we have shown the present statistical model calculations along with the calculations based on systematics [1, 2].

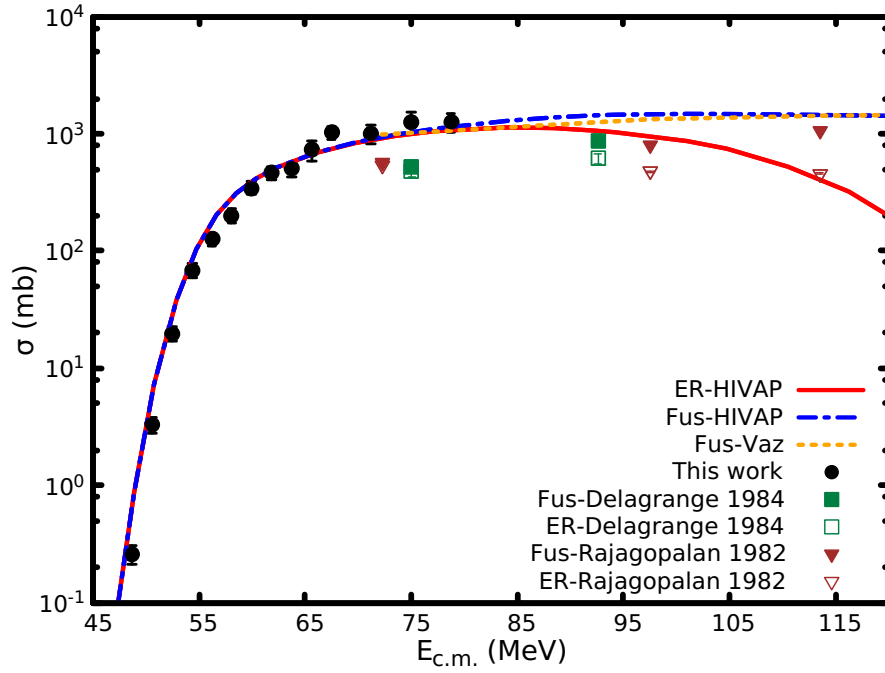


Figure 4.13: Comparison of present measurements and calculations with the measurements and calculation by Rajagopalan *et al.* and Delagrange *et al.* for $^{12}\text{C}+^{182}\text{W}$ reaction. Solid symbols are the measured cross sections, solid lines are the HIVAP calculations and dotted lines are the fusion cross sections from systematics [1, 2].

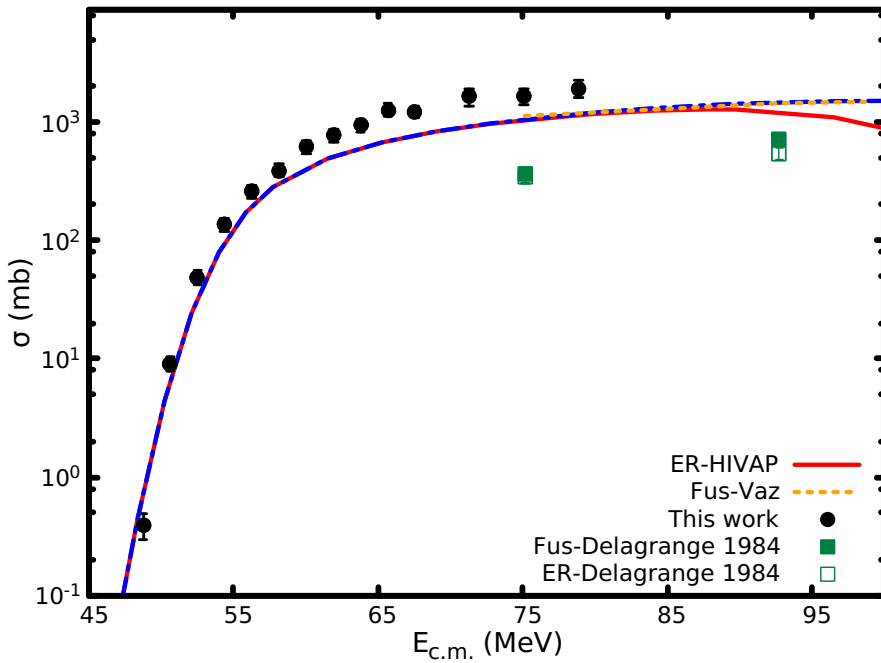


Figure 4.14: Comparison of present measurements and calculations with the measurements and calculation by Delagrange *et al.* for $^{12}\text{C}+^{186}\text{W}$ reaction. Solid symbols are the measured cross sections, solid lines are the HIVAP calculations and dotted lines are the fusion cross sections from systematics [2].

From Fig. 4.13 and Table. 4.4, it is clear that the fusion cross sections measured by Rajagopalan *et al.* and Delagrange *et al.* are smaller by a factor of ~ 2 compared to our measurements for $^{12}\text{C}+^{182}\text{W}$ reaction. Our statistical model calculation for the $^{12}\text{C}+^{182}\text{W}$ reaction is in agreement with the cross sections obtained by Rajagopalan *et al.* [1, 2] using systematics. Moreover, their calculations for the $^{12}\text{C}+^{182}\text{W}$ reaction show good agreement with our measurements.

Delagrange *et al.* [2] measured ER and fission cross sections for $^{12}\text{C}+^{186}\text{W}$ reaction. In Fig. 4.14, we have compared the measurements and calculations by Delagrange *et al.* with our measurements and calculations for $^{12}\text{C}+^{186}\text{W}$ reaction. From Fig. 4.14 and Table. 4.4, it is clear that the fusion cross sections measured by Delagrange *et al.* are smaller by a factor of ~ 5 compared to our measurements for $^{12}\text{C}+^{186}\text{W}$ reaction. Our calculation using the statistical model for the $^{12}\text{C}+^{186}\text{W}$ reaction is in agreement with the calculation by Delagrange *et al.* [2], which is also in agreement with our measurements.

Bibliography

- [1] M. Rajagopalan, D. Logan, J. W. Ball, M. Kaplan, H. Delagrange, M. F. Rivet, J. M. Alexander, L. C. Vaz, and M. S. Zisman, *Phys. Rev. C* **25**, 2417 (1982).
- [2] H. Delagrange, A. Benachou, F. Hubert, Y. Llabador, B. Heusch, J. Coffin, P. Engelstein, P. Fintz, and G. Guillaume, *Nucl. Phys. A* **429**, 173 (1984).
- [3] A. K. Sinha, N. Madhavan, J. J. Das, P. Sugathan, D. O. Kataria, A. P. Patro, and G. K. Mehta, *Nucl. Instrum. Methods Phys. Res. A* **339**, 543 (1994).
- [4] B. P. Ajith Kumar, E. T. Subramaniam, and R. K. Bhowmik, <http://www.iuac.res.in/NIAS>.
- [5] S. Nath, P. V. M. Rao, S. Pal, J. Gehlot, E. Prasad, G. Mohanto, S. Kalkal, J. Sadhukhan, P. D. Shidling, K. S. Golda, A. Jhingan, N. Madhavan, S. Muralithar, and A. K. Sinha, *Phys. Rev. C* **81**, 064601 (2010).
- [6] S. Nath, *Comput. Phys. Commun.* **180**, 2392 (2009).
- [7] O. B. Tarasov and D. Bazin, *Nucl. Instrum. Methods Phys. Res. B* **266**, 4657 (2008), proceedings of the XVth International Conference on Electromagnetic Isotope Separators and Techniques Related to their Applications.
- [8] A. Gavron, *Phys. Rev. C* **21**, 230 (1980).
- [9] <http://lise.nscl.msu.edu/pace4>.
- [10] <http://nrv.jinr.ru/nrv/webnrv/qcalc/>.
- [11] K. Hagino, N. Rowley, and A. T. Kruppa, *Comput. Phys. Commun.* **123**, 143 (1999).

- [12] K. Hagino and N. Takigawa, *Prog. Theor. Phys* **128**, 1061 (2012).
- [13] W. Reisdorf, *Z. Phys. A* **300**, 227 (1981).
- [14] W. Reisdorf and M. Schädel, *Z. Phys. A Hadrons Nucl.* **343**, 47 (1992).
- [15] D. Vermeulen, H.-G. Clerc, C.-C. Sahn, K.-H. Schmidt, J. G. Keller, G. Münzenberg, and W. Reisdorf, *Z. Phys. A* **318**, 157 (1984).
- [16] T. Sikkeland, J. E. Clarkson, N. H. Steiger-Shafir, and V. E. Viola, *Phys. Rev. C* **3**, 329 (1971).
- [17] J. U. Andersen, A. S. Jensen, E. Laegsgaard, K. O. Nielsen, J. S. Forster, I. V. Mitchell, D. Ward, and W. M. Gibson, *Proc. Conf. on physics and chemistry of fission, 1979 vol. I* (IAEA, Vienna 1980).
- [18] <http://www2.yukawa.kyoto-u.ac.jp/kouichi.hagino/ccfull.html>.
- [19] J. R. Leigh, J. J. M. Bokhorst, D. J. Hinde, and J. O. Newton, *J. Phys. G: Nucl. Part. Phys.* **14**, L55 (1988).
- [20] M. Zamrun, F. K. Hagino, and N. Takigawa, Sub-barrier Fusion Cross Sections with Energy Density Formalism, in L. Corradi, D. Ackermann, E. Fioretto, A. Gadea, F. Haas, G. Pollarolo, F. Scarlassara, S. Szilner, and M. Trotta, eds., *Fusion06: Reaction Mechanisms and Nuclear Structure at the Coulomb Barrier* (2006), *American Institute of Physics Conference Series*, volume 853, pp. 309–314.
- [21] P. Jisha, A. M. Vinodkumar, B. R. S. Babu, S. Nath, N. Madhavan, J. Gehlot, A. Jhingan, T. Banerjee, I. Mukul, R. Dubey, N. Saneesh, K. M. Varier, E. Prasad, A. Shamlath, P. V. Laveen, and M. Shareef, *Phys. Rev. C* **101**, 024611 (2020).

- [22] S. Raman, C. W. Nestor, and P. Tikkanen, *At. Data Nucl. Data Tables* **78**, 1 (2001).
- [23] P. Möller, A. J. Sierk, T. Ichikawa, and H. Sagawa, *At. Data Nucl. Data Tables* **109-110**, 1 (2016).
- [24] Z. Kohley, J. F. Liang, D. Shapira, R. L. Varner, C. J. Gross, J. M. Allmond, A. L. Caraley, E. A. Coello, F. Favela, K. Lagergren, and P. E. Mueller, *Phys. Rev. Lett.* **107**, 202701 (2011).
- [25] Z. Kohley, J. F. Liang, D. Shapira, C. J. Gross, R. L. Varner, J. M. Allmond, J. J. Kolata, P. E. Mueller, and A. Roberts, *Phys. Rev. C* **87**, 064612 (2013).
- [26] S. Cohen, F. Plasil, and W. Swiatecki, *Annals of Physics* **82**, 557 (1974).
- [27] R. N. Sagaidak and A. N. Andreyev, *Phys. Rev. C* **79**, 054613 (2009).
- [28] T. Banerjee, S. Nath, and S. Pal, *Phys. Rev. C* **91**, 034619 (2015).
- [29] R. Bass, *Phys. Rev. Lett.* **39**, 265 (1977).
- [30] S. K. Hui, C. R. Bhuinya, A. K. Ganguly, N. Madhavan, J. J. Das, P. Sugathan, D. O. Kataria, S. Murlithar, L. T. Baby, V. Tripathi, A. Jhingan, A. K. Sinha, P. V. Madhusudhana Rao, N. V. S. V. Prasad, A. M. Vinodkumar, R. Singh, M. Thoennessen, and G. Gervais, *Phys. Rev. C* **62**, 054604 (2000).
- [31] M. Crippa, E. Gadioli, P. Vergani, G. Ciavola, C. Marchetta, and M. Bonardi, *Z. Phys. A Hadrons Nucl.* **350**, 121 (1994).
- [32] K. S. Babu, R. Tripathi, K. Sudarshan, B. D. Shrivastava, A. Goswami, and B. S. Tomar, *J. Phys. G: Nucl. Part. Phys.* **29**, 1011 (2003).

Chapter 5

Study of Quasifission processes in $^{180-198}\text{Hg}$ compound nuclei

5.1 Introduction

In this Chapter, we discuss about the systematic analysis carried out to study the dependence of entrance channel mass asymmetry and effective fissility parameters on quasifission processes. For this systematic analysis, we have carried out statistical model calculations for the reactions forming $^{180-198}\text{Hg}$ compound nuclei. The aim of this chapter is to summarize the effects of entrance channel mass asymmetry and effective fissility parameters on quasifission processes in $^{180-198}\text{Hg}$ CN.

Quasifission is one of the main obstacle for the superheavy elements (SHE) production and investigation of theoretically predicted island of stability [1–5]. Fusion reactions have been used in the majority of heavy element synthesis [6–8]. For the heavy ion fusion processes, the cross sections for producing a heavy ER can be written as

$$\sigma_{ER} = \Sigma \sigma_{capture}(E_{cm}, J) P_{CN}(E^*, J) W_{sur}(E^*, J) \quad (5.1)$$

where $\sigma_{capture}(E_{cm}, J)$ is the capture cross sections at the center of mass

energy $E_{c.m.}$ and spin J , P_{CN} is the fusion probability and W_{sur} is the survival probability of the CN against fission.

When projectile-target system overcomes the Coulomb barrier and it will reach the point of contact, which is described by the capture cross sections. The capture cross section can be calculated with a coupled-channel approach [9]. The masses of the touching nuclei and on their deformation at the point of contact have significant effect on the further evolution of the system. The fused system evolves from the touching configuration to CN in competition with non-compound nuclear fission (NCNF) processes, which is described by the fusion probability (P_{CN}). P_{CN} is the probability that the di-nuclear system crosses the inner fusion barrier and forms the CN. In the case of a mass asymmetric system, especially for fusion reactions dealing with light and medium nuclei, the compound nucleus formation probability is close to unity ($P_{CN} \approx 1$). The formed CN de-excited either by emission of light particles or by fission, which is described by the survival probability. The survival probability of the formed compound nucleus can be estimated using well established formalisms [10].

The fusion probability is the least known quantity and it is difficult to measure and to calculate. In this chapter, we discuss the dependence of the variation of P_{CN} with the entrance-channel mass asymmetry and the effective fissility parameters for $^{180-198}\text{Hg}$ CN. In the case of heavy system leading to a SHE, the production cross sections are dramatically reduced due to the presence of quasifission (QF) [11–16]. In heavy ion reactions, the fusion processes depends on many factors, such as the product $Z_P Z_T$ (where Z_P and Z_T are the proton numbers of projectile and target), deformations of projectile and target, and the mass asymmetry ($\alpha = (A_T - A_P)/(A_T + A_P)$, where A_T and A_P are the target and projectile masses respectively) of the projectile-target combinations.

According to the entrance-channel mass asymmetry criterion, QF is observed in systems where the entrance-channel mass asymmetry is smaller than the Businaro-Gallone mass asymmetry (α_{BG} , a point where potential is maximum for a given fissility [17]). The Swiatecki's [18] macroscopic-microscopic model

calculations show that the $Z_P Z_T$ threshold value for the appearance of QF is 1600. However, the onset of QF was observed even for a lower values $Z_P Z_T \approx 800$ [19].

Kozulin *at al.* [20] observed a large contribution (more than 70%) of quasifission (QF) in the case of $^{68}\text{Zn}+^{112}\text{Sn}$ reaction. However QF was not observed in the case of $^{36}\text{Ar}+^{144}\text{Sm}$ reaction forming the same CN, ^{180}Hg [21–23]. du Rietz *at al.* [24] analyzed large set of experimental mass-angular distributions of fission-like fragments and found that the threshold value for the QF appearance for composite systems with $Z_{CN} = 80$ is $Z_P Z_T = 1450 \pm 100$ (where Z_{CN} , Z_P and Z_T are the atomic number of the CN, projectile and target respectively). Also, they reported that QF appears for the reactions with mean fissility parameter $\chi_m > 0.68$ and QF becomes dominant at $\chi_m > 0.765$. In the case of $^{68}\text{Zn}+^{112}\text{Sn}$, the value of χ_m (0.695) and the $Z_P Z_T$ (1500) are close to the threshold values for the onset of the QF processes. Such a large contribution of QF was unexpected. Kaur *at al.* [25] measured ER cross sections for $^{48}\text{Ti}+^{140,142}\text{Ce}$ reactions forming $^{188,190}\text{Hg}$ CN, to understand the influence of neutron shell closure of target nuclei on CN formation. They observed that the effects of shell closure in the target nucleus on fusion cross sections is negligible. Further, they found no evidence of QF processes in the $^{48}\text{Ti}+^{140,142}\text{Ce}$ systems.

As mentioned, the mean fissility parameter for the $^{68}\text{Zn}+^{112}\text{Sn}$ reaction, $\chi_m = 0.695$, is just above the threshold value (0.68) for the presence of QF processes. When compared to the $^{36}\text{Ar}+^{144}\text{Sm}$ reaction, the changes in the entrance channel properties are not so drastic to cause such a large contribution of QF in the $^{68}\text{Zn}+^{112}\text{Sn}$ reaction. The main difference between these two reactions is the entrance-channel mass asymmetry parameter (α), which drops from 0.60 for $^{36}\text{Ar}+^{144}\text{Sm}$ to 0.24 for $^{68}\text{Zn}+^{112}\text{Sn}$ reaction. Kozulin *at al.* [20] suggested that the influence of the entrance-channel mass asymmetry on QF processes is much stronger than previously assumed. To explore the dependence of the fissility parameter and the entrance-channel mass asymmetry on the QF processes, we have studied even-even Hg CN from ^{180}Hg to ^{198}Hg . In

addition to that two odd-even nuclei namely ^{185}Hg and ^{195}Hg also are considered.

5.2 Systematic analysis for $^{180-198}\text{Hg}$ CN

We performed statistical model calculations for $^{40}\text{Ar}+^{144-154}\text{Sm}$ [26], $^{48}\text{Ti}+^{140,142}\text{Ce}$ [25], $^{19}\text{F}+^{175}\text{Lu}$ [27], $^{16}\text{O}+^{176,180}\text{Hf}$ [28], $^{90}\text{Zr}+^{90-96}\text{Zr}$ [29–31], $^{86}\text{Kr}+^{99-104}\text{Ru}$ [32], $^{124,130,134}\text{Te}+^{58,64}\text{Ni}$ [33], and $^{14}\text{N}+^{181}\text{Ta}$ [34] reactions, in addition to our ER measurements of $^{12}\text{C}+^{182,184,186}\text{W}$ reactions, forming $^{180-198}\text{Hg}$ CN. At energies higher than 100 MeV excitation energy, the competition between fission and evaporation is even more complex. Also, due to the paucity of experimental cross sections for other reactions forming Hg CN at these high energies, we limit our calculations to excitation energies below 100 MeV.

For the calculations, the standard set parameters, ie., Reisdorf and Schädel parameters [35] were used. Among this standard set of parameters, we varied the parameters of the nuclear potential to explain the measured ER cross sections. In addition, we considered the effects of static deformation of the target on fusion probabilities below the threshold. The static quadrupole moment for odd-even nuclei (^{181}Ta and ^{99}Ru) have been approximated by averaging the corresponding values in neighboring even-even nuclei. We have performed statistical model calculations by varying fission barrier scaling factor k_f for majority of the asymmetric systems and able to find suitable values which can simultaneously reproduce the experimental fission and ER cross sections. In HIVAP calculations, the $k_f = 0.88$ for ^{180}Hg to ^{190}Hg CN and 0.96 for $^{192-198}\text{Hg}$ CN were used. Also, the same k_f was used for neighboring reactions where no fission measurements are available. To explain the measured ER excitation functions of less asymmetric systems, we varied the CN formation probability (P_{CN}) from unity. The deviation of P_{CN} from unity indicates the presence of QF or other NCNF processes. The results of the HIVAP calculations, as well as the measured cross sections for ^{180}Hg to ^{188}Hg CN are shown in Figs. 5.1(a)-(f) and for ^{190}Hg to ^{198}Hg CN are

shown in Figs. 5.2(a)-(f), where solid points represent experimental cross sections and lines represent HIVAP calculations. From Figs. 5.1(a)-(c), it is clear that the calculated ER cross sections for the reactions forming $^{180,182,184}\text{Hg}$ nuclei show slight deviation at below barrier energies in comparison with the measurements. This may be due to the approximations included in the coupling effects of the HIVAP calculations at these lower excitation energies. The entrance channel properties, $Z_P Z_T$, entrance-channel mass asymmetry (α), the mean fissility parameter (χ_m), effective fissility parameter (χ_{eff}) and CN formation probability (P_{CN}) for the reactions leading to the formation of $^{180-198}\text{Hg}$ CN are listed in Table 5.1.

Table 5.1: The entrance channel properties and P_{CN} for the reactions leading to the formation of $^{180-198}\text{Hg}$.

Reaction	CN	$Z_P Z_T$	α	χ_m	χ_{eff}	P_{CN}	Ref
$^{90}\text{Zr}+^{90}\text{Zr}$	^{180}Hg	1600	0.0	0.714	0.714	0.35	[29–31]
$^{90}\text{Zr}+^{92}\text{Zr}$	^{182}Hg	1600	0.011	0.710	0.710	0.48	[31]
$^{90}\text{Zr}+^{94}\text{Zr}$	^{184}Hg	1600	0.022	0.705	0.705	0.50	[29]
$^{40}\text{Ar}+^{144}\text{Sm}$	^{184}Hg	1116	0.565	0.613	0.583	1	[26]
$^{86}\text{Kr}+^{99}\text{Ru}$	^{185}Hg	1584	0.070	0.699	0.697	0.50	[32]
$^{90}\text{Zr}+^{96}\text{Zr}$	^{186}Hg	1600	0.032	0.701	0.701	0.48	[31]
$^{124}\text{Te}+^{64}\text{Ni}$	^{188}Hg	1456	0.319	0.673	0.665	0.60	[33]
$^{130}\text{Te}+^{58}\text{Ni}$	^{188}Hg	1456	0.383	0.684	0.680	0.70	[33]
$^{86}\text{Kr}+^{102}\text{Ru}$	^{188}Hg	1584	0.085	0.693	0.692	0.60	[32]
$^{40}\text{Ar}+^{148}\text{Sm}$	^{188}Hg	1116	0.574	0.609	0.580	1	[26]
$^{48}\text{Ti}+^{140}\text{Ce}$	^{188}Hg	1276	0.489	0.644	0.627	1	[25]
$^{48}\text{Ti}+^{142}\text{Ce}$	^{190}Hg	1276	0.495	0.642	0.626	1	[25]
$^{86}\text{Kr}+^{104}\text{Ru}$	^{190}Hg	1584	0.095	0.690	0.689	0.65	[32]
$^{16}\text{O}+^{176}\text{Hf}$	^{192}Hg	576	0.833	0.484	0.415	1	[28]
$^{12}\text{C}+^{182}\text{W}$	^{194}Hg	444	0.876	0.440	0.358	1	This work
$^{19}\text{F}+^{175}\text{Lu}$	^{194}Hg	639	0.804	0.495	0.431	1	[27]
$^{40}\text{Ar}+^{154}\text{Sm}$	^{194}Hg	1116	0.588	0.604	0.577	1	[26]
$^{14}\text{N}+^{181}\text{Ta}$	^{195}Hg	511	0.856	0.462	0.388	1	[34]
$^{12}\text{C}+^{184}\text{W}$	^{196}Hg	444	0.878	0.439	0.358	1	This work
$^{16}\text{O}+^{180}\text{Hf}$	^{196}Hg	576	0.837	0.482	0.415	1	[28]
$^{12}\text{C}+^{186}\text{W}$	^{198}Hg	444	0.879	0.438	0.357	1	This work
$^{134}\text{Te}+^{64}\text{Ni}$	^{198}Hg	1456	0.354	0.662	0.656	1	[33]

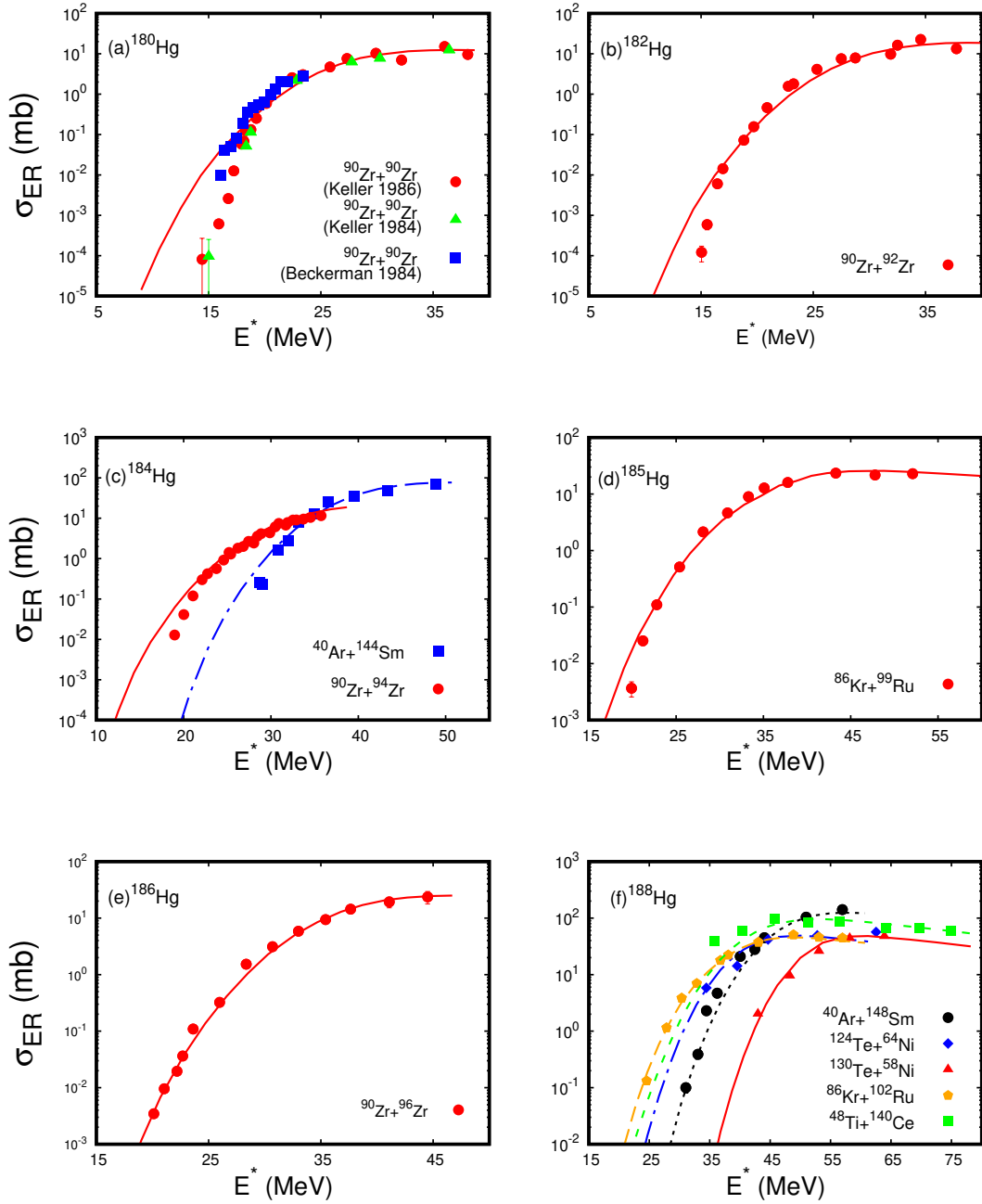


Figure 5.1: Measured ER cross sections along with statistical model calculations as a function of E^* for the reactions forming ^{180}Hg to ^{188}Hg CN. Solid symbols are the experimental data and lines are the statistical model calculations.

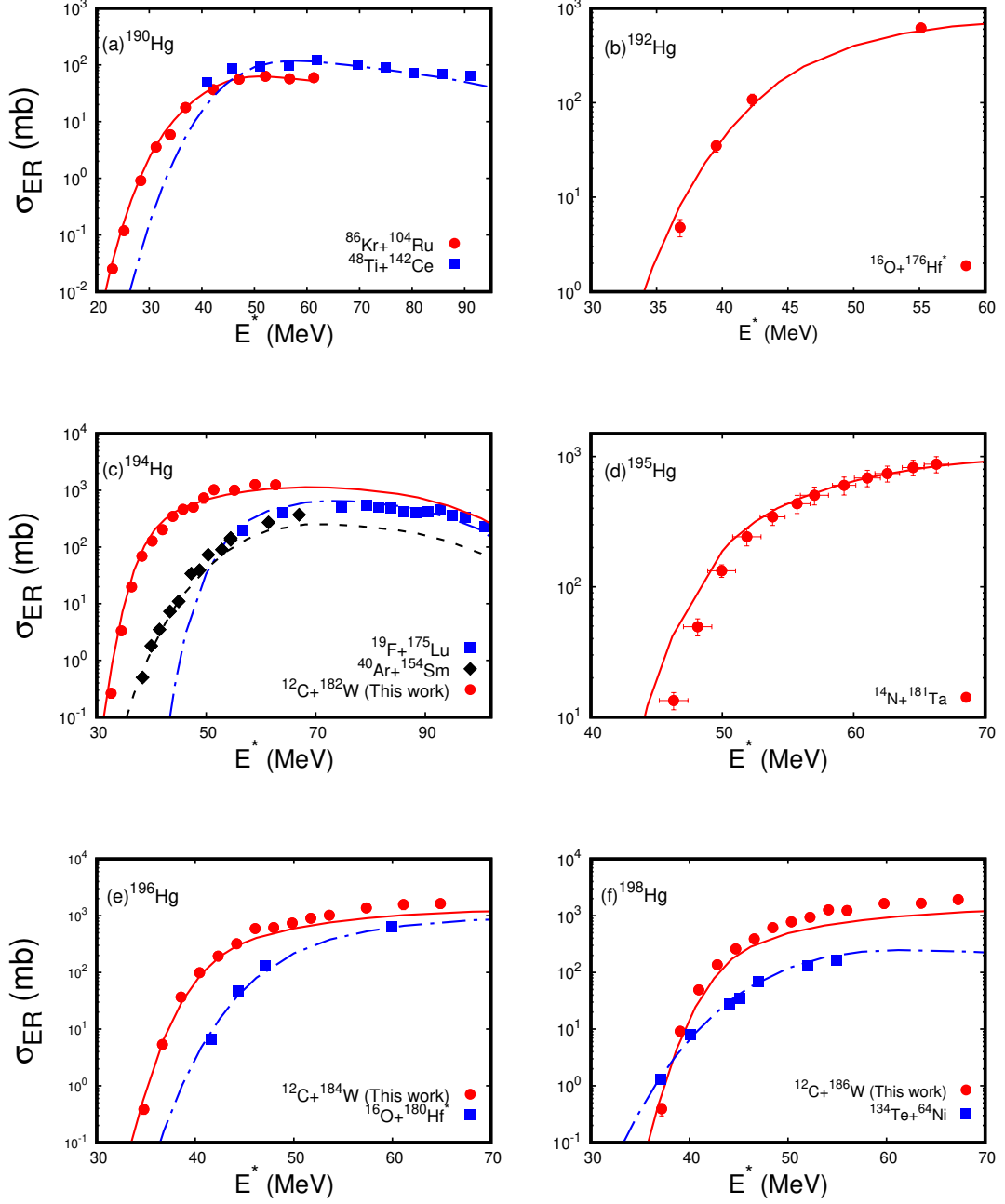


Figure 5.2: Measured ER cross sections along with statistical model calculations as a function of E^* for the reactions forming ^{190}Hg to ^{198}Hg CN. Solid symbols are the experimental data and lines are the HIVAP calculations. In panels b and e, in the case of $^{16}\text{O} + ^{176,180}\text{Hf}$ reactions, instead of σ_{ER} we have taken the measured σ_{fus} from literature [28].

5.3 Dependence of QF on entrance channel parameters

As mentioned, QF is the main mechanism hindering the formation of heavy and superheavy elements using fusion processes. The dependence of the QF and CN formation mechanisms on the entrance channel properties is one of the experimental tasks to predict the trends in cross sections. There have been a number of systematics on P_{CN} using various approaches for both hot and cold fusion reactions [36–45].

To explore the variation of P_{CN} with the entrance-channel mass asymmetry α , and the effective fissility parameter χ_{eff} , we have plotted P_{CN} as a function of α and χ_{eff} , as shown in Fig. 5.3 and Fig. 5.4 respectively. In these figures, the red points represent the $^{12}\text{C}+^{182,184,186}\text{W}$ reactions.

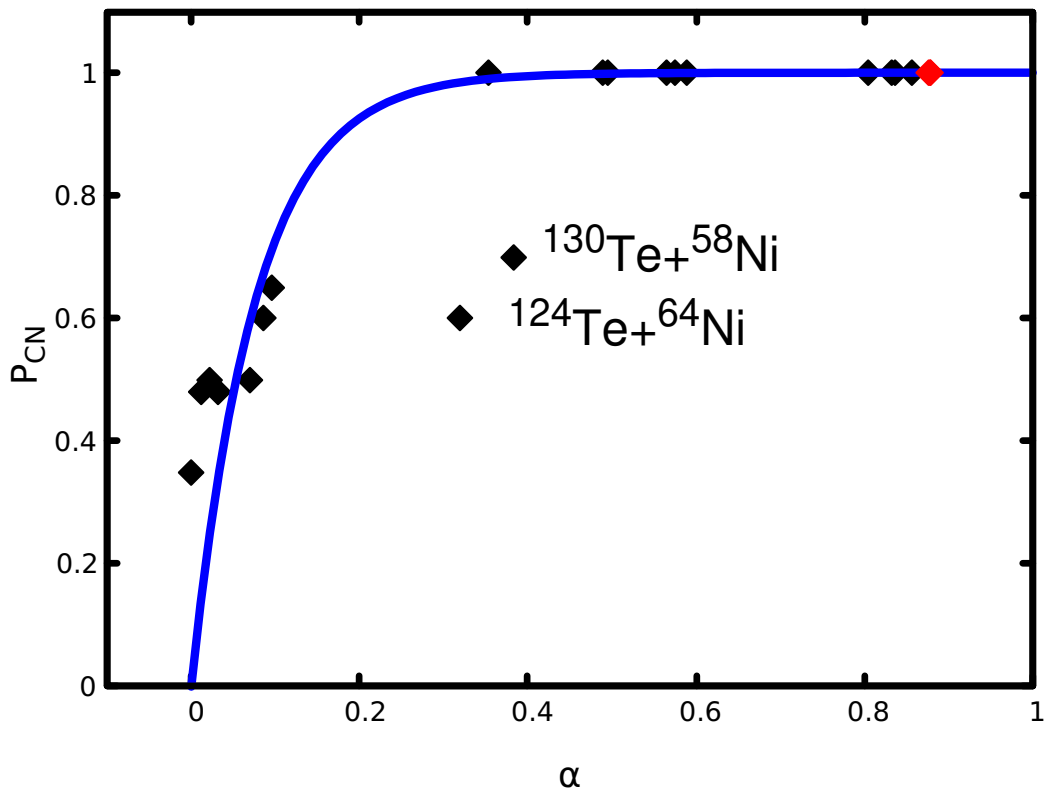


Figure 5.3: The variation of P_{CN} with the entrance-channel mass asymmetry (α).

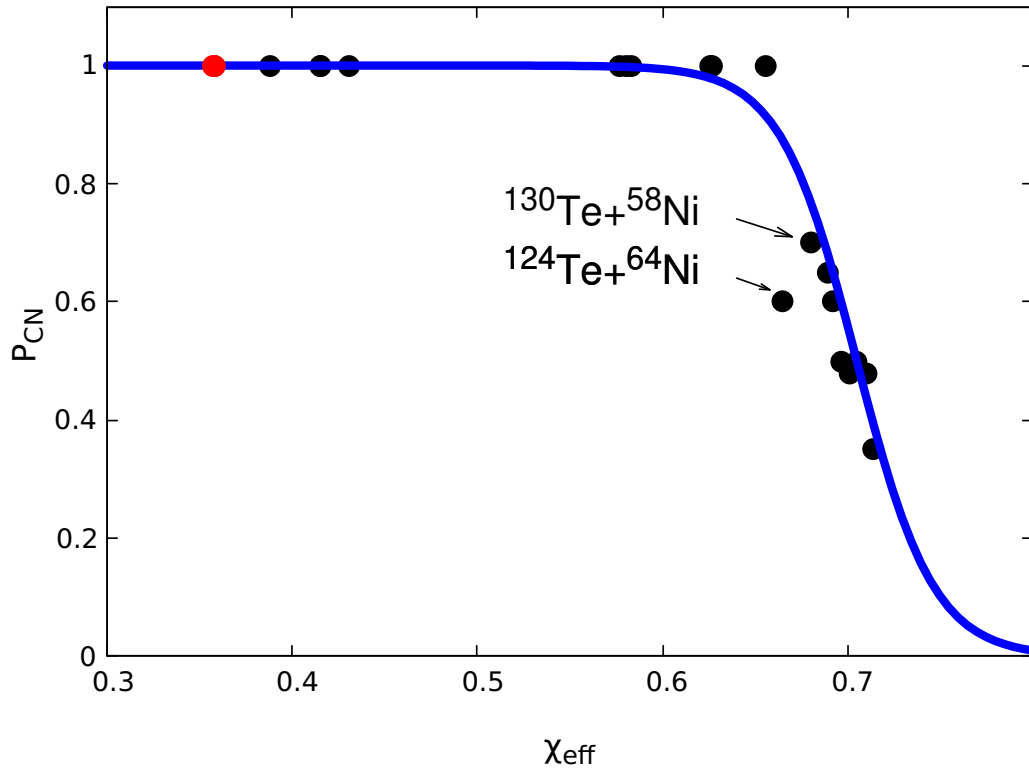


Figure 5.4: The variation of P_{CN} with the effective fissility parameter (χ_{eff}).

In Fig. 5.3, $^{124,130}\text{Te}+^{64,58}\text{Ni}$ [33] reactions forming ^{188}Hg CN show a significant deviation of P_{CN} as a function of α compared to the other data set. However, $^{124,130}\text{Te}+^{64,58}\text{Ni}$ [33] reactions, which show large deviation in Fig. 5.3, do not show such large deviation of P_{CN} as a function of χ_{eff} in Fig. 5.4. Based on Fig. 5.3 and Fig. 5.4, we can conclude that reactions having $\chi_{eff} \geq 0.64$, show presence of QF. If one considers entrance channel mass asymmetry, $\alpha \leq 0.2$ will show QF. Our systematic analysis for $^{180-198}\text{Hg}$ CN clearly shows the dependence of QF on α and the χ_{eff} . However, additional experiments with reactions leading to the formation of the Hg CN are needed to confirm these findings. Especially, the measurements of the reactions with mass asymmetry 0.1-0.3 and effective fissility parameter 0.63-0.70 are needed for better understanding.

Bibliography

- [1] U. Mosel and W. Greiner, *Z. Phys. A Hadrons and nucl.* **222**, 261 (1969).
- [2] S. G. Nilsson, C. F. Tsang, A. Sobiczewski, Z. Szymanski, S. Wycech, C. Gustafson, I.-L. Lamm, P. Mller, and B. Nilsson, *Nucl. Phys. A* **131**, 1 (1969).
- [3] M. Bender, W. Nazarewicz, and P.-G. Reinhard, *Phys. Lett. B* **515**, 42 (2001).
- [4] P. Ring, *Prog. Part. Nucl. Phys.* **37**, 193 (1996).
- [5] S. wiok, J. Dobaczewski, P.-H. Heenen, P. Magierski, and W. Nazarewicz, *Nucl. Phys. A* **611**, 211 (1996).
- [6] Y. T. Oganessian, V. K. Utyonkov, Y. V. Lobanov, F. S. Abdullin, A. N. Polyakov, I. V. Shirokovsky, Y. S. Tsyganov, G. G. Gulbekian, S. L. Bogomolov, B. N. Gikal, A. N. Mezentsev, S. Iliev, V. G. Subbotin, A. M. Sukhov, A. A. Voinov, G. V. Buklanov, K. Subotic, V. I. Zagrebaev, M. G. Itkis, J. B. Patin, K. J. Moody, J. F. Wild, M. A. Stoyer, N. J. Stoyer, D. A. Shaughnessy, J. M. Kenneally, P. A. Wilk, R. W. Loughheed, R. I. Il'kaev, and S. P. Vesnovskii, *Phys. Rev. C* **70**, 064609 (2004).
- [7] Y. T. Oganessian, V. K. Utyonkov, Y. V. Lobanov, F. S. Abdullin, A. N. Polyakov, R. N. Sagaidak, I. V. Shirokovsky, Y. S. Tsyganov, A. A. Voinov, G. G. Gulbekian, S. L. Bogomolov, B. N. Gikal, A. N. Mezentsev, S. Iliev, V. G. Subbotin, A. M. Sukhov, K. Subotic, V. I. Zagrebaev, G. K. Vostokin, M. G. Itkis, K. J. Moody, J. B. Patin, D. A. Shaughnessy, M. A. Stoyer, N. J. Stoyer, P. A. Wilk, J. M. Kenneally, J. H. Landrum, J. F. Wild, and R. W. Loughheed, *Phys. Rev. C* **74**, 044602 (2006).

- [8] Y. T. Oganessian, F. S. Abdullin, P. D. Bailey, D. E. Benker, M. E. Bennett, S. N. Dmitriev, J. G. Ezold, J. H. Hamilton, R. A. Henderson, M. G. Itkis, Y. V. Lobanov, A. N. Mezentsev, K. J. Moody, S. L. Nelson, A. N. Polyakov, C. E. Porter, A. V. Ramayya, F. D. Riley, J. B. Roberto, M. A. Ryabini, K. P. Rykaczewski, R. N. Sagaidak, D. A. Shaughnessy, I. V. Shirokovsky, M. A. Stoyer, V. G. Subbotin, R. Sudowe, A. M. Sukhov, Y. S. Tsyganov, V. K. Utyonkov, A. A. Voinov, G. K. Vostokin, and P. A. Wilk, *Phys. Rev. Lett.* **104**, 142502 (2010).
- [9] K. Hagino, N. Rowley, and A. T. Kruppa, *Comput. Phys. Commun.* **123**, 143 (1999).
- [10] <http://nrv.jinr.ru/nrv>.
- [11] E. Prasad, D. J. Hinde, E. Williams, M. Dasgupta, I. P. Carter, K. J. Cook, D. Y. Jeung, D. H. Luong, C. S. Palshetkar, D. C. Rafferty, K. Ramachandran, C. Simenel, and A. Wakhle, *Phys. Rev. C* **96**, 034608 (2017).
- [12] M. G. Itkis, E. Vardaci, I. M. Itkis, G. N. Knyazheva, and E. M. Kozulin, *Nucl. Phys. A* **944**, 204 (2015), special Issue on Superheavy Elements.
- [13] W. J. Swiatecki, *Physica Scripta* **24**, 113 (1981).
- [14] S. Bjørnholm and W. J. Swiatecki, *Nucl. Phys. A* **391**, 471 (1982).
- [15] J. P. Blocki, H. Feldmeier, and W. J. Swiatecki, *Nucl. Phys. A* **459**, 145 (1986).
- [16] P. Möller and A. J. Sierk, *Nature* **422**, 485 (2003).
- [17] U. L. Businaro and S. Gallone, *Il Nuovo Cimento (1955-1965)* **5**, 315 (1957).
- [18] W. J. Swiatecki, *Nucl. Phys. A* **376**, 275 (1982).

- [19] A. C. Berriman, D. J. Hinde, D. M., M. C. R., B. R. D., and J. O. Newton, *Nature* **413**, 144 (2001).
- [20] E. M. Kozulin, E. Vardaci, W. H. Trzaska, A. A. Bogachev, I. M. Itkis, A. V. Karpov, G. N. Knyazheva, and K. V. Novikov, *Phys. Lett. B* **819**, 136442 (2021).
- [21] E. Prasad, D. J. Hinde, M. Dasgupta, D. Y. Jeung, A. C. Berriman, B. M. A. Swinton-Bland, C. Simenel, E. C. Simpson, R. Bernard, E. Williams, K. J. Cook, D. C. Rafferty, C. Sengupta, J. F. Smith, K. Vo-Phuoc, and J. Walshe, *Phys. Lett. B* **811**, 135941 (2020).
- [22] K. Nishio, A. N. Andreyev, R. Chapman, X. Derkx, C. E. Dllmann, L. Ghys, F. P. Heberger, K. Hirose, H. Ikezoe, J. Khuyagbaatar, B. Kindler, B. Lommel, H. Makii, I. Nishinaka, T. Ohtsuki, S. D. Pain, R. Sagaidak, I. Tsekhanovich, M. Venhart, Y. Wakabayashi, and S. Yan, *Phys. Lett. B* **748**, 89 (2015).
- [23] D. Kumar, E. M. Kozulin, M. Cheralu, G. N. Knyazheva, I. M. Itkis, M. G. Itkis, K. V. Novikov, A. A. Bogachev, N. I. Kozulina, I. N. Diatlov, I. V. Pchelintsev, I. V. Vorobiev, T. Banerjee, Y. S. Mukhamejanov, A. N. Pan, V. V. Saiko, P. P. Singh, R. N. Sahoo, A. N. Andreyev, D. M. Filipescu, M. Maiti, R. Prajapat, and R. Kumar, *Bull. Russ. Acad. Sci.: Phys* **84**, 1001 (2020).
- [24] R. du Rietz, E. Williams, D. J. Hinde, M. Dasgupta, M. Evers, C. J. Lin, D. H. Luong, C. Simenel, and A. Wakhle, *Phys. Rev. C* **88**, 054618 (2013).
- [25] D. P. Kaur, B. R. Behera, N. Madhavan, S. Nath, J. Gehlot, A. Kaur, Raghav, Gonika, R. Biswas, Subodh, Amit, A. Parihari, K. Rani, H. Arora, Shruti, and S. Pal, *Nucl. Phys. A* **1019**, 122384 (2022).

- [26] R. G. Stokstad, W. Reisdorf, K. D. Hildenbrand, J. V. Kratz, G. Wirth, R. Lucas, and J. Poitou, *Z. Phys. A* **295**, 269 (1980).
- [27] S. K. Hui, C. R. Bhuinya, A. K. Ganguly, N. Madhavan, J. J. Das, P. Sugathan, D. O. Kataria, S. Murlithar, L. T. Baby, V. Tripathi, A. Jhingan, A. K. Sinha, P. V. Madhusudhana Rao, N. V. S. V. Prasad, A. M. Vinodkumar, R. Singh, M. Thoennessen, and G. Gervais, *Phys. Rev. C* **62**, 054604 (2000).
- [28] J. R. Leigh, J. J. M. Bokhorst, D. J. Hinde, and J. O. Newton, *J. Phys. G: Nucl. Part. Phys.* **14**, L55 (1988).
- [29] M. Beckerman, J. Wiggins, H. Aljuwair, and M. K. Salomaa, *Phys. Rev. C* **29**, 1938 (1984).
- [30] J. G. Keller, K.-H. Schmidt, H. Stelzer, W. Reisdorf, Y. K. Agarwal, F. P. Hessberger, G. Münzenberg, H.-G. Clerc, and C.-C. Sahm, *Phys. Rev. C* **29**, 1569 (1984).
- [31] J. G. Keller, K. H. Schmidt, F. P. Hessberger, G. Münzenberg, W. Reisdorf, H. G. Clerc, and C. C. Sahm, *Nucl. Phys. A* **452**, 173 (1986).
- [32] W. Reisdorf, F. P. Hessberger, K. D. Hildenbrand, S. Hofmann, G. Münzenberg, K.-H. Schmidt, W. F. W. Schneider, K. Smmerer, G. Wirth, J. V. Kratz, K. Schutt, and C.-C. Sahm, *Nucl. Phys. A* **444**, 154 (1985).
- [33] D. Shapira, F. Liang, C. Gross, R. Varner, J. Beene, A. Galindo-Uribarri, J. Campo, P. Hausladen, P. Mueller, D. Stracener, J. Kolata, and H. Amro, *AIP Conf. Proc.* **853** (2006).
- [34] M. S. Asnain, M. Shuaib, I. Majeed, M. K. Sharma, V. R. Sharma, A. Yadav, D. P. Singh, P. P. Singh, U. Gupta, R. N. Sahoo, A. Sood, M. Kaushik,

- S. Kumar, R. Kumar, B. P. Singh, and R. Prasad, *Phys. Rev. C* **104**, 034616 (2021).
- [35] W. Reisdorf and M. Schädel, *Z. Phys. A Hadrons Nucl.* **343**, 47 (1992).
- [36] R. Yanez, W. Loveland, J. S. Barrett, L. Yao, B. B. Back, S. Zhu, and T. L. Khoo, *Phys. Rev. C* **88**, 014606 (2013).
- [37] C. C. Sahm, H. G. Clerc, K.-H. Schmidt, W. Reisdorf, P. Armbruster, F. P. Hessberger, J. G. Keller, G. Mnzenberg, and D. Vermeulen, *Nucl. Phys. A* **441**, 316 (1985).
- [38] V. I. Zagrebaev, *Phys. Rev. C* **67**, 061601 (2003).
- [39] J. Blocki, L. Shvedov, and J. Wilczyński, *Int. J. Mod. Phys. E* **15**, 426 (2006).
- [40] K. Siwek-Wilczyńska, A. Borowiec, I. Skwira-Chalot, and J. Wilczyński, *Int. J. Mod. Phys. E* **17**, 12 (2008).
- [41] N. Wang, J. Tian, and W. Scheid, *Phys. Rev. C* **84**, 061601 (2011).
- [42] T. Banerjee, S. Nath, and S. Pal, *Phys. Rev. C* **91**, 034619 (2015).
- [43] W. Loveland, *J. Phys. Conf. Ser.* **420**, 012004 (2013), 1207.2095.
- [44] V. Zagrebaev and W. Greiner, *Phys. Rev. C* **78**, 034610 (2008).
- [45] Y. Aritomo, T. Wada, M. Ohta, and Y. Abe, *Phys. Rev. C* **59**, 796 (1999).

Chapter 6

Summary and Outlook

The study of reaction dynamics and decay properties of excited compound nuclei in heavy ion fusion reactions at energies close to the Coulomb barrier has drawn a lot of attention in recent years. Entrance channel parameters and structural properties of the projectile and/or target have a significant impact on fusion processes at near-barrier energies. The one-dimensional potential barrier penetration model (1D-BPM) is quite successful to explain the measured fusion cross sections at above barrier energies. At energies below the barrier, where quantum effects are prominent, the dynamics become more complex and it can be well explained by coupled-channel calculations, which include the coupling of low-lying states and the static deformation and/or vibrational degrees of freedom of participating nuclei. The statistical model framework has been used to explain the de-excitation of the composite system with the inclusion of fission processes. Though the fundamental concepts of composite system de-excitation are relatively well understood by statistical model calculations, some discrepancies and/or ambiguities remain [1–3].

Calculated fusion cross sections based on various theoretical models and systematics showed a large deviation with respect to measured cross sections for $^{12}\text{C}+^{182,186}\text{W}$ reactions in the laboratory energy range 77 to 167 MeV [4, 5]. However, fusion cross section measurements with heavier projectiles forming ^{194}Hg compound nucleus follow the fusion systematics. Also, lack of evapora-

tion residue cross section measurements in the below and near the Coulomb barrier region for $^{12}\text{C}+^{182,184,186}\text{W}$ reactions, forming $^{194,196,198}\text{Hg}$ compound nuclei, demands evaporation residue measurements.

Using a recoil mass spectrometer, we measured the evaporation residue excitation functions for $^{12}\text{C}+^{182,184,186}\text{W}$ reactions leading to the formation of $^{194,196,198}\text{Hg}$ compound nuclei at energies 12% below to 45% above the Coulomb barrier. The experiments were conducted at the Inter-University Accelerator Centre (IUAC) in New Delhi, using pulsed ^{12}C beams with energies ranging from 52 to 84 MeV provided by the 15UD Pelletron Accelerator. These pulsed ^{12}C beams with pulse separation 8 μs at 52-58 MeV, 4 μs at 60-72 MeV and 500 ns at 76-84 MeV were bombarded on $^{182,184,186}\text{W}$ targets with thicknesses 70, 100 and 100 $\mu\text{g}/\text{cm}^2$ with carbon backing of 20, 35 and 25 $\mu\text{g}/\text{cm}^2$ respectively. The enrichment for the $^{182,184,186}\text{W}$ targets were 91.6, 95.2 and 94.0 % respectively.

Two silicon surface barrier detectors (monitors) were placed in the target chamber, one on each side of the beam direction, to measure the elastically scattered beam particles for beam monitoring and absolute cross sections determination. A carbon charge reset foil with a large surface area and a thickness of ~ 10 $\mu\text{g}/\text{cm}^2$ was placed 10 cm downstream of the target to reset the charge state of evaporation residues. The Heavy Ion Reaction Analyzer (HIRA) [6] separated evaporation residues from the beam like background and transported them to its focal plane. For these experiments, the solid angle of acceptance for HIRA was kept at 5 msr . A two-dimensional position-sensitive multi-wire proportional counter with an active area of 15 $\text{cm} \times 5 \text{cm}$ was used at the HIRA's focal plane to detect ERs [7]. To separate the evaporation residues from the beam-like particles, a time of flight was set up between the anode of the multi-wire proportional counter and the radio frequency signal of the beam pulsing system.

In order to investigate the effects of coupling of different excited states of the target nuclei in the sub-barrier energy region we have analyzed measured cross sections for the $^{12}\text{C}+^{182,184,186}\text{W}$ reactions using coupled-channel calculations. In the CC calculations the Woods-Saxon parametrization of the nuclear potential

is used. In the current calculations, the depth parameter of the Woods-Saxon potential V_0 , the radius parameter r_0 , and the diffuseness parameter a_0 are 72.0 MeV, 1.15 fm and 0.70 fm respectively. Coupled-channel calculations with the coupling of static deformation effects of target nuclei, and using these potential parameters, explains the measured fusion cross sections for $^{12}\text{C}+^{182,184,186}\text{W}$ reactions in the sub-barrier energy region. However, deviations from measured cross sections have been noticed at higher excitation energies for $^{12}\text{C}+^{184,186}\text{W}$ reactions. Comparing $^{12}\text{C}+^{182}\text{W}$, $^{12}\text{C}+^{184}\text{W}$ and $^{12}\text{C}+^{186}\text{W}$ reactions, we could not observe any noticeable effects on the sub-barrier enhancement due to the addition of four neutrons in the compound nuclei, $^{194,196,198}\text{Hg}$.

To study the detailed de-excitation processes of $^{194,196,198}\text{Hg}$ compound nuclei, we have carried out statistical model calculations for $^{12}\text{C}+^{182,184,186}\text{W}$ reactions. The potential parameters used for the statistical model calculations, for $^{12}\text{C}+^{182,184,186}\text{W}$ reactions, are $V_0 = 72$ MeV, $r_0 = 1.12$ fm and $D = 0.62$ fm. Simultaneous analysis of fission and evaporation residue cross sections for $^{12}\text{C}+^{182,184,186}\text{W}$ reactions allow us to obtain the value of fission barrier. The fission cross sections for the systems $^{12}\text{C}+^{182,184,186}\text{W}$ were taken from literature [4, 5, 8, 9]. The statistical model calculations with probability of compound nucleus formation, $P_{CN} = 1$ and the fission barrier scaling parameter, $k_f = 0.96$ describes our measured evaporation residue as well as measured fission cross sections (from literature). From these results, we can conclude that the previously reported disagreement between measured and the calculated fusion cross sections for $^{12}\text{C}+^{182,186}\text{W}$ reactions [4, 5] could be due to the missing evaporation residue events in their detection systems. We find no role of dissipative effects in the competition between fission and evaporation of $^{12}\text{C}+^{182,184,186}\text{W}$ reactions in the measured energy region.

To explore the variation of compound nucleus formation probability, P_{CN} , with the entrance-channel mass asymmetry and the effective fissility parameter, we have carried out a systematic analysis for the reactions forming $^{180-198}\text{Hg}$ compound nuclei. Our systematic analysis for $^{180-198}\text{Hg}$ compound nuclei shows the

dependence of quasifission processes on entrance channel mass asymmetry and effective fissility parameter. The probability of forming a compound nucleus P_{CN} , correlates with the effective fissility parameter, χ_{eff} and entrance channel mass asymmetry α . Based on this systematic analysis, we can conclude that reactions forming $^{180-198}\text{Hg}$ compound nuclei, having effective fissility parameter (χ_{eff}) ≥ 0.64 , show the presence of quasifission. If one considers entrance channel mass asymmetry, $\alpha \leq 0.2$ will show quasifission.

6.1 Future plan

Calculated mass distributions for fission of different Hg isotopes by Andreev *et al.* [10] show large variation as one goes from neutron deficient ^{180}Hg to relatively neutron-rich ^{198}Hg nuclei. Their calculations using the improved scission-point model show the quite asymmetric mass distribution for ^{180}Hg and ^{184}Hg . For ^{188}Hg , the asymmetry is less pronounced. In the case of $^{192,196}\text{Hg}$ and ^{198}Hg the mass distribution looks more symmetric but with a dip on the top. Therefore it would be interesting to explore the transition from asymmetric to symmetric fission in fusion measurements, especially mass asymmetric fission following heavy ion fusion reactions.

Developed systematic analysis for $^{180-198}\text{Hg}$ compound nuclei, shows the dependence of quasifission processes on entrance channel mass asymmetry and effective fissility parameter. Additional experiments with reactions leading to the formation of the Hg compound nuclei with entrance mass asymmetry 0.1-0.3 and effective fissility parameter 0.63-0.70 are needed to further exploring the finding from our systematic analysis.

Bibliography

- [1] B. B. Back, D. J. Blumenthal, C. N. Davids, D. J. Henderson, R. Hermann, D. J. Hofman, C. L. Jiang, H. T. Penttilä, and A. H. Wuosmaa, *Phys. Rev. C* **60**, 044602 (1999).
- [2] R. G. Stokstad, W. Reisdorf, K. D. Hildenbrand, J. V. Kratz, G. Wirth, R. Lucas, and J. Poitou, *Z. Phys. A* **295**, 269 (1980).
- [3] A. Shrivastava, S. Kailas, A. Chatterjee, A. M. Samant, A. Navin, P. Singh, and B. S. Tomar, *Phys. Rev. Lett.* **82**, 699 (1999).
- [4] M. Rajagopalan, D. Logan, J. W. Ball, M. Kaplan, H. Delagrange, M. F. Rivet, J. M. Alexander, L. C. Vaz, and M. S. Zisman, *Phys. Rev. C* **25**, 2417 (1982).
- [5] H. Delagrange, A. Benachou, F. Hubert, Y. Llabador, B. Heusch, J. Coffin, P. Engelstein, P. Fintz, and G. Guillaume, *Nucl. Phys. A* **429**, 173 (1984).
- [6] A. K. Sinha, N. Madhavan, J. J. Das, P. Sugathan, D. O. Kataria, A. P. Patro, and G. K. Mehta, *Nucl. Instrum. Methods Phys. Res. A* **339**, 543 (1994).
- [7] J. Gehlot, A. Jhingan, T. Varughese, S. Nath, and N. Madhavan, *DAE Symp. Nucl. Phys.* **65**, 782 (2021).
- [8] T. Sikkeland, J. E. Clarkson, N. H. Steiger-Shafir, and V. E. Viola, *Phys. Rev. C* **3**, 329 (1971).
- [9] J. U. Andersen, A. S. Jensen, E. Laegsgaard, K. O. Nielsen, J. S. Forster, I. V. Mitchell, D. Ward, and W. M. Gibson, *Proc. Conf. on physics and chemistry of fission, 1979 vol. I* (IAEA, Vienna 1980).

- [10] A. V. Andreev, G. G. Adamian, and N. V. Antonenko, Phys. Rev. C **86**, 044315 (2012).

Recommendations

Production of superheavy elements using different projectile-target combinations and investigation of predicted island of stability are leading topics in contemporary nuclear physics. Quasifission process is the one of the important mechanism that prevents the formation of superheavy element in the heavy ion fusion reactions. Also, due to the low production rate of superheavy elements, it is very important to understand the initial conditions that favor the production of superheavy elements. Study of heavy ion fusion is important for understanding the nuclear reaction mechanism and get a clear picture of the most important entrance channel parameters that influence the quasifission process.

To study the reaction dynamics of ^{12}C induced reactions forming $^{194,196,198}\text{Hg}$ compound nuclei, we have measured the evaporation residue cross sections for $^{12}\text{C}+^{182,184,186}\text{W}$ reactions. The measured fusion cross sections are compared with coupled-channel and statistical model calculations. Coupled-channel and statistical model calculations explain the measured cross sections for these reactions. Also, to explore the dependence of quasifission process on entrance channel parameters we have carried out a systematic analysis for the reactions forming $^{180-198}\text{Hg}$ compound nuclei. These results will allow one to predict the compound nucleus formation probability for many compound nuclei of Hg. This can be extended to superheavy element synthesis.